Spectrum and Alignment-Aware Coverage in 6G Millimeter-Wave Networks: Technical and Regulatory Analysis

Wijdan Karam Salim Alsaedi

Doctor of Philosophy

University of York

Physics, Engineering and Technology

November 2025

Abstract

The emerging sixth generation (6G) of cellular networks are expected to use a wide range of spectrum, including millimeter wave (mmWave), terahertz (THz), and optical spectrum, to support ultra-data rates and low-latency applications such as extended reality (XR) services and connected autonomous systems. However, the directional nature of these bands introduces challenges such as severe path loss, sensitivity to blockages, complex hardware requirements, and strict beam alignment. In addition, the regulatory and standardization landscape for these bands remains incomplete. This thesis investigates these spectrum bands and beam alignment challenges through two complementary research directions.

First, a comprehensive survey of 6G spectrum options is conducted, analyzing spectrum allocation approaches and the status of standardization efforts for mmWave, THz, and optical wireless communication (OWC) technologies. Second, the thesis develops an information-aware beam alignment error model in mmWave. The proposed model introduces a novel alignment information parameter to quantify the available directional knowledge and jointly determine the variance and truncation boundaries, enabling a continuous transition from uniform error (no information) to truncated Gaussian (partial information) and to a Dirac delta function (near-perfect information). An antenna inefficiency factor accounts for hardware imperfections. Using stochastic geometry, downlink coverage probability is derived for both omni-antenna and directional antenna users, and a discrete-gain approximation is proposed to enable tractable analysis under cosine antenna patterns.

In summary, this thesis contributes to the understanding of high-frequency 6G networks by examining the opportunities, challenges, spectrum management considerations, and standardization status of mmWave, THz, and OWC technologies, while also demonstrating how alignment information influences beamwidth selection and coverage performance in mmWave systems.

Acknowledgements

I am deeply grateful to God for His endless blessings, guidance, and protection throughout my PhD journey. His grace has strengthened me through every challenge and illuminated my path during moments of uncertainty. I believe that all achievements are by His will, and I am thankful that He placed wonderful people in my life to support and guide me along the way.

I would like to express my sincere appreciation to my supervisors, Dr. Hamed Ahmadi and Dr. David Grace, for their exceptional mentorship, support, and invaluable insights. Their expertise, patience, and constructive feedback have been vital in shaping both this thesis and my development as a researcher. Their encouragement and dedication have guided me at every step.

My deepest gratitude goes to my family. To my parents, thank you for your unconditional love, sacrifices, and prayers, which have been my constant source of strength.

A special and heartfelt thanks goes to my brother, Salah Karam. Your unwavering support, encouragement, and presence throughout this journey have meant more to me than words can express. You stood by me during the most challenging moments, offered your support when I needed it most, and gave me strength when I felt weak. This achievement would not have been possible without your constant belief in me.

I also wish to thank Chrestaina and Sarkaft, whose kindness, empathy, and continuous support helped me navigate the many ups and downs of this journey. Your positivity and care made a tremendous difference.

Wijdan Karam,
York,
November 2025.

Declaration

I declare that this thesis is a presentation of original work and I am the sole author. This work has not previously been presented for an award at this, or any other, University. All sources are acknowledged as References.

Parts of this thesis have been published as:

1. **Wijdan K. Alsaedi**, Hamed Ahmadi, Zaheer Khan, and David Grace. **"Spectrum Options and Allocations for 6G: A Regulatory and Standardization Review."** *IEEE Open Journal of the Communications Society*, vol. 4, pp. 1787–1812, 2023. DOI: 10.1109/OJCOMS.2023.3301630.

   Chapter 2 is based on this publication.

2. **Wijdan K. Alsaedi**, Ahmed Al-Tahmeesschi, Zaheer Khan, David Grace, and Hamed Ahmadi. **"Analysis of Coverage Probability in 6G Millimeter-Wave Cellular Networks: Impact of Alignment Information Availability."** *IEEE Access*, vol. 13, pp. 210117–210133, 2025. DOI: 10.1109/ACCESS.2025.3632852.

   Chapter 3 is based on the this publication.

List of Tables

List of Figures

Contents

Chapter 1

Introduction

To meet the expected increase in data traffic, exploring new bands at higher frequencies has been a common approach in every new generation of wireless communication technology. For example, fifth generation (5G) cellular systems have integrated mmWave bands, specifically the FR-2 frequency range, which spans from 24.25 GHz to 52.6 GHz [1, 2]. Emerging 6G standards are expected to utilize a wide range of frequencies, from traditional sub-6 GHz bands to higher frequency ranges including mmWave, THz and optical spectrum (e.g. visible light (VL)). Using a broad spectrum, especially higher-frequency bands, supports 6G applications that demand ultra-high data rates, massive connectivity, and low-latency services such as XR services, autonomous systems, and holographic telepresence. However, higher-frequency bands pose unique challenges, such as severe path loss, high sensitivity to blockage, hardware complexity, and strict beam alignment requirements [1].

In addition to these technical challenges, regulation and standardization play a crucial role in the deployment of 6G networks. Efficient spectrum management is essential to ensure the optimal allocation and use of scarce frequency resources. Understanding the features, limitations, and potential applications of higher-frequency bands, together with the regulatory frameworks that govern them, is therefore essential to ensure the practical deployment of 6G networks.

The use of ultra-large-scale antenna arrays at both the transmitter and the receiver, combined with directional beamforming, compensates for severe path loss by generating narrow directional beams with a strong beamforming gain [3–5]. Nevertheless, such highly directional beams are inherently vulnerable to misalignment and link blockage, especially when faced with environmental and mobile obstacles [6–8]. Misalignment can significantly degrade system performance and is often attributed to antenna hardware imperfections, beamforming limitations, and mobility-induced challenges [9]. As a result, maintaining reliable and consistent coverage in dense and large-scale deployments of beyond 5G (B5G) and 6G networks requires accurate and robust beam alignment, which remains a major open challenge.

In directional mmWave communications, many studies assume perfect beam alignment [10–12]. However, a growing body of research has investigated the impact of beam alignment errors [13–19], which represent a critical challenge in practical mmWave systems. Previous studies typically model alignment errors using a truncated Gaussian distribution with fixed angular boundaries and either an arbitrarily chosen standard deviation or one derived from Cramér-Rao lower bound (CRLB). Although, CRLB-based models provide valuable analysis of specific misalignment scenarios, their reliance on estimator-specific variance assumptions limits the representation of the full range of alignment uncertainty. To address these limitations, a unified probabilistic beam alignment error model is proposed, based on a novel alignment information parameter, an abstract parameter quantifying directional knowledge availability in the system. This parameter governs both the variance and truncation boundaries of the alignment error distribution, enabling a continuous representation that transitions between a uniform distribution (no directional knowledge), truncated Gaussian (partial knowledge), and a distribution approaching a Dirac delta function (near-perfect knowledge). The model also incorporates a hardware inefficiency factor that, together with the information parameter, controls the error variance.

The analytical framework considers both omni-antenna and directional user antenna configurations. The special case analysis focuses on the scenarios where only the base station (BS) performs beamforming.

Moreover, to make coverage probability analysis tractable when using a more realistic antenna model, a continuous antenna gain pattern is approximated by discretizing it into finite intervals. This approach replaces intractable integrals in coverage probability analysis with finite summations while capturing the effects of beam alignment errors and the realistic antenna model.

1.1 Research Questions

The main research questions addressed in this thesis are:

Question 1. What are the spectrum options and the regulation considerations in 6G networks?

Question 2. How does the availability of alignment information at the serving base station affect downlink coverage probability in mmWave networks?

Question 3. How do alignment information thresholds relate to beamwidth choice and resulting downlink coverage in mmWave networks?

Question 4. How do different user antenna configurations, specifically omni-antenna versus directional antenna, impact downlink coverage in mmWave networks?

Question 5. How does employing a realistic antenna pattern (cosine model with discrete gain approximation) affect downlink coverage under beam alignment errors compared to the flat-top antenna model?

1.2 Thesis Structure and Contributions

The structure of this thesis is organized to address the research questions outlined above. The following chapters summarize the key contributions:

- **Chapter 2:** Reviews 6G spectrum options with a focus on spectrum management, examining existing approaches used in 5G and their applicability in 6G, including the role of spectrum sharing. This chapter also explores the potential use of higher-frequency bands, including mmWave, THz, and optical spectrum, and analyzes their features, limitations, potential applications, and ongoing standardization efforts, providing a comprehensive understanding of the spectrum options available for 6G. This chapter establishes the analytical basis for understanding how spectrum availability and regulatory frameworks shape the spectrum landscape relevant to 6G deployment.
- **Chapter 3:** Develops a probabilistic beam alignment error model for mmWave networks with an omni-antenna user, introducing an align-

ment information parameter that jointly governs variance and truncation boundaries of the error distribution, allowing for a unified representation of all alignment regimes. The model incorporates a hardware inefficiency factor to account for antenna imperfections. Using stochastic geometry, analytical expressions for downlink coverage probability are derived under alignment errors and validated through Monte Carlo simulations. Additionally, Monte Carlo simulations compare Rayleigh, Rician, Nakagami, and non-fading models under both line-of-sight (LOS) and non-line-of-sight (NLOS), confirming that Rayleigh fading serves as a tractable lower bound for coverage analysis in mmWave networks.

- **Chapter 4:** Extends the framework of Chapter 3 to scenarios where the user is equipped with a directional antenna. Using stochastic geometry, analytical expressions for downlink coverage probability are derived under alignment errors and validated through Monte Carlo simulations. The analysis examines the effects of serving base station beamwidth configurations, base station density, fading models, and different path loss exponents.

- **Chapter 5:** Introduces a discrete-gain approximation method that discretizes the main and side lobes, replacing complex integrals with finite summations. It incorporates probabilistic beam alignment errors, enabling coverage analysis in mmWave networks. The method is applied to a cosine antenna model, providing a more realistic evaluation than the flat-top antenna model and allowing closed-form coverage probability expressions for special cases.

- **Chapter 6:** Concludes the thesis and outlines directions for future work.

Chapter 2

Literature Review: 6G Spectrum Options and Standardization

2.1 Background

In recent years, a myriad of use cases for mobile communication have emerged due to constantly evolving societal needs [20]. These include a wide range of applications, such as XR services (augmented reality (AR), mixed reality (MR), and virtual reality (VR)), telemedicine, haptics, flying vehicles, brain-computer interfaces (BCI), connected autonomous systems, holographic telepresence, tele-surgery, and digital twins (DTs) [21–24]. Furthermore, the underlying demand for mobile data traffic/wireless connectivity has increased exponentially [25]. This trend of exponential growth in data demand is expected to continue, and the total mobile data traffic will reach five zettabytes (ZB) per month by 2030 as estimated by International Telecommunication Union (ITU) [25, 26]. In terms of use cases, 5G differs from previous generations by expanding the domain of mobile services from humans to things, as well as from consumers to vertical industries [27]. This expansion has led to the integration of millions of sensors in various environments such as cities, vehicles, homes, industries, food, and games to create a smart living spaces and automated systems [25]. However, the full potential of emerging Internet of Everything (IoE) applications will require a convergence of communication, sensing, control, and computing functionalities that are not fully addressed by 5G technology [28]. Moreover, some emerging applications in XR services and connected autonomous systems may require microsecond-level latency and Terabits-per-second (Tbps) level data rates, and achieving such high-performance requirements may be a challenge when solely relying on 5G networks [20]. To address the limitations and bottlenecks of 5G networks, 6G is expected to shift the focus from "connected things" to "connected intelligence", which requires more advanced technologies [29, 30]. This shift leads to higher capacity requirements because services move from conventional data transmission to continuous real-time information exchange for sensing, processing, and decision-making, resulting in higher traffic loads. It also increases the need for spectral efficiency to accommodate this traffic within limited spectrum resources. To achieve a wider bandwidth to meet the advanced expected use cases in 6G, it will be necessary to exploit a vast spectrum range, including all bands used by the previous cellular networks generations, including higher frequency bands in mmWave than the one allocated for 5G networks (i.e., FR1, FR2), THz and optical bands (e.g., VL). Flexible frequency sharing technology can also be employed in 6G to optimize spectrum utilization [31]. Policymakers are actively seeking ways to facilitate spectrum sharing among operators and service providers, and this has led to the exploration of more flexible licensing approaches such as licensed shared access (LSA) and spectrum access system (SAS), which rely on tiered access models beyond traditional spectrum allocation methods (e.g., administrative approach) [32], [33]. LSA and SAS adopt a regulated sharing paradigm where spectrum access is coordinated through databases and predefined licensing rules, enabling controlled spectrum sharing between incumbents and new entrants. Unlike cognitive radio, which relies on distributed spectrum sensing and opportunistic access to underutilized bands, these frameworks are based on centralized coordination and policy-controlled access mechanisms.

2.2 Spectrum Management Approaches

Spectrum management, as defined by the ITU, refers to the set of administrative and technical procedures aimed at ensuring the effective and efficient use of the radio frequency spectrum by all radiocommunication services identified in ITU radio regulations (RRs) while ensuring that radio systems operate without causing harmful interference [34]. Spectrum management can also be defined as the government function that organizes and regulates the utilization, allocation, and assignment of blocks of frequencies (a particular frequency band) to promote efficient use of spectrum, and minimize interference between users in neighboring bands [35]. In general, spectrum management decisions are made by regulators [36], and these decisions are related to who, where, when, how, and for what purpose to use a particular frequency band [37]. To be specific, spectrum allocation decisions are taken at an international level, while national regulatory authorities (NRAs) make decisions on spectrum assignment by balancing a set of public policy objectives [38]. There is a diversity of spectrum management approaches which regulators can employ for spectrum assignment, and these approaches have evolved from administrative allocation to market-based mechanisms, and unlicensed commons approaches [39]. Next, we briefly review these approaches.

2.2.1 Administrative Command-and-Control Approach

Administrative allocation or a hierarchical command-and-control approach has been the predominant method of spectrum management, through which regulators have implemented a fixed allocation of spectrum to a given entity through beauty contests or direct awards for decades [39]. Accessing spectrum by following this method leads to difficulties in meeting the increasing demand for spectrum based-wireless services [40]. In addition, this traditional approach of spectrum management has exposed some critical barriers over time, such as inefficient utilization of spectrum, political influence and a lack of economic justification [41]. Although it has been instrumental in reducing harmful interference between the different wireless systems and in supporting expansion of a few services like Global System for Mobile Communications (GSM) worldwide through coordination and harmonization [42]. Administrative allocation has continued to be used by national regulatory authorities in some countries for awarding third generation (3G) and fourth generation (4G) spectrum [36], whereas this trend is used for spectrum grant in local 5G networks [37]. However, this approach has faced criticism over the fairness of decision-making by regulators [36]. As a result of the shortcomings of this approach in accommodating spectrum demands for new wireless use cases, inflexibility in responding to changing market conditions and technological advances, in addition to creating high barriers to entry for small businesses and new entrants. Therefore, it is likely that this approach will become less dominant in the 6G and beyond. However, national regulators have adopted more flexible approaches to spectrum management, such as market-based mechanisms that can better accommodate the needs of new wireless use cases and promote greater competition in the industry.

2.2.2 Market-Based Mechanisms

Market-based mechanisms represent the second generation of radio spectrum management approaches. The primary regulatory objective of these methods is to promote static efficiency by ensuring optimal allocation of radio spectrum [41]. Market-based mechanisms can introduce flexibility into the market by allowing the spectrum to be shared through secondary spectrum markets, where license holders have the opportunity to lease or trade unused or underutilized portions of their spectrum [36]. Within this approach, spectrum property rights are established through the issuance of licenses to a limited number of applicants via market mechanisms [39, 43]. Under this licensing approach, the licensee is granted exclusive rights to use a specific spectrum within a defined geographical area. Technical regulations are put in place to govern usage rights and prevent interference among spectrum users. Additionally, licensees are allowed to trade or lease their rights to third parties [44, 45]. In particular, spectrum property rights are determined through spectrum auctions, where licenses are awarded on the basis of bids between competing applicants [41]. From the viewpoint of regulations and policies, spectrum auctions offer an effective means of allocating spectrum to the entities that value it most, while also generating revenue for governments [46]. Compared to administrative procedures, auctions are generally preferred as they ensure more efficient distribution of the limited spectrum resource, especially in cases where demand exceeds supply [38]. However some of the challenges encountered in this approach are that auctions do not always leads to superior market outcomes due to unanticipated problems in their design leading to unexpected bidder behavior such as collusion and over-bidding [46, 47]. To mitigate these challenges, regulators need to recognize the complex relationship between spectrum management and market outcomes [39]. One approach is using learning algorithms to predict bids and also detect anomalies [48].

Regulatory authorities have various instruments at their disposal that can be utilized during auctions to achieve efficiency goals based on specific national circumstances. These tools include, but are not limited to, spectrum packaging, license duration, geographical scope, and obligations [38]. In fact, auctions have become the main mechanism for granting spectrum usage rights to mobile operators for deployment of 3G, 4G [39], and 5G networks [38]. The trend of using market-based mechanisms for spectrum management is expected to continue in 6G, with increasing complexity in the design of auctions due to the wide range of spectrum bands (low, mid, and high) that will be utilized, along with coverage obligations, spectrum trading, and other factors. More details on this topic will be provided in Section 2.3

2.2.3 Unlicensed Commons Approach

An unlicensed commons approach, also known as a licence-exempt approach, provides access to the a portion of the radio spectrum without the need for a license or registration [41]. In this approach, different wireless systems operate in the same frequency band (share the same spectrum) under rules and conditions defined by the national regulator [49]. The licence-exempt operation uses the Industrial, Scientific, and Medical (ISM) bands [50]. The most notable example of such use is the 2.4 GHz spectrum to provide Wireless Fidelity (WiFi) access services [51]. Traditionally, the Institute of Electrical and Electronics Engineers (IEEE) 802.11/ WiFi family of standards, including (802.11b/g) at 2.4 GHz, (802.11a/n) at 5 GHz, and (802.11ad/ay) at 60 GHz, have been designed to operate in license-exempt bands and without the need to obtain a license from the regulatory authorities. Similarly, cellular technologies can also operate in one or more of these unlicensed spectrum bands [52].

Various standardization bodies and industry alliances, such as the 3rd Generation Partnership Project (3GPP) and the IEEE, have made significant efforts to develop technologies that enable cellular networks to operate in these unlicensed frequency bands. These efforts have led to the creation of technologies such as Long Term Evolution unlicensed (LTE-U), License Assisted Access (LAA), MulteFire, and New Radio Unlicensed (NR-U), which allow cellular networks to share frequency bands with other wireless technologies. These technologies offer potential benefits such as increased network capacity, improved coverage, and new use cases for cellular connectivity [49]. In general, the unlicensed commons approach is built entirely on spectrum sharing, where multiple different types of wireless systems and several deployments of the same systems use the same unlicensed band [39]. Coexistence of WiFi and cellular networks in the unlicensed spectrum is another example of this approach [53]. From a technical perspective, the coexistence of WiFi and cellular networks can increase the overall capacity of heterogeneous wireless networks, provided that the mutual interference between WiFi and cellular systems is addressed properly [53]. In particular, the main challenges of allowing cellular networks to operate in the unlicensed spectrum is ensuring a fair coexistence with other unlicensed systems and avoiding interference [54]. One approach to achieving fair coexistence and avoiding interference requires compliance with regulatory requirements, which include using a Listen-Before-Talk (LBT) mechanism to access the channel [55, 56]. Technologies designed for spectrum sharing in unlicensed bands, such as LTE-U and NR-U avoid interference with neighbor networks by using a LBT mechanism to detect and avoid WiFi transmissions in the same band [57]. Under this approach, potential gains from unlicensed use include eliminating the requirement for the administrative licensing that would lower barriers to market entry [44]. However, ISM bands have not been very attractive for cellular networks due to their associated interference environment, which can lead to unpredictable quality of service (QoS) [42, 50].

Moreover, incorporating unlicensed spectrum management techniques in higher frequency bands, including mmWave, presents additional complexities for ensuring coexistence. These challenges arise primarily from the propagation characteristics of mmWave signals, such as severe path loss and susceptibility to blockage, which require highly directional beam-based transmissions. As discussed in [55], beam-based transmissions significantly change the coexistence framework due to the use of directional antennas. Consequently, conventional LBT sensing is limited to narrow spatial regions, reducing the ability to reliably detect concurrent transmissions and exacerbating hidden and exposed node problems, thereby complicating interference management. The coexistence of cellular and Wireless Gigabit (WiGig) users over unlicensed mmWave bands poses several challenges, as highlighted in another study [58]. Specifically, the study addresses the challenges of directional transmission and high propagation loss in cellular communications. It emphasizes that mmWave signals, due to their short wavelength, exhibit directional transmission characteristics and suffer from significant propagation losses. To overcome these challenges, the study emphasizes the importance of implementing hybrid beamforming techniques. By using hybrid beamforming, the transmitting power can be concentrated in desired directions, thus maximizing the signal strength and improving overall system performance. This effective beam management approach is crucial to fully exploiting the spatial resources available in the unlicensed mmWave spectrum for cellular communications. The study's findings underscore the significance of addressing these challenges and implementing appropriate coexistence mechanisms to ensure the harmonious coexistence of cellular and WiGig users in the unlicensed mmWave bands.

These challenges emphasize the importance of conducting research, establishing standards, and implementing regulatory measures to tackle/address the specific complexities of coexistence in higher frequency bands. Developing solutions and optimizations in areas such as node coordination, interference management, channel access, and beamforming will be vital to enabling successful coexistence between different systems operating in the mmWave spectrum. It is worth noting that these difficulties are not limited solely to the mmWave bands but serve as an example of the challenges encountered in higher frequency bands in general.

2.2.4 Spectrum Sharing in 6G

In the past fifteen years, numerous studies have investigated the efficiency of spectrum utilization, and the findings have consistently revealed that certain portions of the spectrum allocated or assigned with exclusive usage rights are not being utilized to their full potential [56]. As such, an appropriate spectrum resource management scheme is critical for dealing with the conflict between the huge demand for mobile data traffic (e.g., Internet of Things (IoT) connections) and limited spectrum resources, accommodating use cases in future generations (e.g., 6G) and improving performance [59]. According to a study from Europe, around 76 GHz spectrum resource is needed (to accommodate mobile data traffic) if the spectrum is exclusively used in 5G networks [59, 60]. Nevertheless, this amount can be significantly reduced to 19 GHz by adopting spectrum sharing [59, 60]. Consequently, new models for spectrum access rights have emerged, with the general aim of allowing more dynamic access to the spectrum [56].

Recent examples of emerging models are licensing-based sharing which includes the LSA developed in Europe and SAS developed in the U.S [39]. The ongoing standardization process for LSA and SAS follows the European Conference of Postal and Telecommunications Administrations (CEPT) recommendations, with a focus on the 2.3 GHz band, which is considered as supplementary spectrum for mobile operators [32]. This band has been globally allocated to mobile services and designated for International Mobile Telecommunications (IMT) use [61]. LSA is a regulatory concept specific to the European region that enables opportunistic access to the spectrum through the use of databases, with a primary focus on the (2.3 – 2.4) GHz frequency range for initial deployment [62]. Several regional regulatory and standardization organizations, including the Electronic Communications Committee (ECC), CEPT, European Telecommunications Standards Institute (ETSI), European Commission (EC), and the Radio Spectrum Policy Group (RSPG) of the European Union, have contributed to the development of the concept of LSA by establishing the necessary regulatory framework [61, 62].

In 2013, the RSPG defined the LSA concept as a *"regulatory approach aiming to facilitate the introduction of radio communication systems operated by a limited number of licensees under an individual licensing regime in a frequency band already assigned or expected to be assigned to one or more incumbent users. Under the LSA approach, the additional users are authorized to use the spectrum (or part of the spectrum) in accordance with sharing rules included in their spectrum rights of use, thereby allowing all authorized users, including incumbents, to provide a certain QoS"* [41, 63]. The sharing of licensed spectrum is facilitated by the two-tier framework of the LSA access model [64]. In the first tier, incumbent users are guaranteed protection of their spectrum and the option to monetize any unused spectrum. The second tier involves secondary LSA licensees who are granted short-term access to the underutilized spectrum licensed by the incumbents, with a guaranteed quality of service [64]. Under the LSA approach, regulators have the flexibility to decide on the spectrum assignment methods used to grant LSA licenses [39]. Furthermore, through the LSA framework, spectrum resources can be shared across different dimensions, such as frequency, time, and geography [65]. The sharing framework involves a series of terms and conditions that are mutually accepted by the incumbent user, the licensee of the LSA, and the national regulatory authority (NRA) [66]. These conditions are determined at the national level and the license agreements can vary significantly between countries [66]. The LSA framework grants exclusive access to the spectrum for LSA licensees when the incumbent is inactive and protects against potential interference from other LSA licensees or incumbents, thus ensuring that a predictable level of QoS is maintained [67].

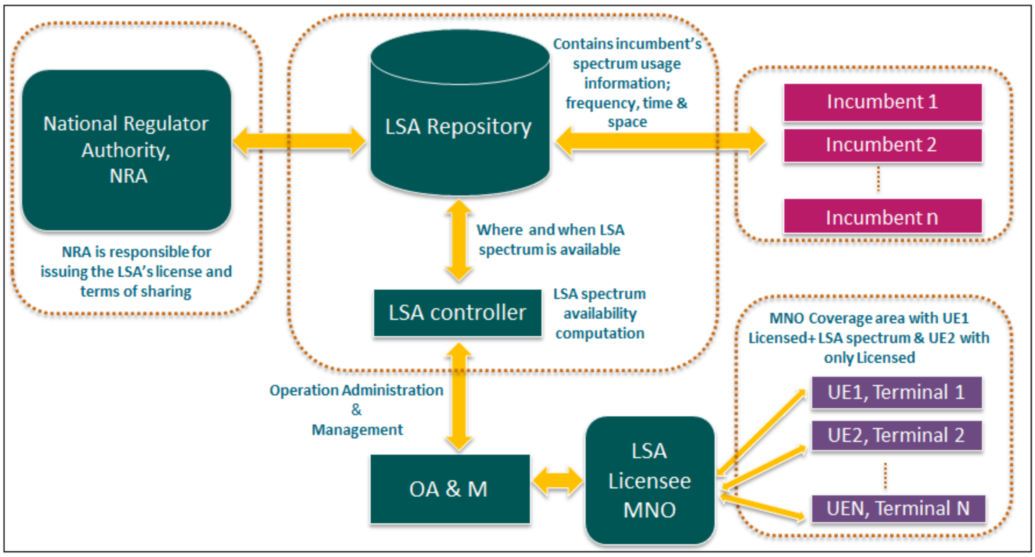

Figure 2.1: LSA Framework, in LSA, incumbent users are primary license holders who have exclusive rights to use a specific portion of the radio spectrum. New users, such as mobile network operators (MNOs), can request access to the spectrum in areas where it is not being fully occupied by the incumbent users.

In general, the LSA framework relies on a centralized database that is generated by leveraging previous usage information provided by authorized users [68]. As shown in Figure 2.1 [69], the LSA Repository (LR), is a centralized database that stores information related to incumbent protection [70]. The LSA Controller (LC) is another critical component of the LSA framework, which obtains the LSA spectrum resource availability information (LSRAI) from the LR [70]. To be specific, the previous LSA work (2013 - 2014) mainly focused on providing additional spectrum for existing MNOs [71]. However, LSA work that began in 2017 had a different objective, which was to address temporary spectrum access for locally deployed high-quality 5G networks [71]. The main objective of high-quality wireless networks is to provide dependable and secure services and applications with predictable levels of QoS, which are limited to a specific geographic or temporal area [39]. Additionally, ETSI proposed some improvements to the LSA architecture in 2018, particularly in the LSA repository and controller, to accommodate the introduction of the third category of players [61].

LSA can be considered as a solution to facilitate the implementation of 5G applications in various vertical sectors, including industrial automation, utilities, and e-health [61]. In particular, the LSA sharing framework is being explored for feasibility in the (3.4 – 3.8) GHz band to allow for coexistence between incumbent services, including satellite systems, and emerging 5G use cases [61]. This second use case for LSA in European regulation differs from the first (2.3 GHz band) due to the more static nature of the incumbent usage on the band, which may require different implementation and tools for LSA [66].

SAS is another database sharing model introduced by the Federal Communications Commission (FCC), which supports spectrum sharing with a three-tier/layer hierarchical regulatory model [36, 70, 72]. The FCC has introduced SAS to provide citizens broadband radio service (CBRS) on a shared basis in the 3.5 GHz band [32, 71]. Initially, CBRS was used exclusively by the US Federal Government for Navy radar systems and commercial satellite operators [70]. The CBRS system is structured into a three-tier framework [73]. The highest tier is the incumbent access tier, occupied mainly by federal government entities, who receive the most protection from interference from other CBRS users [66]. The second tier consists of commercial users who have been granted Priority Access Licenses (PALs) by the NRA [49]. The PAL users in the second tier are also entitled to receive protection against the lower-tier users in order to prevent harmful interference [49]. In addition to PALs, a third layer of access called General Authorized Access (GAA) has also been defined in the SAS approach, which functions similarly to the operation of users in license-exempt bands [49]. In other words, GAA users are able to utilize portions of the CBRS spectrum without incurring license fees, but they are not guaranteed protection against interference from other users [71]. In comparison to commercial users with PALs, GAA users have limited access guarantees to the CBRS spectrum under certain rules and conditions set by the regulator [49, 64]. The SAS approach offers greater flexibility compared to traditional approaches, and is designed to ensure coexistence with incumbent users, even when they cannot provide prior information to a central access database [32].

In the previous examples, the spectrum sharing models are multi-tiered sharing schemes based-on two-tiers or three-tiers, and each network has a specific/defined priority for band usage. In contrast, in single-tiered sharing schemes, all networks have the same priority to use the spectrum [73]. The examples of single-tiered sharing scheme includes:

- Spectrum commons: This type of spectrum sharing is in relation to unlicensed bands, and can be divided into two categories; (i) spectrum sharing in unlicensed bands with an anchor in the licensed bands, technologies that use sharing with an anchor are LTE-U (developed by the LTE-U Forum based on Long Term Evolution (LTE) Release 12) and LTE-LAA (Release 13, 14 and 15) [54, 57]. Both LAA and LTE-U are based on carrier aggregation (CA) to occupy licensed and unlicensed bands [55, 74]. (ii) IEEE 802.11 standards (which includes WiFi), MulteFire (developed by the MulteFire Alliance based on LTE Release 14), and NR-U (Release 16 2020) are all examples of technologies that are designed to operate standalone in unlicensed bands or shared spectrum bands without the need for a licensed band as an anchor [55, 57]. However, the high density of WiFi users in unlicensed bands poses a challenge to MNOs who adopt spectrum sharing methods, resulting in more restrictions such as the requirement to use LBT [70, 75].

- Authorized light-licensing: This type of spectrum sharing provides a more flexible regulatory framework for spectrum authorization that falls somewhere between traditional exclusive licensing and unlicensed operations [66, 76] in which a limited number of equal priority license-exempt networks can use the band temporarily upon registration [73]. Bands such as the 60 GHz (57 - 64 GHz) and 80 GHz (71 - 76/81 - 86 GHz) are reasonable options for this access mode due to their propagation characteristics that enable operations with a minimum risk of interference and high data rate capacities [76].

The LSA and the SAS spectrum sharing schemes have received significant attention as a means to rapidly access sub-6 GHz frequency bands, which are crucial for supporting 5G use cases across various vertical sectors [61]. Although spectrum sharing is considered essential for 5G, the implementation of the LSA sharing framework in the C-band in Europe remains a national decision, and European NRAs have shown limited interest in utilizing the LSA framework for 5G [61]. TV White Spaces (TVWS) represent an early example of dynamic spectrum access within the spectrum sharing framework, where unused portions of licensed television broadcast spectrum (typically in VHF and UHF bands) can be opportunistically accessed by secondary users [77]. In several regulatory frameworks, such as those adopted by the FCC in the US and Ofcom in the UK, TVWS access has been enabled through licence-exempt approaches while ensuring protection of incumbent users [78]. TVWS systems rely on geolocation database-assisted techniques to identify available channels and avoid harmful interference with incumbent broadcast services. This approach enables dynamic spectrum access and serves as a foundational example of practical spectrum sharing implementation [77]. In the US, the initial approach to managed spectrum sharing did not succeed for TVWS due to a lack of commercial demand. However, it worked well for CBRS because there was a strong demand for mid-band 5G frequencies, especially due to the lack of awards for the rest of the band until the end of 2021 (3.45 – 3.55) GHz [79]. Despite recent regulatory activities in Europe that have made the LSA and CBRS frameworks broadly similar, the LSA framework is still in its early stage of development, whereas CBRS is already being implemented [61].

From a technical standpoint, the adoption of higher carrier frequencies in mmWave, such as (24.25 - 27.5) GHz in 5G, shifts deployment models from wide coverage areas to local service areas. This shift enables more feasible spectrum sharing as potential interference is limited to local areas [39]. However, this shift also requires new spectrum assignment models that define and grant access rights for deploying 5G networks to cater to the specific needs of different verticals [39]. In 2018, ETSI published a technical report that explores the practicality of temporary spectrum access solutions for local high-quality wireless networks, which are specifically designed to be deployed in particular geographic areas for either a short or long period of time, and can be either fixed or nomadic in nature [79]. The development of 5G networks has expanded beyond the traditional MNOs-centric deployment models to alternative local network operator models, emphasizing the significance of local spectrum availability and the increasing reliance on spectrum sharing for the emergence of high-quality 5G wireless networks alongside regulatory approaches for assigning local spectrum licenses [39]. There are several practical options available to ensure spectrum access for local high-quality 5G networks. One option is to deploy them as a managed service by MNOs, which is also known as a "network slice". Another option is to create a private network that utilizes locally sub-leased MNO spectrum. Finally, a private network can be established that utilizes locally individually licensed spectrum [79].

Based on the trend observed in 5G deployment, 6G is also expected to rely on higher frequency bands, such as mmWave, leading to a similar shift in deployment models from traditional wide coverage areas, MNOs-centric networks to local service areas (e.g., local high-quality networks), which in turn will increase the reliance on spectrum sharing. Therefore, it is likely that new spectrum assignment models will need to be developed to define and grant access rights for the deployment of 6G networks.

2.2.5 Integration of Advanced Technologies for Spectrum Sharing in 6G Networks

The advancement of spectrum sharing techniques in 5G/6G networks has been driven by the integration of cutting-edge technologies such as artificial intelligence (AI) and distributed ledger technology (DLT) [73, 80–82]. These technologies provide new avenues for optimizing resource allocation, addressing the dynamic nature of wireless networks, and enhancing spectrum sharing mechanisms. AI techniques, specifically Reinforcement Learning (RL) and Deep Learning (DL), have emerged as a prominent approach to spectrum sharing. By leveraging RL and DL algorithms, intelligent spectrum allocation based on real-world data can be achieved. These algorithms have the ability to learn from past experiences, adapt to changing network conditions, and optimize spectrum utilization in real-time [82]. DLT and Machine Learning (ML) algorithms are another key focus area for efficient and secure spectrum sharing in the 6G networks [80, 81]. DLT, such as blockchain technology, can establish a decentralized and trustless environment, ensuring fairness, transparency, and security among network participants. By integrating DLT with ML algorithms, spectrum sharing mechanisms can be designed to optimize resource allocation, enable dynamic sharing among multiple stakeholders, and enhance spectrum access [81, 83]. The concept of sharing frequency bands among unlimited networks with configurable priorities and interference protection criteria is discussed in [73]. This spectrum sharing scheme emphasizes the importance of efficient resource allocation in dynamic network environments. By incorporating ML algorithms, the approach ensures fair and effective spectrum sharing among multiple networks, leading to improved overall network performance and enhanced resource utilization [84]. Additionally, blockchain-based solutions address limitations in existing spectrum sharing systems, such as three-layer spectrum system, offering a decentralized and transparent environment for optimized spectrum utilization and broader participation [80]. These advancements pave the way for more efficient and intelligent 6G networks.

In addition, the integration of advanced technologies AI/ML that improve spectrum efficiency and sharing flexibility in 6G networks is widely recognized as a key enabler for reducing end-to-end latency by supporting real-time resource allocation and minimizing centralized processing delays [85]. In particular, edge computing combined with AI/ML capabilities supports ultra-reliable and low latency communication (URLLC) by processing data closer to the data source, thereby minimizing transmission delay to distant centralized cloud servers and reducing network congestion. ML based solutions can be employed for predictive analytics, data aggregation, and data mining techniques at edge or cloud platforms to efficiently process massive data loads [86]. Computationally intensive tasks can be executed at edge or cloud nodes rather than centralized servers, improving response time and supporting real-time applications, and alleviating network bandwidth consumption [86, 87].

2.3 Spectrum Management Approaches in 5G and Future Directions for 6G

The main European bands for 5G include 700 MHz, 3.5 GHz and 26 GHz, and many countries in Europe have completed their spectrum awards for 5G in these frequency bands [37]. In a case study of the 3.5 GHz band in different countries, national regulators have adopted very different approaches in their 5G spectrum awarding decisions . The study showed that all three spectrum management approaches are still in use including administrative allocation (Japan), market-based mechanisms (Finland, Germany, Ireland, Italy, USA) and the unlicensed commons approach (USA) [39]. According to this study, it is clear that a market based mechanism is the preferred approach in awarding 5G spectrum by many regulators, due to the fact that the auction is a transparent mechanism for assigning licensed spectrum and generating revenue for the government. Furthermore, we can also infer from this study that different regulators may have different priorities and considerations when deciding on the approach to awarding 5G spectrum. Furthermore, an analytical study of European auctions of C-band (3.4 - 3.8) GHz for 5G between 2017 and 2020 in [38], shows that the market-based mechanism method was adopted in sixteen European countries. In this approach, regulators adopted different types of auctions formats for spectrum grants such as the simultaneous multiple round (ascending) auction (SMRA), the clock auction, and the combinatorial clock auction (CCA). Moreover, according to this study, there is no consistent pattern observed in the auctions analyzed with regard to the instruments used to improve efficiency and equity. The SMRA format was

Table 2.1: Approaches for managing spectrum in the context of 5G networks [37]

Assigning and Licensing Spectrum Resources Framework	Choices Made in 5G Deployment	Consideration at a Local Network Level
Administrative Approach	This method is rarely used for spectrum granting in 5G, but it has regained its significance in spectrum awarding to local 5G networks.	The awarding of spectrum is carried out on a first come first served basis.
Market-based Mechanisms	Auctions, which rely on a market-based mechanism, are the dominant method of assigning spectrum licenses in 5G. MNOs obtain licenses through these auctions.	MNOs have the choice of leasing or trading their allocated spectrum to third-party entities for the purpose of establishing local networks.
Unlicensed Commons	This approach is one of the operational methods available for 5G.	Unlicensed deployment of networks is possible if regulatory requirements for the band are met.

found to be the most widely used auction format for the C-band, adopted by seven countries. However, some countries have modified the auction format they use, such as SMRA, CA, or CCA, to prevent ineffective outcomes such as fragmented or unsold spectrum [38].

Overall, recent developments and decisions regarding 5G spectrum indicate that a diversity of spectrum management approaches are now being included into mobile networks in great contrast to previous generations of cellular networks, and this trend is expected to continue towards the 6G era [36, 37]. Moreover, spectrum sharing is expected to play an increasingly important role in the future, particularly to allow the deployment of 5G networks in new spectrum bands that are likely to have incumbent spectrum users, whose rights need to be protected [39]. Table 2.1 summarizes the various spectrum management approaches in the context of 5G, with an emphasis on how local networks are considered [37].

The development of 6G is expected to entail significant changes that will build upon the progress achieved in 5G and elevate it to a higher level. This transformation will involve converting the radio communication network from relying solely on electronic technologies to a hybrid system that also takes advantage of optical and photonic free-space technologies in order to exploit the abundant spectral resources in terahertz and visible light bands, to meet the growing demand for higher system capacity and peak data rates [27]. This shift towards hybrid radio frequency (RF)–optical/photonic architectures implies that future spectrum management will no longer be confined to a single RF framework, but will need to manage multiple physical transmission domains with fundamentally different propagation characteristics and coexistence requirements. Unlike conventional RF systems, where spectrum management mainly focuses on frequency allocation and interference mitigation, hybrid systems introduce additional complexity due to the integration of RF, THz, and optical spectrum resources, each with different coverage characteristics, interference conditions, and deployment constraints. As a result, spectrum management in 6G is expected to expose a new level of complication that arises from the diversity of spectrum bands (e.g., mmWave, THz, and VL), and thus 6G technology will need the flexibility to operate in multiple bands under different spectrum management approaches [36]. Moreover, these frequencies have different propagation characteristics and may require different sharing mechanisms compared to traditional microwave bands. Additionally, 6G is expected to integrate terrestrial mobile communication networks, satellite communications, aerial, and maritime communications to realize ubiquitous coverage, whereas radio coverage is mainly limited to terrestrial mobile communication in all previous generations. These new paradigm shifts compared to previous mobile generations are leading to new use cases, create new business models, and will transform many aspects of society. As a result, regulators needs to rethink current spectrum management approaches and policies to align with the developments in future 6G network models.

2.4 Spectrum Options: Radio and Light

The demand for higher peak rates and capacity in mobile communication systems has driven the exploration of higher spectrum bands. For 5G networks, new spectrum bands ranging from 3 GHz to 6 GHz and mmWave bands ranging from 24 GHz to 50 GHz have been allocated, with additional bands expected to be allocated as 5G evolves [88]. However, the next generation of applications, such as holographic videos, VR, and ubiquitous connectivity, will require even higher bandwidth than what can be supported by the mmWave band alone [89]. The trend toward higher frequency operation is anticipated to continue with 6G systems, which are expected to exploit subterahertz and terahertz, surpassing the spectral ranges utilized in 5G and enabling data rates 100 to 1000 times faster [90]. In this context, researchers are exploring new spectrum options for future 6G and beyond networks, such as higher mmWave frequencies, THz bands and optical spectrum, including the VL, infrared (IR), and ultraviolet (UV) bands, to address the high traffic demands [91, 92]. In the following subsections, we examine these frequency bands and their characteristics in more detail.

2.4.1 mmWave Band

The classical sub-6 GHz cellular bands have become extremely crowded and cannot support the massive increase of communication capacity alone [93]. In response to the growing demand for wireless data and the increasing congestion in the traditional sub-6 GHz bands, regulators have been exploring new spectrum at higher frequencies above the sub-6 GHz range. These higher frequencies include the centimeter-wave (cmWave) ranges from 3 to 30 GHz, and the mmWave bands ranges from 30 to 300 GHz, which have the potential to provide abundant spectral resources while enabling wider carrier bandwidths of up to 1 GHz [94]. The cmWave band is generally referred to as the super high frequency (SHF) band, and the mmWave band is also referred to as extremely high frequency (EHF). The spectrum from 3 GHz to 300 GHz is also collectively called mmWave bands with wavelengths ranging from 1 to 100 mm, as the radio waves in the SHF and EHF bands share similar propagation characteristics [95, 96]. Despite the abundance of spectrum resources in the mmWave band, not all frequency bands within this range are used in practical wireless cellular communication systems [97]. Some frequency bands in the mmWave range are underutilized or not used at all for various reasons, such as technical limitations, regulatory restrictions, and the lack of suitable equipment. These limitations arise mainly from the inherent propagation characteristics of mmWave signals, such as high path loss and sensitivity to blockage, as well as practical hardware constraints related to antenna array implementation and RF chain complexity, which increase cost and reduce large-scale deployment feasibility. Examples of underutilized mmWave frequency bands include [97];

- 28 / 38 GHz is licensed but underutilized with available bandwidth in total 3.4 GHz.
- 57 - 64 GHz is unlicensed with available bandwidth in total 7 GHz.
- 71 – 76 GHz, 81 – 86 GHz, and 92 – 95 GHz is light licensed with

Table 2.2: Candidate mmWave Bands for IMT-2020 Considered in WRC-15 [97], [98]

Frequency Range (GHz)	Radio Communication Service			Allocation Band Mainly for Mobile Service ?
	Shared with Fixed Service	Shared with Fixed Satellite Service	Shared with Space Radio Communication	
24.25 - 27.5	-	-	-	✓
31.8 - 33.4	(31.8 - 33.4) GHz	-	-	✗
37 - 40.5	(37 - 40) GHz	(39 - 40) GHz in Region 1, (40 - 40.5) GHz worldwide	-	✓
40.5 - 42.5	(40.5 - 43.5) GHz	(40.5 - 42) GHz in Region 2	-	✗
42.5 - 43.5	(40.5 - 43.5) GHz	-	-	✓
45.5 - 47	-	-	(43.5 - 47) GHz	✓
47 - 47.2	-	-	-	✗
47.2 - 50.2	-	(47.5 - 47.9), (48.2 - 48.54), and (49.44 - 50.2) GHz in Region 1. (48.2 - 50.2) GHz in Region 2	-	✓
50.4 - 52.6	(51.4 - 52.6) GHz	-	-	✓
66 - 76	-	-	(66 - 71) GHz	✓
81 - 86	-	-	-	✓

available bandwidth in total 12.9 GHz.

Efforts to allocate mmWave spectrum for cellular communications were initiated by the ITU- Radiocommunication (ITU-R) sector through the World Radiocommunication Conference (WRC) in 2015, as several frequency bands were proposed for discussion in WRC- 2019. Further details are discussed in the following subsection.

2.4.1.1 Spectrum Regulation of mmWave for Cellular Communication

At the WRC-15, the ITU-R sector suggested 11 potential frequency bands between 24.25 GHz and 86 GHz, to assess the feasibility of coexistence between IMT and existing services like fixed and satellite services, both in shared and adjacent frequency bands [99]. These candidate frequency bands were further discussed during the WRC-19, and their details are presented in Table 2.2 [98]. Additionally, Table 2.3 provides information on the allocation of frequency bands within the range of 52.6 – 116 GHz ITU-R, including details on the frequency band, allocation status, and primary services authorized to use each band [97]. Furthermore, there are several regions that are also promoting 5G development in the mmWave spectrum in addition to the ITU-R process [99]. More details on this are provided in the following:

- The FCC in the USA has allocated large bandwidths in the mmWave bands for 5G development, including 3.85 GHz of licensed spectrum in the (27.5 – 28.35) GHz and (37 – 40) GHz bands (with 37 – 37.6 GHz allocated to 5G on a shared basis), as well as 7 GHz of unlicensed spectrum in the (64 – 71) GHz band [98]. Additionally, there is a 12.9 GHz band from the E-band located at (71 – 76) GHz, (81 – 86) GHz, and (92 – 95) GHz [9, 96]. Although these choices do not fully align with the ITU plans, the FCC is considering the possibility of opening up to 18 GHz of additional spectrum in all ITU candidate bands, except for (42.5 – 47.2) GHz [98].

- In the UK, the pioneer band centered at 26 GHz has been released by The United Kingdom Office of Communications (Ofcom) for potential 5G use ranging between (24.25 – 27.5) GHz [96].

- China has been exploring the use of frequency bands around 45 GHz for both licensed and unlicensed communication systems, including 5G applications [96]. Within these bands, spectrum between (40.5 - 42.3) GHz and (48.4 - 50.2) GHz has been designated for fixed point-to-point wireless access systems with light license management, and the spectrum between (42.3 - 47) GHz and (47.2 - 48.4) GHz has been allocated for mobile point-to-point wireless access systems with unlicensed management [100].

Table 2.3: Frequency bands between 52.6-116 GHz as defined in the Radio Regulations [97]

Frequency Range (GHz)	Service	Is the Mobile Service allocated as the primary user in this frequency band?	Notes
52.6 - 54.25	Earth Exploration Satellite Service (Passive)/ Research Service (Passive)	✗	Emissions prohibited
54.25 - 55.78	Earth Exploration Satellite Service (Passive)/ Research Service (Passive)	✗	-
55.78 - 59	Earth Exploration Satellite Service/ Research Service (Passive)/ Fixed Service	✓	High-density applications
59 - 59.3	Earth Exploration Satellite Service (Passive)/ Research Service (Passive)	✓	-
59.3 - 64	Radiolocation	✓	-
64 - 65	Fixed Service	✓	High-density applications
65 - 66	Fixed Service	✓	High-density applications
66 - 71	-	✓	Frequencies listed under agenda item 1.13 of WRC-19 are undergoing compatibility studies with potential limitations.
71 - 76	-	✓	Frequencies listed under agenda item 1.13 of WRC-19 are undergoing compatibility studies with potential limitations.
76 - 81	Radiolocation	✗	-
81 - 86	-	✓	Frequencies listed under agenda item 1.13 of WRC-19 are undergoing compatibility studies with potential limitations.
86 - 92	Earth Exploration Satellite Service (Passive)/ Research Service (Passive)	✗	Emissions prohibited
92 - 94	Radiolocation	✓	-
94 - 94.1	Radiolocation	✗	-
94.1 - 95	Radiolocation	✓	-
95 - 100	Radiolocation	✓	-
100 - 102	Earth Exploration Satellite Service (Passive)/ Research Service (Passive)	✗	Emissions prohibited
102 - 105	Not Applicable	✓	-
105 - 109.5	Research Service (Passive)	✓	-
109.5 - 111.8	Earth Exploration Satellite Service (Passive)/ Research Service (Passive)	✗	Emissions prohibited
111.8 - 114.25	Research Service (Passive)	✓	-
114.25 - 116	Earth Exploration Satellite Service (Passive)/ Research Service (Passive)	✗	Emissions prohibited

2.4.1.2 mmWave Features and Limitations

Abundant spectral resources in mmWave bands offer a promising solution to satisfy QoS requirements of wireless communications beyond 5G and 6G such as multi-Gigabits per second (Gbps) peak throughput, ultra-reliable delivery, and end-to-end latency at the order of 1 ms, and thus the adoption of mmWave communications brings advantages [97], including:

- Wide Bandwidth: Utilizing mmWave frequencies centered around 35, 94, 140, and 220 GHz can offer significant advantages for wireless communication,these advantages include high data rates of up to 10 Gbps and ultra-low latency of around 1 ms [100]. The larger bandwidth available in the mmWave spectrum allow for faster data transmission compared to lower frequency bands.

- Short Wavelength and Narrow Beamwidth: The use of mmWave frequencies offers the benefit of having a shorter wavelength compared to sub-6 GHz bands. This makes it possible to pack a large number of antennas into a compact array. With a greater number of antenna elements, a narrow directional beam can be achieved, which has several advantages. Firstly, it suppresses multi-path reflection, which can improve signal quality. Secondly, it provides high immunity against jamming and eavesdropping attacks, as the narrow beam is more difficult to intercept or interfere with. Lastly, it offers robustness to co-user interference, as the wireless channels will be largely uncorrelated [9, 101, 102]. These features make mmWave highly attractive for various wireless communication applications, particularly those where high data rates, low latency, and reliable connectivity are essential.

Despite the many benefits of mmWave communications, there are still several challenges that need to be addressed for effective design, deployment, and operation. These challenges arise from several limitations, including:

- Poor Propagation Characteristics: The mmWave communication system faces inherent challenges such as; high free-space path loss, atmospheric gaseous absorption, rainfall attenuation [103, 104], and sensitivity to blockage (e.g., solid construction, plants, etc.) [7, 105]. Directional beamforming and beam tracking techniques can be utilized to overcome the challenges posed by harsh propagation loss and expanding the coverage area. However, when cell sizes are reduced to enhance spectral efficiency, the impact of rain attenuation and atmospheric absorption becomes less significant for cell sizes around 200 meters. Consequently, mmWave communication is primarily used for indoor environments, small cell access, and backhaul, with cell sizes generally on the order of 200 meters [106].

- Integrated Circuits and System Design: Designing circuit components and antennas for mmWave communications can be quite challenging due to the high carrier frequency and wide bandwidth. In particular, the high equivalent isotropic radiated power (EIRP) and wide bandwidth in the higher frequency bands, such as the 60 GHz band, can potentially result in severe nonlinear distortion of power amplifiers (PA). Furthermore, the design of RF integrated circuits also faces significant challenges related to phase noise, in-phase and quadrature phase (IQ) imbalance [106].

- Industrially, the industrial production of small mmWave components involves a higher level of precision, which in turn leads to increased manufacturing costs. [100].

2.4.1.3 Spectrum Allocation for 5G New Radio (NR)

The mmWave spectrum bands are being recognized as a promising solution to deal with the high data rate and capacity requirements of 5G and beyond [72]. Compared to previous generations (e.g., 3G, 4G), 5G has the advantage of allocating mmWave bands in cellular communications [107]. In 2018, the first 5G communications standard, called new radio (NR), was defined by 3GPP in Release 15 [108]. Compared to previous generations of mobile communication systems, NR has a key feature of being able to be deployed over a much wider range of spectrum for radio access technology [55, 109]. In this regard, ITU-R and 3GPP have specified the use of two frequency ranges for 5G NR, namely FR1 and FR2, with the latter mainly using frequencies in the mmWave band [110]. In particular, FR1 is defined in the frequency range from 410 MHz to 7.125 GHz, while FR2 covers two mmWave frequency ranges: (1) from 24.25 GHz to 52.6 GHz (FR2-1), and (2) from 52.6 GHz to 71 GHz (FR2-2) [74].

In terms of maximum bandwidth in FR1 and FR2, 5G NR adopts an Orthogonal Frequency Division Multiplexing (OFDM) based waveform for both downlink and uplink with a sub-carrier spacing (SCS) of ($2^n x 15$ kHz) where ($0 \geq n \geq 3$) [111]. More specifically, NR can adopt SCS in the values (15/30/60) kHz for the data channel in FR1 with channel bandwidth up to 100 MHz, whereas for FR2, NR can only use SCS at (60/120) kHz with channel bandwidth up to 400 MHz [52, 54, 111]. Furthermore, NR differs from LTE Advanced (LTE-A) in that it can only support a single SCS of 15 kHz and CA with up to 5 component carriers (CCs) resulting in a maximum aggregated bandwidth of 100 MHz, whereas NR is capable of aggregating up to (16 CCs) and offers a higher bandwidth. Table 2.4 summarizes the 5G NR supplementary frequency bands in FR1 and FR2, applied SCSs, and maximum bandwidth with and without CA [111]. In terms of data rate, frequency bands from 24.25 GHz to 52.6 GHz can provide data exchange at the rates of several Gbps [102, 110].

From the 3GPP standardization point of view, 5G NR has been developed under Release 15 and Release 16 defining operation for frequencies up to 52.6 GHz and all physical layer channels, signals, procedures, and protocols have

Table 2.4: 5G NR Supplementary Frequency Bands in FR1 & FR2 with Max. Bandwidth [54, 111].

Frequency Range	Band Index	Uplink (GHz)	Downlink (GHz)	Subcarrier Spacing (SCS)	Max. BW with and without Carrier Aggregation (CA)	Duplex Mode
FR1 (450 ~7125) MHz	n77	3.3 - 4.2	3.3 - 4.2	15 / 30 / 60 kHz	100 MHz per component carrier, 1.6 GHz with CA up to 16 component carriers	TDD
	n78	3.3 - 3.8	3.3 - 3.8			TDD
	n79	4.4 - 5	4.4 - 5			TDD
FR2 (24.25 - 52.6) GHz	n257	26.5 - 29.5	26.5 - 29.5	60 / 120 kHz	400 MHz per component carrier, 6.4 GHz with CA up to16 component carriers	TDD
	n258	24.5 - 27.5	24.5 - 27.5			TDD
	n260	37.0 - 40.0	37.0 - 40.0			TDD
	n261	27.5 - 28.35	27.5 - 28.35			TDD

been optimized for uses under 52.6 GHz [112]. However, in Release 17 [113], 3GPP has considered the maximum SCS up to 960 kHz for the frequency band between 52.6 GHz and 71 GHz. The reason for this is that the air interface for Release 15 and Release 16 has been optimized for a 240 kHz SCS under 52.6 GHz [112].

In particular, one of the main objectives of Release 16 (July 2020) is to extend the applicability of 5G NR to unlicensed spectrum in mmWave, NR-U [55, 114] as a general purpose technology that allows fair coexistence across different Radio Access Technology (RATs) [109]. NR-U differs from LTE-U and LAA which were standardized based on CA using 5 GHz bands, whereas the design of NR-U considers multiple bands 2.4 GHz (unlicensed worldwide), 3.5 GHz (shared in the USA), 5 GHz (unlicensed worldwide), 6 GHz (unlicensed in the USA and Europe), 37 GHz (shared in the USA) [55, 115], in addition to 60 GHz (unlicensed worldwide) [81, 113]. Furthermore, NR-U is expected to be extended to higher frequencies such as V and W mmWave bands (60 - 114.25) GHz in upcoming releases, including Release 18 or beyond. This expansion is noteworthy because it offers not only a very wide spectrum up to 15 GHz, but also new opportunities to facilitate many high-capacity use cases, such as back/fronthaul, relay, industrial IoT, private network, advanced vehicle-to-everything (V2X), and tightly coupled licensed-unlicensed spectrum usage [111].

2.4.1.4 Access to Licensed/Unlicensed Bands in NR-U mmWave

NR-U for sub 7 GHz and NR-U for mmWave bands (standardized in Release 16 and 17 respectively) support different deployments scenarios for coexistence with other licensed and unlicensed systems [55, 109]. The NR-U supports these modes for coexistence with other systems:

- NR-U Carrier Aggregation: NR-U CA is developed based on the approach of LTE-LAA which was first introduced in Release 13 [109], allows for the aggregation of NR-U in unlicensed frequency bands and NR in licensed frequency bands [55, 115]
- NR-U Dual Connectivity: NR-U DC is built upon LTE-enhanced LAA (eLAA), which was introduced in Release 14 [109], and enables for simultaneous connectivity with NR-U in unlicensed spectrum and either NR or LTE in the licensed spectrum [55].
- NR/UL, NR-U/DL: This scenario involves the combination of a licensed carrier that is serviced by a 5G NR cell for uplink communication, and an unlicensed carrier that is serviced by a 5G NR-U cell for downlink communication [55, 114].
- NR-U Standalone: In 3GPP Release 16, a new approach called Standalone NR-U was introduced, which allows for the operation in unlicensed spectrum without being anchored to any licensed carrier, similar to MulteFire approach proposed for LTE [109]. Whereas, Release 15,

only supports non-standalone (NSA) operation of 5G NR networks, where 4G LTE and 5G mobile networks coexist [116].

2.4.1.5 mmWave Spectrum Options for 6G

5G uses more spectrum than previous generations and this trend is expected to continue in 6G. One potential spectrum option for 6G is the mmWave band above 52.6 GHz, such as the W-band (75 – 110) GHz, which offers an abundance of available spectrum. Besides, 6G is expected to operate in the mmWave bands defined by the ITU-R and 3GPP for 5G. This broad spectrum in mmWave band provides an opportunity to cover capacity-intensive applications in 6G. However, the challenges related to path loss and expensive hardware costs restrict the use cases and deployment scenario in such higher frequencies. Despite the high propagation loss in bands above 52.6 GHz, relatively large coverage can still be achieved with LOS transmission and high gain antennas. This makes urban macro/rural macro scenarios suitable for the fixed wireless access and backhaul applications, which have LOS transmission conditions [97]. Overall, the mmWave bands offer a promising spectrum option for 6G, but more research and development are needed to overcome the challenges and realize the full potential of this frequency range.

2.4.1.6 Expected Use Cases of mmWave in 6G

With the advantages of mmWave mentioned above such as huge bandwidth and narrow beams, mmWave has potential applications that are expected to fulfill/realize the vision of 6G systems. The use cases of mmWave are categorized as;

- Wireless Backhaul: Wireless backhaul using mmWave frequencies is becoming an increasingly popular solution for connecting BSs in small cell dense deployment scenarios [102]. In particular, mmWave frequencies in the 60 GHz and E-band (71 – 76) GHz and (81 – 86) GHz provide a huge bandwidth, which can support very high data rates of several Gbps [106]. This makes them suitable to support the high-speed transmission between small cell BSs or between BSs and gateways [117]. Moreover, wireless backhaul solutions, such as microwave and mmWave, can offer several advantages compared to fiber-based backhaul in certain scenarios such as rural areas and mountains regions. In such cases, laying fiber in order to connect core network with small cells is not feasible due to high deployment costs and availability problem, or where it may be time-consuming [118]. Consequently, mmWave wireless backhaul can overcome these challenges and provide a cost-effective and scalable solution for small cell backhaul [102, 118]. As a result of these advantages, mmWave wireless backhaul is projected to have a significant role in the next generation of cellular systems, including beyond B5G and 6G.

- Vehicular Networks: The use of mmWave bands, especially those at 24 GHz and 77 GHz, can greatly benefit communication between vehicle-to-vehicle (V2V) and vehicle-to-infrastructure (V2I), in high-speed transportation systems, such as cars, high-speed railways, and subway systems. These systems require data rates of several Gbps, which are not possible with the 10 MHz channel bandwidths at 5.9 GHz used in current 4G technology [119]. However, the use of mmWave frequencies for vehicular networks also presents challenges related to beam alignment and routing stability due to the high mobility of vehicles, which requires further research and development to overcome [120].

- Wearable Devices: Wearable devices include smartwatches, smart wristbands, smart (AR, VR) glasses, motion trackers, and so on. Different types of wearable devices generate huge data traffic, which requires huge bandwidth to achieve low latency. Therefore, mmWave is a promising candidate for connecting these wearable devices [101, 121].

- Imaging and Tracking: The mmWave communications, operating at frequencies such as 60 GHz, are a promising option for imaging and tracking systems, as the signals in this band are mostly reflected from objects larger than their short wavelengths. Utilizing the high directional beams of 60 GHz links, dimensions of objects can be precisely measured, which reduces the interference and enhances the accuracy of tracking [102]-[101].

2.4.2 THz Band

While the path to higher carrier frequencies clearly supports much greater bandwidth, the total consecutive available bandwidth for mmWave systems remains below 10 GHz, making Tbps data rates difficult to achieve [100]. In this sense, the potential for achieving ultra-high speed data rates of up to 1 Tbps and supporting bandwidth-intensive applications has made THz band communication a promising enabler for 6G technology [122]. The THz band lies in the frequency range of 0.3 THz to 10 THz [25], between mmWave and the IR bands and shares some properties with both bands [122]. The THz band is also known as the sub-millimeter radiation due to its wavelengths beginning at 1 mm and progressing into shorter wavelengths [123]. The THz frequency range from 275 GHz to 300 GHz falls within the mmWave band, whereas the other part from 300 GHz to 3 THz falls within the far-IR spectrum band [89]. Despite being part of the optical band, the (300 GHz - 3 THz) band exhibits properties similar to the RF band (i.e, is characterized by electronic behavior). This behavior can be explained by the fact that THz radiation lies at the boundary between the RF and optical frequency bands, as shown in Figure 2.2 [89, 124].

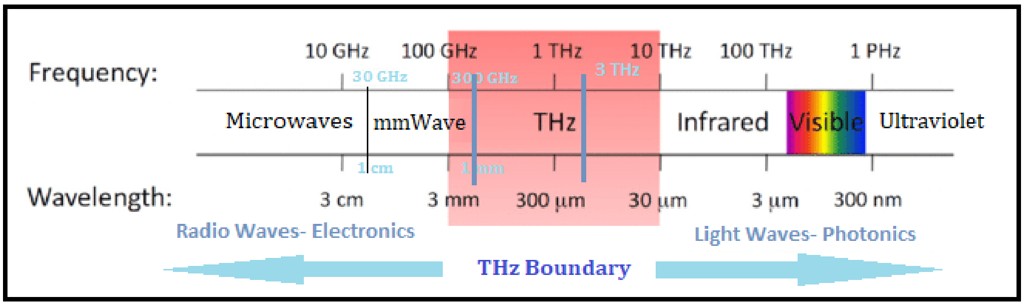

Figure 2.2: The THz band encompasses frequencies from 0.3 THz to 10 THz and occupies a position between the mmWave band and the infrared IR band. The waves in this band exhibit properties of both electronics and photonics.

For a considerable period of time, the lack of practical and small-scale techniques for producing and detecting THz signals hindered the practicability of using THz band communication [125]. Specifically, the inadequacy of semiconductor devices to efficiently convert electrical energy into electromagnetic energy at THz frequencies has long posed a challenge for THz communication [126]. However, in the last decade, the THz technology gap has been significantly reduced due to notable advancements in semiconductor technologies and the emergence of new materials, which offer greater potential for THz band communication [127].

2.4.2.1 Standardization of THz Communication

Standardization efforts for THz wireless communications began in 2008, when the IEEE formed an Interest Group on THz communications (IGTHz) under the IEEE 802.15 standard umbrella [128]. In 2014, the group members made key design choices and preliminary performance predictions, which laid the foundation for the IEEE Task Group on 100G Wireless (TG100G, IEEE 802.15.3d) [129]. In 2017, IEEE Std. 802.15.3d was issued as the first wireless communication standard in the 300 GHz band to support 100 Gbps and above wireless point-to-point links [130]. The development of IEEE Std. 802.15.3d- 2017 has been based on the 2016 version of the RRs. The RRs include an allocation of the bands from (252 - 275) GHz for the use by land mobile and fixed service on a co-primary basis [131]. At WRC- 2019, 160 GHz of the spectrum in the whole frequency band between 275 GHz and 450 GHz was opened for THz communications and the outcome of WRC-19 has included a new footnote to the RRs (No. FN5.564A), describing the conditions for the use of the spectrum between (275 – 450) GHz by land mobile and fixed service [129], and indicating potential standardization of the low frequency window of the terahertz band for near-future wireless communications [130]. In accordance with ITU-R recommendations, the frequency range from (275 GHz to 3 THz) has been identified as a major part of the THz communications [25, 124]. Since the frequency bands (275 GHz – 3 THz) have not been allocated to any services globally yet, adoption of these higher frequency bands is a potential solution to achieve the desired data rate at the Tbps level [25, 124]. The envisioned capacity for 6G can be achieved by aggregating the THz band (275 GHz – 3 THz) with the current mmWave band (30 – 300) GHz, as a result of which the overall band capacity will increase by approximately 11.11 times [25, 124].

2.4.2.2 THz Features and Limitations

With a multi-gigahertz bandwidth, the THz band is likely to be one of the candidate bands as a solution to the problem of spectrum scarcity and to improve the capacity of the next generation of wireless systems [127]. In general, THz-based communications are characterized by a wide frequency range, high speed, good directivity, high security, and better penetrability than infrared IR and visible light VL under bad weather conditions or noisy environments [132]. THz communications have the ability to support the much higher speed data rates from multi-Gbps to several Tbps than mmWave communications [128, 133]. Moreover, the shorter wavelength of THz when compared to mmWave makes it more directional and less prone to free-space diffraction [128]. Because THz band communication exhibits highly directional transmission, this can significantly mitigate intercell interference, dramatically reduce the probability that communications can be listened to, and provide better security [80]. Even though the increased directionality of THz transmissions presents a more challenging environment for eavesdroppers, there is still an opportunity for eavesdropper to intercept signals in LOS transmissions. Therefore, physical layer security techniques, that exploit the physical properties of wireless channels to incorporate security features, have been considered as an important solution for THz links [134]. Furthermore, THz has a good penetrating ability to dielectric materials, and it can be used to detect hidden objects [132].

However, there are many challenges facing the THz spectrum, including:

- Atmospheric/Absorption Loss: When operating at THz frequencies, the losses from path and reflection are joined by molecular absorption, which weakens the received power and amplifies noise. Molecular absorption produces additional noise, known as molecular absorption noise, in addition to the thermal noise found in lower frequency bands. Specifically, molecular absorption is caused by the energy differences between the molecular states of the physical medium during transmission [126]. Oxygen and water vapor in the atmosphere are the primary components responsible for absorption in the THz frequency [110].

- Beam Tracking, Beam Alignment, and Mobility Management: To combat the high transmission loss at THz frequencies, it is essential to employ large antenna arrays for directional beamforming. This technique utilizes extremely narrow pencil beams for LOS links, which can mitigate attenuation losses and provide natural interference mitigation, thereby extending the communication range of THz networks. However, pencil beams are highly sensitive to changes in user position and orientation, which can cause beam misalignment and affect the LoS link reliability. Consequently, they introduce new challenges related to mobility management, efficient beam tracking, and beam alignment. [126], [135].

- Engineering Challenges for Antennas and RF Circuitry: At higher frequencies such as THz, it becomes challenging to manufacture miniaturized chips that can effectively suppress noise and interference between components, while also overcoming the limitation of impedance. To address these challenges, ongoing research efforts are exploring techniques such as distance-aware physical layer design, supermass Multiple Input Multiple Output (MIMO) communication, smart surface, and graphene transistors [132].

- Power Consumption: The use of large antennas in THz systems presents a significant power consumption challenge, primarily due to the necessary analog-to-digital (A/D) conversion required in broadband THz systems. The power consumption increases exponentially with the sampling rate and the number of samples per bit, which is dependent on the required high-resolution quantization for the vast bandwidth and enormous antennas in the THz band. Consequently, developing low-power and cost-effective devices remains a crucial obstacle [136].

In addition, there are non-technical obstacles associated with policies and regulations for the allocation and usage of frequency spectrum in the THz range [136]. Overcoming all of these challenges is essential to effectively launch THz wireless communications in practice.

2.4.2.3 Use Cases of THz in 6G

THz communication has a broad range of potential applications at both macro and micro/nano scales. These applications can be grouped into various categories depending on the specific sector or scenario, including automotive, indoor networking, aerospace, healthcare, intrinsically safe environments, location-based services, defense, underwater communication, and more [128]. Below, some of the key applications of THz communications:

- Macroscale use cases: The primary use cases for THz communications at the macroscale are expected to be driven by emerging applications that require Tbps links, which are not possible using the mmWave spectrum. These applications include ultra-high-definition holographic (HD) video conferencing, three-dimensional (3D) gaming, XR, and haptic communications, among others [23]. In addition, THz communications show promise as a potential candidate for the next generation of data centers. With THz links, seamless connectivity at ultra-high speeds in fixed networks can be achieved, along with adaptability for hardware reconfiguration, whereas conventional data centers manage connectivity and maintain it using wired networks, resulting in high costs for both installation and reconfiguration of the system [20]. Furthermore, THz communications can play a vital role in wireless local area networks (WLANs) and wireless personal area networks (WPANs) applications by providing a means for seamless interconnection between ultra-high speed wired networks such as fiber optical links, and wireless devices such as laptops or tablets in WLANs, or between personal wireless devices in WPANs [102]. THz communications can also have potential applications in vehicular communication scenarios such as V2V and V2I. In these scenarios, neighboring or cooperating vehicles share perceptual data with each other using THz bands for high-rate and low-latency communication. The shared data can be used to create a satellite view of the surrounding traffic and real-time maps of the environment [128].

- Micro/nanoscale: Enabling communications between nano-machines is another potential application of the THz band. These nano-machines can carry out simple tasks, such as computations, data storage, actuation, and sensing. The transmission distance for such communications depends on the specific application and can range from a few micrometers to a few meters [23]. One of the most significant potential application of nano-machine enabled communications is the ability to transmit information within sub-mm sized regions inside the human body, which is typically inaccessible by any other medical device, making this technology particularly useful in the field of healthcare [137]. Enabling interactions between nano-machines, nano-sensors, and nano-actuators at the same scale as living systems and chipsets can lead to the development of the Internet of Nano-Things (IoNT) [126].

2.4.2.4 Vision of THz Communication in 6G

While THz systems have shown great promise for revolutionizing wireless networks, they are still in their nascent stage and require further research and development to fully realize the potential of THz systems and to overcome the technical challenges [126]. This means that it will likely take a long time to become mature and commercially available for use. Meanwhile, mmWave and OWC systems have already been extensively studied and commercially deployed in various applications, making them more likely to be the enabling technology for 6G wireless networks than THz systems. However, with the advancements in the infrastructure and computational aspects of communication systems, such as ultra-massive MIMO (UM-MIMO), intelligent surfaces, new signal processing methods and communication protocols, make it possible for THz communications to mature and become a viable technology for future wireless networks [138].

2.4.3 Optical Spectrum (VL, IR, UV)

Besides THz-based cellular communications, OWC systems are being explored as a means to provide broadband connectivity and coverage for 6G [122].

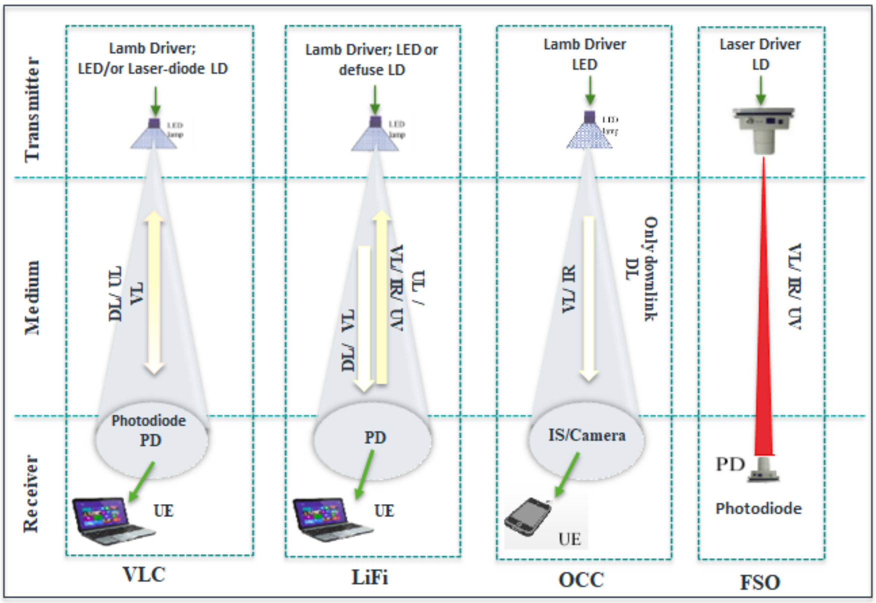

Figure 2.3: OWC technologies architectures. The figure shows the basic components of an OWC system, including a transmitter, a receiver, and an optical channel (VL- IR- UV) for different OWC technologies; VLC, LiFi, OCC, and FSO.

OWC systems operate in the IR, VL and UV frequency bands and are generally considered to be more mature than THz systems, with deployments in various applications [136]. OWC technologies include, Visible Light Communication (VLC), Light Fidelity (LiFi), Optical Camera Communication

(OCC), Free-Space Optics (FSO), and Light Detection and Ranging (LiDAR) [122, 139, 140]. Moreover, OWC can be considered as a complementary technology to existing RF-based wireless communication technologies [136]. Figure 2.3 illustrates brief architectures of these technologies.

Table 2.5: mmWave, THz, Optical Spectrum [25]

mmWave		**mmWave**	mmWave Range1	30 - 275 GHz	10 - 1.1 mm
	THz		mmWave Range 2	275 - 300 GHz	1.1 - 1 mm
Optical		**Infrared (IR)**	Far IR- Range 1	0.3 - 3 THz	1 - 0.1 mm
			Far IR- Range 2	3 - 20 THz	0.1 - 0.015 mm
			Thermal IR	20 - 100 THz	0.015 - 0.003 mm
			Short-wavelength IR	100 - 214.3 THz	3000000 - 1400 nm
			Near IR	214.3 - 394.7 THz	1400 - 760 nm
		Visible Light (VL)	Red	394.7 - 491.8 THz	760 - 610 nm
			Orange	491.8 - 507.6 THz	610 - 591 nm
			Yellow	507.6 - 526.3 THz	591 - 570 nm
			Green	526.3 - 600 THz	570 - 500 nm
			Blue	600 - 666.7 THz	500 - 450 nm
			Violet	666.7 - 833.3 THz	450 - 360 nm
		Ultraviolet (UV)	UVA	750 - 952.4 THz	400 - 315 nm
			UVB	952.4 - 1071 THz	315 - 280 nm
			UVC	1.071 - 3 PHz	280- 100 nm
			NUV	0.750 - 1 PHz	400 - 300 nm
			Middle UV	1 - 1.5 PHz	300 - 200 nm
			Far UV	1.5 - 2.459 PHz	200 - 122 nm
			Hydrogen Lyman-alpha	2.459 - 2.479 PHz	122 - 121 nm
			Extreme UV	2.479 - 30 PHz	121 - 10 nm
			Vacuum UV	1.5 - 30 PHz	200 - 10 nm

Table 2.5 shows the optical sub-bands for possible wireless 6G communications, THz and mmWave [25]. The optical regions encompass a range of wavelengths, including (750 nm - 1 mm) for IR, (380 nm – 750 nm) for VL, and (10 nm – 400 nm) for UV [141].

OWC technologies are expected to have wide-ranging applications, including V2X communication, indoor mobile robot positioning, VR, and underwater [25]. A variety of OWC technologies are being developed to address the requirements of future communication systems beyond 5G [142]. Generally, wireless optical technologies offer several advantages such as high data rates, low latency, secure communications, and reduced power consumption

[122]. The possibility of combining OWC and RF technologies, known as hybrid RF/OWC systems, could offer an efficient solution to meet the high user demands expected in the near future [143]. Hybrid RF/optical and optical/optical wireless systems, such as OWC/RF, FSO/RF, WiFi/LiFi, VLC/femtocell, VLC/FSO, and LiFi/OCC [142], offer a promising approach to overcome the limitations of individual systems while leveraging the advantages of each technology [144].

2.4.3.1 Visible Light Communication (VLC)

VLC is a wireless communication technology that utilizes visible light to transmit high-speed data wirelessly. It operates within a frequency range of (400 – 800) THz, which is not subject to licensing requirements [25, 138, 145]. The transmitter in VLC systems employs light-emitting diodes (LEDs) and intensity modulation (IM) technique to transmit data at high speeds [122]. On the receiver side, VLC typically uses photodiodes (PDs) or laser diodes (LDs), along with direct detection (DD) technology to detect the intensity (power) of the received optical signal [122]. DD employs photodiode to convert the incident optical signal power into a corresponding electrical current that is proportional to the signal power [146].

a) **Features and Limitations**: VLC technology provides various distinctive benefits compared to radio communication. Firstly, it can leverage multiple available spectra, providing a wider range of potential frequencies [136]. Secondly, external electromagnetic interference has minimal impacts on VLC-based communication [91]. Thirdly, the transmission medium used in VLC technology is visible light, which makes the network more secure, as the signal cannot penetrate walls and other obstacles. Fourthly, the spectrum occupied by VLC systems is free and unlicensed [138]. Additionally, VLC can be combined with RF systems to form a hybrid RF/VLC wireless communication, enabling highly energy-efficient communication and enhancing the user experience [122]. Although VLC technology has several advantages, it has limitations that must be addressed. For instance, it is not suitable for outdoor use and cannot support long-distance communication [142]. Moreover, there are several technical challenges that require further investigation, including channel modeling, fast switching mechanisms between optical and radio-frequency systems, development of new theoretical bounds for channel capacity, and improving physical layer security and coding techniques. Addressing these challenges is crucial for improving the overall performance and reliability of VLC technology [122].

b) **Standardization of VLC:** Optical wireless technologies are addressed by IEEE standards, including IEEE 802.15.7-2011 (VLC), IEEE 802.15.13 (Li-Fi), and IEEE.802.15.7m OCC [147]. However, it is worth noting that the standardization efforts of OWC systems, including VLC, is not limited to IEEE. Other large-scale organizations, such as the Visible Light Communication Consortium (VLCC) in Japan and the European OMEGA project, have also played a significant role in the standardization and development of VLC technology [139]. In 2003, Japan began the standardization of VLC systems, and interest in the technology has been increasing since then [148]. In 2007, the Japan Electronics and Information Technology Industries Association (JEITA) introduced two standards based on visible light communication [149], namely (CP-1221) and (CP-1222) respectively [149, 150]. JEITA CP-1221 standards emphasizes the fundamental design requirements of VLC systems, and JEITA CP-1222 provides details about visible light ID systems [150]. Following the introduction of JEITA CP-1222, a new standard named CP-1223, also known as the visible light beacon system standard, was proposed by the Japanese six years later [149, 151]. The development of VLC technology continued, and in September 2011, the IEEE established a standard for VLC systems, named IEEE 802.15.7, which includes the physical and medium access control (MAC) layers [152]. This standard encompasses three physical (PHY) types for VLC: PHY, I which operates from (11.67 to 266.6) kbps, PHY II, which operates from (1.25 to 96) Mbps, and PHY III, which operates between (12 and 96) Mbps for indoor and outdoor applications [153]. The two modulation schemes supported by PHY I and PHY II are on-off keying (OOK) and variable pulse-position modulation (VPPM), both of which utilize a single light source. On the other hand, PHY III employs multiple light sources of different colors to implement color shift keying modulation (CSK) [154]. The standard also covers topics related to link mobility, the impairments caused by noise, and the interference from other light sources [152]. The IEEE 802.15.7-2018 standard, which was revised in 2018, provides additional information on various aspects of VLC technology. These include security, compatibility of VLC infrastructure with existing illumination infrastructure, selection of modulation schemes, and addressing dimming and flickering issues of light sources, among others [150].

c) **Expected Use Cases in 6G:** VLC technology is expected to have significant use cases in 6G, given its numerous benefits. VLC can be applied in various IoT applications, including smart homes, smart cities, smart transportation, smart buildings, smart grids, smart factories, and hospitals [122, 138, 142]. Because VLC is considered safe for all electronic equipment, which makes it suitable for use in RF restricted areas such as airplanes, chemical plants or hospitals [152]. Furthermore, VLC has the potential to be use in outdoor environments, such as V2V and V2I communications, to provide crucial information about road conditions, accidents, and traffic-off loading [122]. However, outdoor VLC deployment faces challenges such as interference from natural and artificial light sources, the rapid decrease of light intensity with distance, and the need to support high-mobility scenarios [122]. In comparison to RF, VLC can also transmit data underwater communication over longer distances since RF electromagnetic waves are highly absorbed in water [122, 142].

2.4.3.2 Light Fidelity (LiFi)

LiFi is a wireless communication technology that operates using the IR and VL spectrum to transmit data at high speeds [155]. It is often seen as an extension of VLC technology. Although LiFi and VLC share some similarities, such as using light as a medium for communication, they have some distinct differences. Firstly, LiFi is a bidirectional communication system that utilizes transceivers at both ends of the connection, whereas VLC systems can be either unidirectional or bidirectional [144]. Secondly, LiFi must support multiuser communications, specifically point-to-multipoint and multipoint-to-point communications, whereas VLC systems can support point-to-point, point-to-multipoint, and multipoint-to-point communications [142]. Thirdly, LiFi uses VL for the forward link and VL or IR for the reverse link, whereas VLC uses VL as the communication medium [144]. Additionally, LiFi is capable of supporting user mobility and handover [122]. To be considered as LiFi, a VLC system must possess LiFi features such as multi-user connectivity, point-to-multipoint and multipoint-to-point communications, and seamless user mobility. Conversely, a LiFi system can only be classified as VLC when VL is utilized as the transmission medium [140]. Like VLC, LiFi communication systems use LEDs and photodetectors as transmitters and receivers, respectively [102]. However, it is also possible to use LDs integrated with an optical diffuser as transmitters and light sources [142]. Moreover, LiFi is envisioned as complementary technology to WiFi [102].

a) **Features and Limitations:** LiFi has the potential to be a cost-effective solution as it can easily integrate with the current RF wireless networks, allowing for the creation of heterogeneous wireless networks that combine optical and RF fields [122]. In comparison to WiFi, LiFi offers several advantages, such as extremely high data rates, lower cost, easily available spectrum capacity, and superior security [142]. These features and advantages make LiFi a promising technology for the development of future 6G networks [122]. However, LiFi systems have limitations in outdoor applications due to interference from natural and artificial light sources and cannot provide long-range communication [122, 142]. In addition, technical challenges such as channel modeling and feasible interference mitigation techniques need further research [122].

b) **Standardization of LiFi:** After the publication of the first two VLC standards JEITA CP-1221 and JEITA CP-1222 by JEITA in 2007, and the IEEE 802.15.7 standard in 2011, the IEEE 802.15 working group continued its efforts to standardize VLC technology. In 2015, IEEE established the 802.15.7r1 Task Group (TG) to revise the IEEE 802.15.7 standard. The goal of 802.15.7r1, later referred to as 802.15.m, was to expand the standard to cover not only visible light but also near-UV and IR wavelengths, and to include options such as OCC and LiFi [156]. Task Group 13 (TG13) was launched by the 802.15 Working Group in March 2017 with the aim of developing an OWC standard (802.15.13) that can support point-to-point and point-to-multipoint configurations with data rates up to 10 Gbps over a range of 200 m. This standard is designed to operate over a range of wavelengths from 10,000 nm to 190 nm [157]. One drawback of 802.15.13 is that it is intended for industrial use and is not targeted towards mass market consumers, meaning it is unlikely to be integrated into widespread wireless network systems. Additionally, 802.15.13 is limited to LOS scenarios [158]. A task group named IEEE 802.11 Light Communications Amendment - Task Group "bb" (TGbb) was formed alongside TG13, with the aim of integrating LiFi technology into the IEEE 802.11 ecosystem [159]. IEEE 802.11bb aims to create a distinct ecosystem for chipset vendors, network infrastructure, device integrators, and operators of IEEE 802.11, utilizing high-layer specifications. This will enable LiFi to coexist and cooperate with other WiFi standards and leverage the well-established commercialization phases of IEEE 802.11 for mass-market adoption [160]. Additionally, the ITU launched the G.vlc project in 2018 to create a system architecture and define the PHY/Data Link Layer functionality of LiFi transceivers for high-speed indoor networking applications. As a result, a new set of PHY recommendations known as G.9991 was published in 2019. G.vlc is currently the only LiFi standard that has available chipsets [157].

2.4.3.3 Optical Camera Communication (OCC)

OCC is an OWC technology that is currently receiving significant attention due to the recent advancements in camera technology and the widespread use of smart devices equipped with LED flashlights [161]. OCC is considered as promising technology for indoor positioning and navigation applications [102]. In comparison to VLC, OCC has a wider spectral range, as it can use both VL and IR as a communication medium [141]. In an OCC system, the receiver is typically equipped with built-in cameras or image sensors (IS), while the transmitter is a conventional commercial LEDs [102, 142, 144].

a) **Features and Limitations:** OCC offers several advantages over other OWC technologies. Firstly, OCC can be easily integrated or implemented with existing smart infrastructure such as smartphone and laptop cameras [122], rear vehicle cameras, and security cameras [147], allowing for ubiquitous coverage in both indoor and outdoor scenarios [122]. Secondly, OCC uses non-interference communication, which means that when using image sensors as a receiver, lights from different sources are almost perfectly separated on a focal plane due to the large number of pixels in image sensor [142]. As a result, OCC can mitigate interference caused by light coming from different sources and directions. This is made possible by advanced lenses used in portable cameras that can display lights from different sources and separate different signals, which can then be sampled using different pixels [122]. Lastly, One more advantage of OCC is its ability to provide interference-free communication and a high signal-to-noise ratio (SNR), even in outdoor environments [142]. Despite its advantages, OCC has some limitations. For instance, the data rate is relatively low due to the limited sampling rate at the receiver, and random blockages can occur [147]. Moreover, the OCC system faces synchronization challenges related to the limited pulse rates of LEDs within the camera's frame [122]. Additionally, since the optical channel is LOS, any object that obstructs light penetration [122], such as walls, buildings, thick fog, or gas, can block the OCC communication links [142].

b) **Standardization of OCC** The development of camera-based optical communication was greatly stimulated by the release of the IEEE 802.15.7:2011 standard for short-range VLC. This led to the formation of a task group (TG7m) in 2014 to revise the standard, known as the IEEE 802.15.7m standard, specifically for camera-based optical communication [162]. TG7m has been working on specifying the technical requirements of OCC, including the OCC transceivers, system architecture, and PHY and MAC layers [147].

c) **Expected Use Cases in 6G:** Based on the advantages of OCC, it is expected to have a wide range of applications in 6G, including V2X communication, AR/VR, drone-to-drone communication [122], and digital signage [142]. Another potential use case for OCC in 6G is in localisation (positioning) for indoor environments such as shopping centers and large supermarkets [122].

2.4.3.4 Free Space Optics Communication (FSO)

FSO is a wireless communication system that has gained significant interest and development in recent years [163]. FSO technology uses various segments of the electromagnetic spectrum, including near- infrared (NIR), VL, and UV bands, to serve as the communication medium [122, 142]. FSO systems commonly use LDs to transmit data at high data rates [161]. However, some manufacturers employ high power LEDs with beam collimators [164]. The LD transmitter generates a highly focused and coherent laser beam that enables long-distance data transmission [144], allowing for the establishment of high-data-rate communication links between a transmitter and a receiver [142]. FSO technology provides benefits such as high bandwidth and long transmission distances at high data rates [161]. These features make it suitable for high-speed and high bandwidth applications such as wireless backhaul broadband connectivity. Moreover, it is also considered as a promising solution to meet the massive traffic demands of 6G systems [122]. FSO links offer a significantly higher optical bandwidth compared to RF links, which allows for much higher data rates [164]. Furthermore, FSO can be integrated with existing RF wireless networks to create heterogeneous networks that combine both optical and RF domains, resulting in enhanced capacity and coverage [122]. This integration can be achieved through hybrid FSO, Radio over FSO (RoFSO), and MIMO FSO, which can support the ultra-high-speed demands of 5G/B5G by overcoming the limitations of single technologies [143].

a) **Features and Limitations:** FSO technology offers several key benefits over other connectivity and backhaul technologies. It is easy to deploy and provides high bit rates with low bit error rates. FSO also enables full duplex transmission, allows independent protocol, and does not require a license [165]. Additionally, FSO systems offer several other advantages, such as the ability to use high-frequency reuse factors, secure communication, immunity against electromagnetic interference, and reduced power consumption [122]. FSO communications have the potential for high-speed data transmission, but their effectiveness can be limited by various factors that negatively impact performance, including absorption, scattering, and turbulence within the atmospheric channel [166–168]. Of all the challenges faced by FSO communications, atmospheric turbulence is the most significant challenge faced by FSO communication as it can cause severe degradation in the bit error rate performance of the system, making the communication link unfeasible [166]. The amplitude and phase of the FSO signal can experience random fluctuations due to atmospheric turbulence, which is called channel fading. Such fluctuations can cause a decrease in signal quality, an increase in errors, and a reduction in link reliability [161]. Adverse outdoor weather conditions, such as heavy rain, fog, smoke, storms, deep clouds, and snow, can significantly degrade the performance of FSO links, leading to unreliable and unpredictable communication [122, 169]. FSO communications can also be affected by misalignment and geometric losses, which can lead to reduced signal power and degraded communication [170]. Misalignment losses may occur due to building sway or other factors that cause inadequate alignment between the transceivers [167]. On the other hand, geometric losses occur as a result of the light energy being spreading over a larger area as it travels through the atmosphere, which leads to a decrease in the power received by the receiver [168]. Therefore, it is important to address and mitigate these factors to ensure the efficient and reliable performance of FSO communication systems.

b) **Standardization of FSO:** In light of the potential deployment of FSO in mobile networks, there is a growing demand for simple and widely accepted channel models. However, standardization efforts in the context of FSO have been limited [171]. The Infrared Data Association (IrDA) group has developed a series of standards specifically for high-speed data transmission and short-distances FSO links [172]. These standards are targeted to connect handheld mobile devices with fixed stations or other mobile devices using short-range (typically from centimetres to less than 1 m), low-cost, line-of-sight, point-to-point FSO links [173]. More specifically, IrDA has defined six standards for the IR physical layer, including Serial Infrared (SIR), with data rates ranging from (2.4 to 115.2) kbps, Medium Infrared (MIR) with data rates ranging from (0.576 to 1.152) Mbps, Fast Infrared (FIR) supporting 4 Mbps, Very Fast Infrared (VFIR) supporting 16 Mbps, Ultra Fast Infrared (UFIR) supporting 96 Mbps, and Gigabit Infrared (Giga-IR) supporting 512 Mbps and 1.024 Gbps [174, 175]. In contrast, JEITA CP-1221, CP-1222, CP-1223, IEEE 802.15.7, and IEEE 802.15.7r1, are designed for short-to-medium range VLC that support low-data rate links [172]. In particular, the technical specifications established by IrDA, IEEE (802.11 and 802.15.7), and JEITA are primarily intended to cater for OWC links that are deployed indoors, whereas, the ITU is mainly concerned with developing standards and guidelines for terrestrial OWC links [171]. This includes propagation prediction techniques for designing terrestrial FSO links that operate in VL and IR regions of the spectrum (ITU-R P.1814-0 and ITU-R P.1817-1) [171]. Furthermore, the ITU is also involved in developing guidelines for planning fixed-service terrestrial FSO links [172]. However, the ITU-R P.1817-1 (2012) guidelines, which are entitled "Propagation data required for the design of terrestrial free-space optical links", provide only general recommendations and has not been updated recently [171].

c) **Expected Use Cases in 6G:** FSO systems have a various applications including backhaul for cellular networks, last mile access, and disaster recovery [142, 143, 166]. It also finds its applications in video surveillance, broadcasting, and underwater communication [122, 142, 143]. FSO systems has a wide range of applications across various networks, including aerial, optical, and terrestrial, and has been employed in applications such as ground-to-satellite, satellite-to-ground, satellite-to-airplane, airplane-to-airplane, satellite-to-satellite, satellite-to-UAVs, satellite-to-balloons, and satellite-to-ship connectivity [122, 142, 143]. FSO systems also have potential applications in inter-chip connectivity, as well as providing connectivity between different types of networks, such as MAN-to-MAN, LAN-to-LAN , ship-to-ship communication [142].

In Table 2.6, a comparison is made between mmWave, THz, and optical spectrum in terms of their frequency ranges, available bandwidths, features, limitations, regulations, and areas of application in the context of 6G technology.

Table 2.6: Comparison of mmWave, THz, and Optical Spectrum in terms of Frequency Ranges, Features, Limitations, and Application Areas [89, 100, 142, 176].

Issue	mmWave	THz	Optical Bands
Frequency Range	30 - 300 GHz	300 GHz - 10 THz	IR 3 - 430 THz VL 430 - 790 THz UV 790 THz - 30 PHz
Wavelength	10 - 1 mm	3 mm - 0.03 mm	IR 0.03 mm - 690 nm VL 690 nm - 380 nm UV 380 nm - 10 nm
Bandwidth	MHz to several GHz	10 GHz- 100 GHz	MHz to several GHz
Spectrum Regulatory	Licensed	Licensed	Unlicensed
Advantages	Wide bandwidth Small element size Narrow directional beam	Extremely wide bandwidth; enable communication rate exceeding Tb/s Suitable for Mssive-MIMO	Wide available spectrum High Security
Limitations	High free-space path loss Atmosheric gaseous absorption Blockage & Technical Challenges; Design circuit components and antennas	Path loss Atmosheric gaseous absorption Strong atmosheric attenuation Blockage & Technical\Engineering Challenges; Design circuit components and antennas	Small coverage area Mobility support is no guaranteed Performance is affected by environment conditions Very limited NLOS communications.
Applications Area in 6G	Wireless backhual, Wearable devices, AR/VR Imaging & Tracking	Holographic Teleportation, Digital Twin, Connected Robotics & Autonomous systems (CRAS); (include autonomous driving, atounomous drone swarms, Vehicle platoons), XR services, Industry 4.0, NTNs.	Smart buildings, smart factories, smart transportation, and hospitals, V2V, V2I communications, Backhaul for cellular networks, Remote sensing and track position and movements underwater communication

2.5 Concluding Remarks

Our study highlights the spectrum options for 6G, the importance of addressing technical challenges, promoting technology development, embracing spectrum sharing, and adapting policies and regulations. The key findings can be summarized as follows:

- Spectrum Options: Higher frequency bands such as mmWave, THz, and optical wireless (OW) spectra offer potential spectrum options for 6G, enabling faster data rates and higher capacity. However, challenges related to path loss and hardware costs need to be addressed for effective adoption.

- Technology Development: While THz systems hold promise, further research and development are required. More mature technologies like mmWave and OWC (e.g., VLC and FSO) are likely to play a significant role in enabling 6G networks.

- Spectrum Management Paradigm Shift: The deployment of 6G will require a paradigm shift in spectrum management. Spectrum sharing will become increasingly crucial to efficiently utilize limited resources in the context of higher frequency bands and localized service areas.

- Policy Implications: Policymakers and regulators must reevaluate current spectrum management policies to align with the unique requirements of 6G. Developing new spectrum assignment models that accommodate flexible deployment and define access rights will be essential.

These findings provide valuable insights for the successful deployment and utilization of 6G networks.

Chapter 3

Beam Alignment Error Modeling and Coverage Analysis in mmWave Networks

3.1 Introduction

The highly directional nature of mmWave communications requires the implementation of directional beamforming at both the transmitter and the receiver to establish a robust link. Determining the optimal beamforming directions between the transmitter and receiver is known as beam alignment [177]. In mmWave systems, achieving precise beam alignment is challenging due to multiple sources of error. These include imperfections in the antenna and beamforming techniques (e.g., analog beamforming distortions, array perturbations, and angle-of-departure (AoD) estimation inaccuracies), as well as mobility and environmental factors [178, 179].

Most prior studies in mmWave communications assume perfect beam alignment [10–12]. Nevertheless, several works have investigated the impact of beam alignment errors [13–15, 17, 19]. In studies such as [13–16, 18], alignment errors were commonly modeled using a zero-mean truncated Gaussian distribution with fixed angular boundaries and with either an arbitrarily chosen standard deviation or one derived from CRLB. For example, in [13], the standard deviation of the alignment error is typically chosen based on the assumed absolute error values, without being explicitly linked to the underlying physical parameters of the system. CRLB-based models, including [15] and its extension in [18], address this limitation by deriving the error variance from the CRLB of angle-of-arrival (AoA) estimates and explicitly relating error statistics to the physical parameters of the link, such as path loss, antenna array size, and the SNR of pilot signals. While CRLB-based models offer useful insights into specific misalignment scenarios, they are constrained by particular assumptions and estimation methods, limiting their flexibility to represent diverse alignment uncertainty conditions encountered in practical deployments. This uncertainty arises from various operational and physical factors, such as pilot overhead, feedback quantization, antenna imperfections, and user mobility. As a result, their generality and applicability across diverse scenarios are limited. Furthermore, these models lack explicit separation between alignment errors caused by hardware impairments and those due to informational uncertainty, making it difficult to analyze their individual impacts on system performance.

Motivated by these limitations, this chapter develops a unified probabilistic beam alignment error model with dynamic, information-aware boundaries. The model introduces a novel alignment information parameter that jointly controls the variance and truncation boundaries of the error distribution. This parameter abstractly captures the overall quality of the directional information available to the system, enabling a unified representation of the full spectrum of beam alignment scenarios, from a uniform distribution (no directional knowledge) to a truncated Gaussian (partial knowledge) and to a distribution approaching a Dirac delta function (near-perfect knowledge). The model also incorporates a hardware inefficiency factor, which accounts for antenna-system imperfections and, together with the alignment information parameter, controls the error variance.

The main contributions of this chapter are summarized as follows:

- **Information-dependent beam alignment error modeling:** Development of a probabilistic beam alignment error model using a zero-mean truncated Gaussian distribution, with variance and truncation boundaries jointly governed by an alignment information parameter, enabling a unified representation of all alignment regimes.

- **Antenna System Inefficiency Factor:** Introduction of a tunable factor that captures antenna hardware-related imperfections (e.g., phase noise, beam pattern distortion, and mutual coupling) which, together with the alignment information parameter, determines the alignment error variance.

- **Validation of Fading Assumptions:** Monte Carlo simulations comparing Rayleigh, Rician, Nakagami, and non-fading models under both LOS and NLOS conditions, confirming that Rayleigh fading serves as a mathematically tractable lower bound for coverage probability analysis.

- **Coverage Probability Analysis with Beam Alignment Error:** Derivation of analytical expressions for downlink coverage probability using stochastic geometry, incorporating the proposed alignment error model and validated through Monte Carlo simulations.

The remainder of this chapter is organized as follows. Section 3.2 presents the system model, including the network model, association model, link state and channel models, beam alignment error, and antenna model. Section 3.3

provides coverage probability analysis. Section 3.4 describes the simulation setup and discusses the results. Section 3.5 concludes the chapter.

3.2 System Models

This section describes the system components and assumptions used to evaluate downlink coverage probability. The model considers a typical user equipped with an omni-antenna and a serving BS with a directional antenna, as illustrated in Figure 3.1 (system model). The system model includes the network model, link state, channel model, association model, beam alignment error model, and the antenna model.

3.2.1 Network Model

All BSs are distributed according to a homogeneous Poisson point process (PPP), denoted by Φ, with a density parameter designated as (λ_b), across a two-dimensional space represented by the Euclidean plane $\mathbb{R}^2$ [180, 181]. Following Slivnyak's theorem and common practice in stochastic geometric analysis, we assume a typical user is situated at the origin. Subsequently, the analysis is conducted with a specific focus on this typical user [18].

3.2.2 Association Model

In cellular network analysis using point processes models, a critical consideration is the contact distance between a user and its nearest serving BS, as the statistical properties of this distance significantly affect signal strength and signal-to-interference-plus-noise ratio (SINR) [182]. In line with common

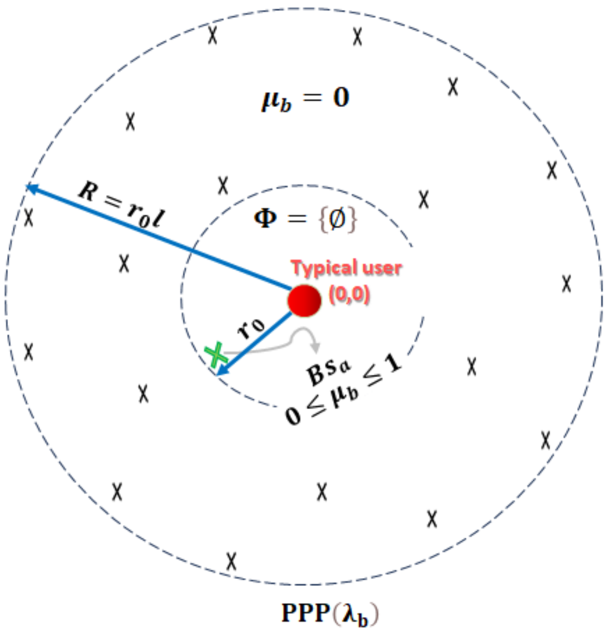

Figure 3.1: Stochastic geometry-based system model illustrating the typical user situated at the origin $(0, 0)$. The distance r_o denotes the proximity of the nearest BS, referred to as BS_a, to the typical user. BS_a is characterized by an alignment information parameter μ_b, where $0 \le \mu_b \le 1$. The ring-like region, extending from the boundary of the inner circle with radius r_o to the boundary of the outer circle with radius R, represents the area of interfering BSs. Here, $R = r_o\, l$, where $l > 1$ is a positive integer scaling factor. These interfering BSs have no beam alignment information, denoted by $\mu_b = 0$.

practices in cellular network analysis, we assume that the typical user is associated with the nearest BS, which is typically in LOS conditions particularly in mmWave scenarios like this, as described in [12]. This approach simplifies the characterization of signal strength and interference while providing a tractable framework to derive key performance metrics in cellular networks.

As illustrated in Figure 3.1, the typical user is positioned at the origin, with the distance to its serving BS defined as the contact distance r_o. No other BS is assumed to be closer to the typical user than this nearest BS ($\Phi = \{\phi\}$); all other BSs in the network located at distances greater than r_o are considered interfering BSs for this user. This assumption is consistent with established models in the literature [180, 183]. The contact distance r_o between the typical user and its nearest BS is modeled as a random variable. In a two-dimensional (2D) Poisson process, r_o follows a Rayleigh distribution with probability density function (PDF) given by:

$$f_r(r_o) = 2\pi\lambda\, r_o e^{-\lambda\pi r_o^2}, \tag{3.1}$$

where λ is the intensity of the Poisson process [180].

3.2.3 Link State and Channel Models

Signals operating within the mmWave bands are particularly sensitive to blockage effects during propagation, distinguishing them from signals in the lower frequency bands. These obstructions lead to notable differences in path loss characteristics between LOS and NLOS [11, 13, 19]. At a given propagation distance r, the path loss for a LOS mmWave link follows the model $l_L(r) = C_L r^{-\alpha_L}$, whereas in the NLOS scenario, the path loss is represented by $l_N(r) = C_N r^{-\alpha_N}$. The parameters α_L and α_N denote the path loss exponent for LOS and NLOS conditions, respectively, while C_L and C_N represent the intercepts for the LOS and NLOS links. In the close-in (CI) reference distance model, these intercepts correspond to the path loss at the reference distance (typically 1m) and are determined by the carrier frequency, whereas in the floating-intercept model, C_L and C_N are treated as curve-fitting parameters obtained from measurements [184]. Typically, it is observed that $\alpha_N > \alpha_L > 0$, and $C_L \geq C_N$ [185].

The model does not explicitly adopt detailed blockage models such as the LOS ball [9, 11, 18] or the 3GPP blockage model [185]. Instead, it focuses on two scenarios: a no-blockage case, where all links are assumed to be LOS, and a full-blockage case, where all links are NLOS. This enables the derivation of exact closed-form expressions for downlink coverage probability under pure LOS or NLOS assumptions. These scenarios provide fundamental performance benchmarks critical to understanding the behavior of mmWave systems, corresponding to deployment environments ranging from open areas with minimal blockage to dense urban environments with severe obstruction.

In the no-blockage scenario, a typical receiver is served by a LOS transmitter and experiences interference only from other LOS BSs. In the full-blockage scenario, all links are NLOS, including both serving and interfering BSs. The assumption of homogeneous link types (i.e., all links being LOS or all being NLOS) is consistent with the modeling approaches in [12, 13]. For example, in [12], although a LOS ball blockage model is adopted, the analysis primarily focuses on LOS links, while interference from NLOS links is shown to have negligible impact on SINR through numerical validation. In [13], a probabilistic blockage model is adopted, with analytical results derived for the special regimes of all-LOS or all-NLOS links, and numerical methods used to study networks with mixed LOS/NLOS links.

Shadowing is not explicitly included in the analytical model due to tractability limitations. Incorporating log-normal shadowing leads to mathematical intractability and prevents closed-form expressions in stochastic geometry-based analysis [186]. In mmWave networks, large-scale channel variations are dominated by blockage effects, and shadowing does not accurately capture blocking in dense networks because blockage not only introduces randomness in the average path loss but can also significantly change the effective path loss exponent [184]. Measurements further show that LOS and NLOS links exhibit fundamentally different path loss exponents, with NLOS links characterized by higher fitted values $\alpha > 2$ that reflect environment-dependent propagation effects associated with scattering and blockage [11]. Numerical results in [187] show that including log-normal shadowing does not significantly change the observed rate coverage trends.

For small-scale fading, Rayleigh fading is adopted in theoretical analysis, as commonly found in the literature [16, 187–189]. Although Rayleigh fading does not fully capture the sparse scattering characteristics of mmWave propagation, especially under directional beamforming [13], it provides a mathematically tractable framework for analysis [19]. As discussed in [187], more general fading models such as Nakagami do not provide significant additional design insights while substantially increasing analytical complexity. The simulation results, presented in Section 3.4, are in line with this observation.

3.2.4 Beam Alignment Error Model

Beam alignment is a critical aspect of mmWave systems due to the highly directional nature of signal transmission. Misalignment can significantly impact system performance and arises from various factors, including antenna hardware imperfections (e.g., array perturbations and mutual coupling), beamforming limitations (e.g., analog beamforming impairments and AoD estimation errors), and mobility-induced challenges [9]. Previous works, such as [13, 18], modeled beam alignment errors using truncated Gaussian distributions with zero mean and fixed boundaries. In Cheng et al. [13], the alignment error is modeled using a truncated Gaussian distribution with fixed boundaries of $\pm\pi$, which represent the angular limits of the BS sector. The absolute error is shown to increase monotonically with the standard deviation (σ) of the Gaussian distribution. However, the model does not clarify how σ is determined. Similarly, Zia et al. [18] adopt a truncated Gaussian model with boundaries $\pm\pi/3$, where alignment errors arise from deviations between the true AoA and the estimated AoA. Unlike Cheng et al. [13], Zia et al. [18] express σ as a function of the received SNR and system parameters, such as antenna configuration and channel characteristics.

The errors are modeled as a truncated Gaussian distribution with zero mean and dynamic boundaries, expressed as $\epsilon \sim \mathcal{N}_T\left(0, \frac{\zeta}{\mu}, -b(\mu), b(\mu)\right)$. This model introduces dynamic boundaries $b(\mu)$ that adjust according to the level of alignment information μ, where $\mu \in [0, 1]$. In this context, $\mu = 1$ represents perfect alignment knowledge, indicating that the system has complete and accurate information about the optimal beam direction. In contrast, when $\mu = 0$ corresponds to a scenario where no alignment information is available.

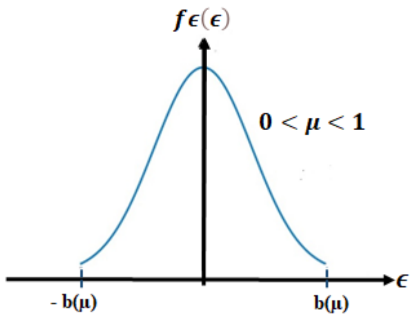

(a) PDF of error for $0 < \mu < 1$.

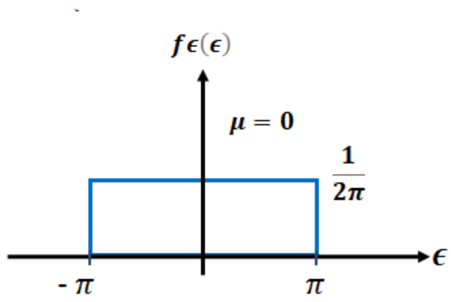

(b) PDF of error when $\mu = 0$.

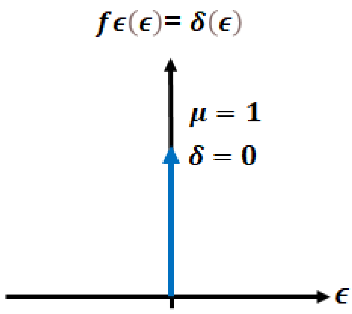

(c) PDF of error for an ideal system with $\mu = 1$.

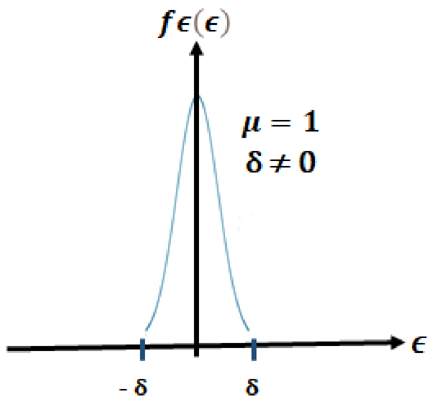

(d) PDF of error for a practical system with $\mu = 1$.

Figure 3.2: PDF of beam alignment error: (a) Truncated Gaussian distribution with dynamic boundaries for partial alignment information ($0 < \mu < 1$); (b) Uniform distribution for the case of no alignment information ($\mu = 0$); (c) PDF of error for an ideal system with perfect alignment at $\mu = 1$, which approaches a Dirac delta function $\delta(\epsilon)$; (d) Practical system error distribution with perfect alignment ($\mu = 1$).

For $0 < \mu < 1$, the system operates with partial alignment knowledge. The dynamic nature of the boundaries captures the varying degrees of alignment knowledge that are encountered in practical scenarios, providing a more realistic representation of beam alignment errors compared to traditional models that rely on fixed-boundary for the error distribution. While μ is introduced as an abstract modeling parameter, it can be related to measurable system quantities that reflect the accuracy of directional knowledge. For example, higher pilot SNR, denser pilot patterns, larger training beam counts, or more accurate user location estimates improve the system's directional information and correspond to higher values of μ. Conversely, low SNR, sparse pilot density, or rapidly changing user mobility reduce the reliability of directional information, resulting in smaller μ. Thus, although μ serves as an abstraction in the model, it remains grounded in measurable physical quantities and system-level procedures. Moreover, our model incorporates the inefficiency factor ζ, which accounts for inherent imperfections in antenna systems. By quantifying these inefficiencies, ζ serves as a tunable parameter that adjusts the spread of the error distribution based on the level of system imperfection, thereby enhancing the model's applicability to diverse system configurations and environments. In practice, ζ could be calibrated from measurements (e.g., beam patterns, received power, or alignment errors) or from detailed hardware simulations to reflect the actual performance of a given antenna system.

The PDF of the error is given by:

$$f_\epsilon(\epsilon) = \begin{cases} \frac{\mu e^{-\frac{\mu^2 \epsilon^2}{2\zeta^2}}}{\sqrt{2\pi}\zeta \operatorname{erf}\left(\frac{\mu\, b(\mu)}{\sqrt{2}\,\zeta}\right)}, & \text{if } -b(\mu) \le \epsilon \le b(\mu), \\ 0, & \text{otherwise.} \end{cases} \tag{3.2}$$

Here, $\operatorname{erf}(\cdot)$ denotes the error function, defined as $\operatorname{erf}(x) = \frac{2}{\sqrt{\pi}} \int_0^x e^{-t^2} dt$.

The PDF satisfies the normalization condition:

$$\int_{-b(\mu)}^{b(\mu)} f_\epsilon(\epsilon) = 1 \quad \text{(normalization conditions).} \tag{3.3}$$

To model the dynamic nature of the boundary $b(\mu)$ in relation to the availability of beam alignment information, we propose a linear relationship between them, formulated as follows:

$$b\left(\mu\right) = \pi - \mu\left(\pi - \delta\right), \tag{3.4}$$

In (3.4), δ is the minimum truncation boundary, representing the residual misalignment that persists even under the perfect alignment information. This error is unavoidable by design and arises from intrinsic system-level limitations of practical beamforming, such as finite beam resolution and discrete codebooks. For practical mmWave systems, $\delta > 0$; for an ideal system, $\delta = 0$, resulting in $b(\mu) = \pi - \mu\pi$. The linear relationship in (3.4) is adopted for analytical tractability and reflects the intuitive trend that higher alignment information (larger μ) reduces the uncertainty range $b(\mu)$. Although a nonlinear mapping could capture more complex practical behaviors, it is not considered in this work and is deferred to future research.

The behavior of the alignment error PDF, $f_\epsilon(\epsilon)$, is governed by μ, as demonstrated by the following limits:

$$\lim_{\mu \to 0} f_\epsilon(\epsilon) = \frac{1}{2b(0)}, \quad \text{(uniform distribution)} \tag{3.5a}$$

$$\lim_{\mu \to 1} f_\epsilon(\epsilon) = \delta(\epsilon), \quad \text{(Dirac delta function)} \tag{3.5b}$$

Figure 3.2 provides a comprehensive view of how the alignment error distributions evolve with the availability of alignment information and highlights the transition from a uniform distribution to a more accurate alignment model as the information parameter μ increases. For partial availability of alignment information ($0 < \mu < 1$), the alignment error distribution follows a truncated Gaussian, as shown in Figure 3.2 (a). The boundary $b(\mu)$ is dynamically adjusted based on the alignment information available, and as μ increases, the distribution becomes narrower, indicating improved alignment accuracy. In the extreme case, where $\mu = 0$, the error distribution becomes uniform, as depicted in Figure 3.2 (b). This uniform distribution indicates that, in the absence of alignment information, all directions are equally probable for beam alignment, resulting in maximum uncertainty regarding the optimal beam direction. In the case where $\mu = 1$, the error distribution approaches a Dirac delta function, $\delta(\epsilon)$, representing an ideal beam alignment with zero error, as shown in Figure 3.2 (c). However, achieving this ideal scenario is practically infeasible due to system imperfections, as shown in Figure 3.2 (d).

Furthermore, the expected value of the absolute error $|\epsilon|$ can be expressed as:

$$E\left[|\epsilon|\right] = \frac{\sqrt{2}\zeta}{\sqrt{\pi}\mu \operatorname{erf}\left(\frac{\mu b(\mu)}{\sqrt{2}\zeta}\right)}\left(1 - e^{\frac{-\mu^2 b(\mu)^2}{2\zeta^2}}\right), \tag{3.6}$$

as the level of alignment information μ approaches 1, the minimum expectation error for a practical system is given by:

$$\lim_{\mu\to 1} E\left[|\epsilon|\right] = \frac{\sqrt{2}\zeta}{\sqrt{\pi} \operatorname{erf}\left(\frac{\delta}{\sqrt{2}\zeta}\right)}\left(1 - e^{\frac{-\delta^2}{2\zeta^2}}\right), \tag{3.7}$$

for the ideal case, where the system has perfect alignment knowledge ($\mu = 1$) and $\delta = 0$, the expectation value of the absolute error approaches zero:

$$\lim_{\mu\to 1} E[|\epsilon|] = 0.$$

On the other hand, when there is no alignment information ($\mu = 0$), the expectation error reaches its maximum value:

$$\lim_{\mu\to 0} E[|\epsilon|] = \pi.$$

Finally, we define Δ as the probability that the beam alignment error ϵ falls within half the main lobe beamwidth η:

$$\Delta = \Pr\left[|\epsilon| \leq \frac{\eta}{2}\right] = \int_{-\eta/2}^{\eta/2} f_\epsilon(\epsilon)\, d\epsilon = \frac{\operatorname{erf}\left(\frac{\mu\,\eta}{2\sqrt{2}\,\zeta}\right)}{\operatorname{erf}\left(\frac{\mu\, b(\mu)}{\sqrt{2}\,\zeta}\right)},$$

where, $f_\epsilon(\epsilon)$ is the error PDF defined in (3.2), $b(\mu)$ is the dynamic truncation boundary, μ represents the alignment information parameter, and ζ is the inefficiency factor. This expression captures how alignment information, beamwidth, truncation boundary, and system imperfections jointly influence system performance. More details will be demonstrated in Section 3.3.

Without loss of generality, a flat-top antenna model is adopted, with $\delta = \frac{\eta}{2}$ assumed, establishing a baseline for future extensions using more complex antenna models.

3.2.5 Directional Beamforming and Antenna Model

In mmWave systems, antenna arrays are employed at both BSs and user equipment (UE) to perform directional beamforming [10]. For analytical tractability, the actual antenna array patterns are approximated by a sectored antenna model, also known as a flat-top model [11, 13]. The flat-top antenna pattern approximates the continuously varying array gain in a binary manner, where the gain is represented by two constant values: the peak main-lobe gain within the beamwidth and the side-lobe gain outside the main lobe [18, 190]. As shown in Figure 3.3, G_o^b denotes the main-lobe directivity gain, g^b represents the side-lobe directivity gain, and η_b signifies the beamwidth of the main-lobe. In this conventional model, essential performance parameters of the antenna arrays, such as G_o^b, g^b, and θ, are considered ideal [17]. The antenna gain is mathematically described as:

$$G(\theta) = \begin{cases} G_o^b & \text{if } |\theta| \leq \frac{\eta_b}{2} \\ g^b & \text{otherwise} \end{cases} \tag{3.8}$$

where the main-lobe gain G_o^b for an ideal sector antenna is given by :

$$G_o^b = \frac{2\pi - (2\pi - \eta_b)g^b}{\eta_b}.$$

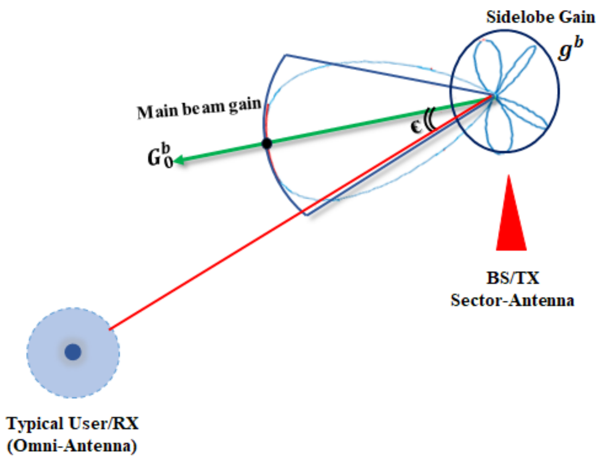

Figure 3.3: Illustration of the downlink scenario with a directional BS and an omni-antenna user. The BS employs a sectored antenna with main-lobe gain G_o^b, side-lobe gain g^b, and beamwidth η_b. The green arrow indicates the BS main-lobe direction, while the red arrow shows the received signal direction at the user. The angular difference between these two directions corresponds to the beam alignment error ϵ. The sectored antenna model is employed to approximate the directional beamforming pattern [11, 184].

This idealized sectored antenna model slightly overestimates the main-lobe directivity and neglects side-lobe variations, which can potentially affect system performance, resulting in an optimistic performance bound. Such a simplification is widely adopted in the literature to provide a baseline analytical framework. The effects of employing more realistic antenna patterns, including measured side-lobe variations and gradual main-lobe roll-off, are deferred to future work.

3.3 Coverage Probability

The coverage probability represents the probability that the signal-to-interference-plus-noise ratio (SINR) at the user exceeds a certain threshold [13]. Mathematically, it is defined as a complementary cumulative distribution function (CCDF), and expressed as $P_c(\gamma) = \mathbb{P}\left[SINR \geq \gamma\right]$ [184, 191]. The analysis focuses on the downlink SINR experienced by a typical user, located at the origin, as depicted in Figure 3.1. A generalized framework is first presented, incorporating alignment information at both the BS (μ_b) and the typical user (μ_u), covering both possible user antenna configurations: a directional antenna user, which can participate in beam alignment ($\mu_u \neq 0$) or an omni-antenna user without beamforming capability (i.e., no user-side alignment information is incorporated, ($\mu_u = 0$). This general framework captures all possible alignment scenarios at both ends of the communication link.

The analysis is then narrowed to the practical case where only the BS performs beamforming ($\mu_b \neq 0$), while the user employs an omni-antenna ($\mu_u = 0$). Closed-form expressions for the downlink coverage probability under LOS and NLOS conditions are derived. Scenarios that include the participation of the typical user in the alignment process can be considered in the future.

3.3.1 General Framework: Incorporating Alignment Information

A generalized framework is presented for analyzing the downlink coverage probability in mmWave networks, incorporating the alignment information at both the BS (μ_b) and the typical user (μ_u), where these parameters flexibly represent different levels of directional knowledge. Larger values correspond to higher confidence in alignment (smaller errors), while smaller values capture greater uncertainty (larger alignment errors or blind search). The general SINR expression, accounting for the alignment at both ends, is given in (3.9):

$$\mathrm{SINR} = \frac{P h_o G^{ab}_{\mu_b \neq 0}(\epsilon_b) G^{au}_{\mu_u \neq 0}(\epsilon_u)\; C r_o^{-\alpha}}{\sigma_n^2 + I_n} \tag{3.9}$$

In (3.9), h_o denotes the channel gain linked to the serving BS, r_o is a random variable defining the distance to the nearest BS from the typical user. Its distribution is defined by (3.1) (see Section 3.2.2). The parameters C and α represent the path-loss intercept and path loss exponent, respectively. Furthermore, ϵ_b and ϵ_u represent random variables characterizing the alignment error at the BS and the typical user, respectively. Finally, the terms σ_n^2 and I_n denote the noise power and aggregate interference, respectively. It is also assumed that all BSs provide service to users at the same power level P. The aggregate interference encountered by a typical user is defined as follows:

$$I_n = \sum_{\substack{i \in \Phi \\ (r_o, R)}} P\ h_i\ G^{Ib}_{i(\mu_b=0)}(\epsilon_b)\ G^{Iu}_{(\mu_u=0)}(\epsilon_u)\ C r_i^{-\alpha}, \tag{3.10}$$

here, the summation $\sum_{i \in \Phi(r_0, R)}$ is taken over all interfering BSs located in the annular region (r_0, R), at distances r_i from the typical user, outside the exclusion region defined by the serving BS at distance r_0 and within the network boundary $R = l\, r_0$, where $l > 1$ is a positive integer scaling factor. The gain expressions in (3.9) and (3.10) can be stated as follows:

G^{ab} : Gain of the serving BS at the typical user when $\mu_b \neq 0$.

G^{au} : Gain of the typical user at the serving BS when $\mu_u \neq 0$.

G^{Ib} : Gain of the interfering BS at the typical user when $\mu_b = 0$.

G^{Iu} : Gain of the typical user at the interfering BS when $\mu_u = 0$.

The interfering BSs are characterized by power fading random variables h_i and are assumed to have no alignment information with respect to the typical user $\mu_b = 0$ and no coordination. This assumption simplifies interference modeling and provides a conservative estimate of coverage probability, while allowing the analysis to focus solely on the effect of alignment information at the serving BS.

The coverage probability P_c can be expressed as follows:

$$\begin{aligned} P_c =& \mathbb{P}\left[\text{SINR} > \gamma\right] = \mathbb{P}\left[\frac{h_o G^{ab}_{\mu_b \neq 0}(\epsilon_b) G^{au}_{\mu_u \neq 0}(\epsilon_u)\ C r_o^{-\alpha}}{\sigma^2_{\bar{n}} + I_{\bar{n}}} > \gamma\right] \\ =& \mathbb{P}\left[h_o > \rho\left(\sigma^2_{\bar{n}} + I_{\bar{n}}\right)\right], \end{aligned} \tag{3.11}$$

where,

$$\rho = \frac{\gamma\ r_o^{\alpha}}{G^{ab}_{\mu_b \neq 0}(\epsilon_b)\ G^{au}_{\mu_u \neq 0}(\epsilon_u)\ C}$$

$I_{\bar{n}} = \frac{I_n}{P}$ represents the normalized aggregate interference, and $\sigma^2_{\bar{n}} = \frac{\sigma^2_n}{P}$, represents the normalized noise power, the coverage probability P_c is expressed as:

$$P_c = \mathbb{E}_{G^{ab}, G^{au}, r_o, I_{\bar{n}}}\left[e^{-\rho\sigma^2_{\bar{n}}} \cdot e^{-\rho I_{\bar{n}}}\right], \tag{3.12}$$

the formulation given in (3.12) arises from small-scale Rayleigh fading, represented as h_o, which follows an exponential distribution $h_o \sim \exp(1)$

[188].

$$
\begin{aligned}
P_c = &\int_{-b(\mu_u)}^{b(\mu_u)} \int_{-b(\mu_b)}^{b(\mu_b)} \int_{0}^{\infty} e^{-\rho\sigma_{\bar{n}}^2} \\
&\times \mathbb{E}_{\Phi,G^{Ib},G^{Iu},h}\left[e^{-\rho\sum_{i\in\Phi} h_i G^{Ib}_{(\mu_b=0)} G^{Iu}_{(\mu_u=0)} C r_i^{-\alpha}}\right] \\
&\times f_{R_o}(r_o)\cdot f_{\epsilon_b}(\epsilon_b)\cdot f_{\epsilon_u}(\epsilon_u)\, dr_o\; d\epsilon_b\; d\epsilon_u
\end{aligned}
\tag{3.13}
$$

Now, we focus on solving the expectation term in (3.13), which can be expressed as follows:

$$
\mathbb{E}_{\Phi,G^{Ib},G^{Iu},h}\left[\prod_{i\in\Phi} e^{-\rho h_i G^{Ib}_{(\mu_b=0)} G^{Iu}_{(\mu_u=0)} C r_i{}^{-\alpha}}\right]
$$

The expectation term can be further simplified using two steps:

$$
\overset{(a)}{=} \exp\left(\int_{(r_o,R)} \mathbb{E}_{G^{Ib},G^{Iu},h}[e^{-\rho h G^{Ib} G^{Iu} C r^{-\alpha}} - 1] d\Lambda(\bar{r})\right)
$$

$$
\overset{(b)}{=} \exp\left(\int_{(r_o,R)} \mathbb{E}_{G^{Ib},G^{Iu}}\left[\frac{-\rho G^{Ib} G^{Iu} C r^{-\alpha}}{1+\rho G^{Ib} G^{Iu} C r^{-\alpha}}\right] d\Lambda(\bar{r})\right)
\tag{3.14}
$$

Here,

(a) This term results from applying the Probability Generating Functional (PGFL) of the point process.

(b) This term arises from the fact that h follows an exponential distribution, $h \sim \exp(1)$.

The expression in (3.13) represents the general form of system model, incorporating alignment information at both the serving BS (μ_b) and the typical user (μ_u). This general framework is presented to show that the model can cover different user antenna configurations: either a directional antenna user, which can participate in beam alignment ($\mu_u \neq 0$), or an omni-antenna user, which cannot perform beamforming and therefore does not contribute any user-side alignment information ($\mu_u = 0$). In the following subsections, we focus on the practical case where only the BS performs beamforming ($\mu_b \neq 0$), while the user employs an omni-antenna. This allows us to derive tractable expressions for the coverage probability under LOS and NLOS conditions.

3.3.2 Case Study: Impact of Base Station Information

In our analytical model presented in this thesis, we focus solely on the beam alignment information (μ_b) available at the serving BS. We assume that the typical user employs omni-antenna and does not perform any beamforming. Consequently, the alignment information from the user's perspective is not considered ($\mu_u = 0$),

For a typical user with an omni-antenna, $\eta_u = 2\pi$, we have:

$$G^{au} = G^{Iu} = 1 \tag{3.15a}$$

$$b(\mu_u = 0) = \pi \tag{3.15b}$$

$$\lim_{\mu_u \to 0} f_{\epsilon_u}(\epsilon_u) = \frac{1}{2\pi} \tag{3.15c}$$

Based on (3.15-a), (3.14) can be rewritten as:

$$\exp\left(\int_{(r_o,R)} \mathbb{E}_{G^{Ib}_{\mu=0}}\left[\frac{-\rho G^{Ib}Cr^{-\alpha}}{1+\rho G^{Ib}Cr^{-\alpha}}\right] d\Lambda(\bar{r})\right) \tag{3.16}$$

$$\text{with } \rho = \frac{\gamma\ r_o^{\alpha}}{G^{ab}\ C}$$

given that G^{Ib} is evaluated at $\mu_b = 0$, according to (3.5a), the PDF of alignment error for interference BSs will be a uniform distribution over the interval $[-\pi, \pi]$, as shown in Figure 3.4. Then, (3.16) can be written as:

$$\begin{aligned}\exp\Bigg(&\frac{\eta_b}{2\pi}\int_{r_o}^{R}\left(\frac{-\rho\ G_o^bCr^{-\alpha}}{1+\rho\ G_o^bCr^{-\alpha}}\right)2\pi\lambda r\,dr+\\ &\left(1-\frac{\eta_b}{2\pi}\right)\int_{r_o}^{R}\left(\frac{-\rho\ g^bCr^{-\alpha}}{1+\rho\ g^bCr^{-\alpha}}\right)2\pi\lambda r\,dr\Bigg)\end{aligned} \tag{3.17}$$

For the first integral, we have:-

$$= \pi\lambda R^2\ \ {}_2F_1\left(\frac{-G^{ab}}{G_o^b\gamma}\left(\frac{R}{r_o}\right)^{\alpha}\right) - \pi\lambda r_o^2\ \ {}_2F_1\left(\frac{-G^{ab}}{G_o^b\gamma}\right) \tag{3.18}$$

for the second integral, we have:-

$$= \pi\lambda R^2\ \ {}_2F_1\left(\frac{-G^{ab}}{g^b\gamma}\left(\frac{R}{r_o}\right)^{\alpha}\right) - \pi\lambda r_o^2\ \ {}_2F_1\left(\frac{-G^{ab}}{gb\gamma}\right) \tag{3.19}$$

here, ${}_2F_1(\cdot)$ represents the hypergeometric function, and we utilize the form ${}_2F_1(\cdot) = {}_2F_1\left(1, \frac{2}{\alpha}; \frac{2}{\alpha}+1; (\cdot)\right)$, where, g^b represents the side lobe gain of BS.

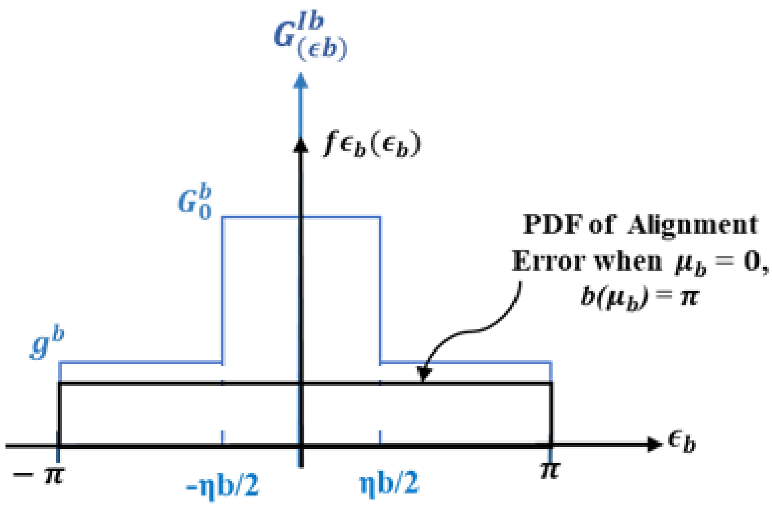

Figure 3.4: Illustration of the PDF of alignment error $f_{\epsilon_b}(\epsilon_b)$ for the interfering BSs with information parameter ($\mu_b = 0$), resulting in a uniform distribution of $1/2\pi$. The figure also shows the flat-top antenna gain with main lobe ($G_o^b = G_o^{Ib}$) and side lobe ($g^b = g^{Ib}$) for the interfering BS gain (G^{Ib}). The vertical scales of the PDF and the antenna gain curves are independent and not comparable. The figure is schematic and not to scale; relative heights are shown only for visualization.

Let the expressions in (3.18) and (3.19) be denoted as B and D, respectively. By using (3.15-b), (3.15-c), and substituting (3.18) and (3.19) into (3.13), we obtain:

$$P_c = \int_0^{\infty} \int_{-b(\mu_b)}^{b(\mu_b)} e^{-\left(\rho\,\sigma_n^2 + \frac{\eta_b}{2\pi} B + \left(1 - \frac{\eta_b}{2\pi}\right) D + \pi\lambda r_o^2\right)}\, 2\pi\lambda r_o f_{\epsilon_b}(\epsilon_b)\, dr_o\, d\epsilon_b \tag{3.20}$$

The expression in (3.20) represents the downlink coverage probability P_c when considering alignment information μ_b at the serving BS. This expression is applicable in scenarios where the typical user employs an omni-antenna and is derived for the specific cases where the path loss exponent α is set to 2 and 4. In the subsequent sections, we will derive specific solutions for these two values of the path loss exponent.

3.3.2.1 Path Loss Exponent ($\alpha = 2$)

For the specific case where we set $\alpha = 2$, and to facilitate a tractable mathematical analysis without loss of generality, we assume that $R = l r_o$ with $l > 1$ (see Figure 3.1). Solving (3.18) and (3.19) under these conditions, we can express the terms B and D as follows:

$$B^{(\alpha=2)} = \pi\lambda r_o^2 \left(\frac{\gamma\, G_o^b}{G^{ab}}\right) \ln\left(\frac{\frac{\gamma\, G_o^b}{G^{ab}} + l^2}{\frac{\gamma\, G_o^b}{G^{ab}} + 1}\right) \tag{3.21}$$

$$D^{(\alpha=2)} = \pi\lambda r_o^2 \left(\frac{\gamma\, g^b}{G^{ab}}\right) \ln\left(\frac{\frac{\gamma\, g^b}{G^{ab}} + l^2}{\frac{\gamma\, g^b}{G^{ab}} + 1}\right) \tag{3.22}$$

by substituting (3.21) and (3.22) into (3.20), and solving the integrals for $\alpha = 2$, see Figure 3.5, the expression for P_c becomes:

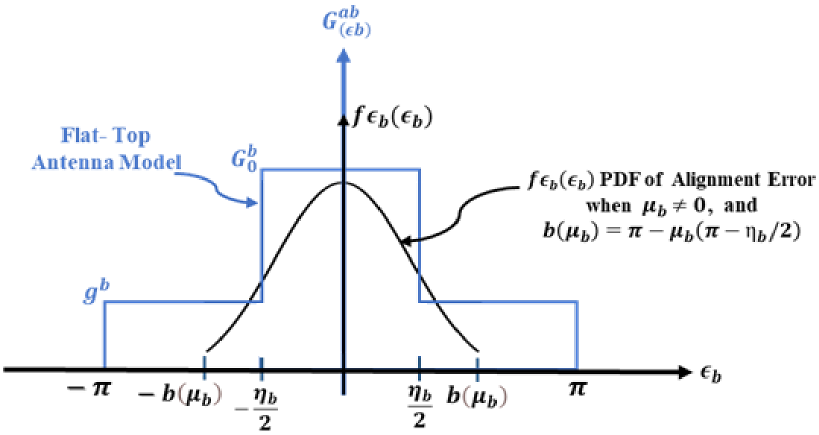

Figure 3.5: Illustration of the truncated Gaussian PDF of alignment error $f_{\epsilon_b}(\epsilon_b)$ for the serving BS with information parameter $0 < \mu_b \leq 1$. The figure also shows the flat-top antenna gain pattern with main lobe ($G^b_o = G^{ab}_o$) and side lobe gain ($g^b = g^{ab}$) for the serving BS gain G^{ab}. The figure is schematic and not to scale.

$$P_c = \frac{\Delta^b}{\left(1 + \frac{\gamma\sigma_n^2}{G^b_o C\pi\lambda}\right) + \left(\frac{\eta_b}{2\pi}\right) B_o + \left(1 - \frac{\eta_b}{2\pi}\right) D_o} +$$

$$\frac{\left(1 - \Delta^b\right)}{\left(1 + \frac{\gamma\sigma_n^2}{g^b C\pi\lambda}\right) + \left(\frac{\eta_b}{2\pi}\right) B_g + \left(1 - \frac{\eta_b}{2\pi}\right) D_g}, \tag{3.23}$$

where :

$$B_o = \gamma \ \ln\left(\frac{\gamma + l^2}{\gamma + 1}\right)$$

$$D_o = \left(\frac{g^b\gamma}{G^b_o}\right) \ \ln\left(\frac{\frac{g^b\gamma}{G^b_o} + l^2}{\frac{g^b\gamma}{G_o} + 1}\right)$$

$$B_g = \frac{G_o^b\gamma}{g^b} \ \ln\left(\frac{\frac{G_o^b\gamma}{g^b}+l^2}{\frac{G_o\gamma}{g^b}+1}\right)$$

$$D_g = \gamma \ \ln\left(\frac{\gamma+l^2}{\gamma+1}\right)$$

$$\Delta^b = \begin{cases} \frac{\operatorname{erf}\left(\frac{\mu_b\eta_b}{2\sqrt{2}\sigma_b}\right)}{\operatorname{erf}\left(\frac{\mu_b b(\mu_b)}{\sqrt{2}\sigma_b}\right)} & \text{if } b(\mu_b) \geq \frac{\eta_b}{2} \\ 1 & \text{if } b(\mu_b) < \frac{\eta_b}{2} \end{cases} \tag{3.24}$$

We defined $\delta_b = \eta_b/2$, then $b(\mu_b) \geq \eta_b/2$.

$$\Rightarrow \Delta^b = \frac{\operatorname{erf}\left(\frac{\mu_b\eta_b}{2\sqrt{2}\sigma_b}\right)}{\operatorname{erf}\left(\frac{\mu_b b(\mu_b)}{\sqrt{2}\sigma_b}\right)}$$

The expression Δ^b encapsulates the impact of alignment error on coverage probability P_c, highlighting the sensitivity of system performance to variations in alignment information μ_b. The expression derived in (3.23) for the coverage probability P_c under the path loss exponent $\alpha = 2$. As we move to analyzing the case with a path loss exponent $\alpha = 4$, we build on these foundational results to explore how different propagation characteristics further shape P_c.

3.3.2.2 Path Loss Exponent ($\alpha = 4$)

In the second specific case, under the same assumption that $R = lr_o$, $l > 1$, and solving (3.18) and (3.19) for $\alpha = 4$, we can express the terms B and D as follows:

$$B^{(\alpha=4)} = \left[\tan^{-1}\left(\frac{l^2}{\sqrt{\frac{G_o^b\gamma}{G^{ab}}}}\right) - \tan^{-1}\left(\frac{l^2}{\sqrt{\frac{G_o^b\gamma}{G^{ab}}}}\right)\right]\pi\lambda r_o^2\sqrt{\left(\frac{G_o^b\gamma}{G^{ab}}\right)} \tag{3.25}$$

$$D^{(\alpha=4)} = \left[\tan^{-1}\left(\frac{l^2}{\sqrt{\frac{g^b\gamma}{G^{ab}}}}\right) - \tan^{-1}\left(\frac{l^2}{\sqrt{\frac{g^b\gamma}{G^{ab}}}}\right)\right]\pi\lambda r_o^2\sqrt{\left(\frac{g^b\gamma}{G^{ab}}\right)} \tag{3.26}$$

Substituting (3.25) and (3.26) into (3.20), and solving for $\alpha = 4$, yields:-

$$\begin{aligned} P_c = {} & \frac{\pi^{3/2}\lambda\sqrt{G_o^b C}}{2\sigma_{\bar{n}}\sqrt{\gamma}}\; e^{\left(\frac{\pi^2\lambda^2 G_o^b C}{4\gamma\sigma_{\bar{n}}^2}\left(1+\frac{\eta_b}{2\pi}\tilde{B}_o+\left(1-\frac{\eta_b}{2\pi}\right)\tilde{D}_o\right)^2\right)} \\ & \operatorname{erfc}\left[\frac{\pi\lambda\sqrt{G_o^b C}\left(1+\frac{\eta_b}{2\pi}\tilde{B}_o+\left(1-\frac{\eta_b}{2\pi}\right)\tilde{D}_o\right)}{2\sigma_{\bar{n}}\sqrt{\gamma}}\right]\Delta^b \\ & + \frac{\pi^{3/2}\lambda\sqrt{g^b C}}{2\sigma_{\bar{n}}\sqrt{\gamma}} \cdot e^{\left(\frac{\pi^2\lambda^2 G_o^b C}{4\gamma\sigma_{\bar{n}}^2}\left(1+\frac{\eta_b}{2\pi}\tilde{B}_g+\left(1-\frac{\eta_b}{2\pi}\right)\tilde{D}_g\right)^2\right)} \\ & \operatorname{erfc}\left[\frac{\pi\lambda\sqrt{g^b C}\left(1+\frac{\eta_b}{2\pi}\tilde{B}_g+\left(1-\frac{\eta_b}{2\pi}\right)\tilde{D}_g\right)}{2\sigma_{\bar{n}}\sqrt{\gamma}}\right](1-\Delta^b), \end{aligned} \tag{3.27}$$

where:

$$\tilde{B}_o = \sqrt{\gamma}\left[\tan^{-1}\left(\frac{l^2}{\sqrt{\gamma}}\right) - \tan^{-1}\left(\frac{1}{\sqrt{\gamma}}\right)\right]$$

$$\tilde{D}_o = \sqrt{\frac{g^b\gamma}{G_o^b}}\left[\tan^{-1}\left(\frac{l^2}{\sqrt{\frac{g^b\gamma}{G_o^b}}}\right) - \tan^{-1}\left(\frac{1}{\sqrt{\frac{g^b\gamma}{G_o^b}}}\right)\right]$$

$$\tilde{B}_g = \sqrt{\frac{G_o^b\gamma}{g^b}}\left[\tan^{-1}\left(\frac{l^2}{\sqrt{\frac{G_o^b\gamma}{g^b}}}\right) - \tan^{-1}\left(\frac{1}{\sqrt{\frac{G_o^b\gamma}{g^b}}}\right)\right]$$

$$\tilde{D}_g = \sqrt{\gamma}\left[\tan^{-1}\left(\frac{l^2}{\sqrt{\gamma}}\right) - \tan^{-1}\left(\frac{1}{\sqrt{\gamma}}\right)\right]$$

The expression derived in (3.27) represents the coverage probability P_c for a path loss exponent $\alpha = 4$, which typically models NLOS conditions with higher path loss. By analyzing both $\alpha = 2$ (representing LOS conditions) to $\alpha = 4$, we provide a comparison of how varying environmental conditions affect coverage probability.

In the next section, we present simulation results that validate the analytical model, confirming its applicability in real-world deployment scenarios.

3.4 Simulation Results

This section analyzes the performance of a mmWave network in the presence of beam alignment errors and verifies the precision of the developed analytical framework through Monte Carlo simulations. The coverage probability expressions P_c derived in Section 3.3 for LOS and NLOS conditions, given in (3.23) and (3.27), respectively, are evaluated under different network configurations. The results examine the impact of the alignment information available at the serving BS, represented by μ_b, the serving BS beamwidth η_b, BS density λ_b, and fading models on the downlink coverage probability P_c. Table 3.1 presents the key simulation parameters.

3.4.1 Coverage Analysis

The analysis begins with the first scenario, corresponding to a path loss exponent of $\alpha_L = 2$. The simulation parameters are set as follows: a path

Table 3.1: Simulation Parameters

Notation	Description	Value	Reference
λ_b	BS density	50/km^2	[18]
g_b	BS antenna gain-sidelobe	-10 (dBi)	–
α_L, α_N	LOS and NLOS path loss exponents, respectively	2, 4	[188]
C_L, C_N	LOS and NLOS path loss intercepts, respectively	-60 dB, -70 dB	[188]
f_c	Carrier frequency	28 GHz	[13]
W	Bandwidth	100 MHz	[13]
ζ_b	Antenna system inefficiency factor	0.158	–
l	Positive integer scaling factor ($l > 1$, $R = r_o\, l$)	8	–
σ_n^2	Noise power	- 174 dBm/Hz + 10 $\log_{10}(W)$ + 10 dB	[18]

loss intercept $C_L = -60$ dB, a BS downlink transmit power of $P_t = 30$ dBm, and a BS density of $\lambda_b = 50\,\text{km}^{-2}$. The disk radius of PPP is determined by $R = r_o l$.

Figure 3.6 shows the coverage probability P_c against SINR thresholds for perfect alignment information ($\mu_b = 1$), partial information ($\mu_b = 0.5$), and no information ($\mu_b = 0$). It can be seen that when $\mu_b = 1$, the coverage probability P_c is the highest across the range of SINR values, indicating that perfect alignment information leads to the best performance in terms of coverage. For $\mu_b = 0.5$, P_c decreases, showing that the coverage probability is compromised when alignment information is not perfect. This reduction in P_c reflects the impact of uncertainty in alignment, which results in less effective beamforming.

When $\mu_b = 0$, indicating that there is no alignment information, the coverage probability P_c is the lowest. This scenario highlights the significant

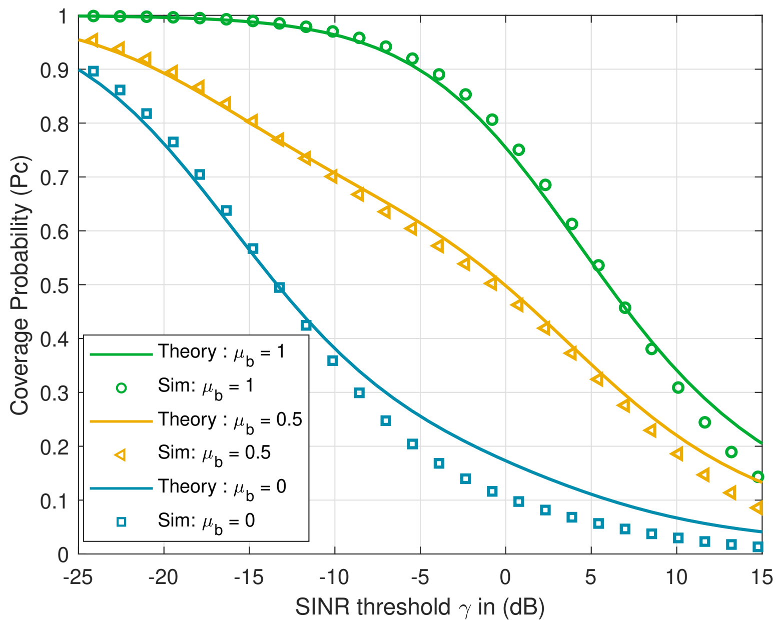

Figure 3.6: Coverage probability P_c theory and Monte Carlo simulation vs SINR for $\alpha_L = 2$. The system utilizes the following parameters: $C_L = -60\,$dB, BS downlink transmit power $P_t = 30\,$dBm, with beamwidth $\eta_b = 30^o$, BS density $\lambda_b = 50/km^2$.

degradation in coverage performance due to the lack of alignment information. Thus, the quality of alignment information plays a crucial role in determining the coverage probability, with perfect alignment ($\mu_b = 1$) providing the best performance, and the performance progressively deteriorating as the quality of alignment information decreases.

It is important to note that the analytical predictions tend to deviate from the results of the Monte Carlo simulation at high SINR thresholds. In our model, an exclusion zone of radius r_o around the typical user ensures that only the serving BS is excluded, while all other BSs at $r_i > r_o$ contribute to interference. The deviation arises because the mean interference in a PPP network is finite only if the path loss exponent $\alpha > 2$, whereas for $\alpha = 2$, the interference from distant BSs beyond the exclusion zone remains significant and decays slowly, which can cause cumulative interference to diverge, as discussed in Example 5 of [180]. This slow decay of interference explains the observed deviation between the analytical and simulation results at high SINR thresholds. In subsequent figures that also consider $\alpha = 2$, similar trends will be observed.

In Figure 3.7, we investigate the impact of different BS beamwidths (η_b) on the downlink coverage probability under perfect alignment information ($\mu_b = 1$). The beamwidths considered are $\eta_b = 30°$, $\eta_b = 15°$, and $\eta_b = 5°$. The results show that the narrowest beamwidth, $\eta_b = 5°$, provides the highest coverage probability compared to wider beamwidths. This trend is attributed to the more focused transmission and reduced interference, which enhances the received signal quality. Therefore, $\eta_b = 5°$ offers favorable performance in terms of coverage probability for the omni-user scenario with

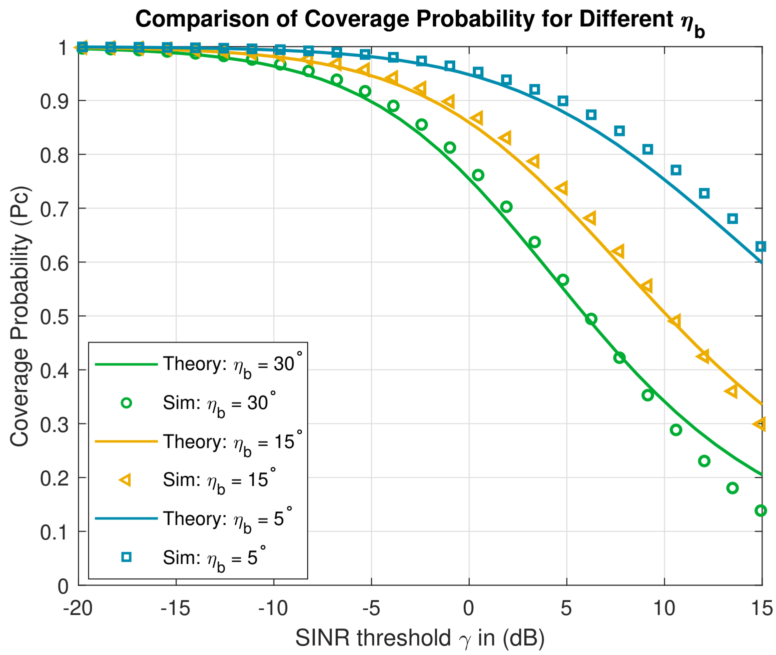

Figure 3.7: Coverage probability P_c theory and Monte Carlo simulation vs SINR for $\alpha_L = 2$. The system utilizes the following parameters: $C_L = -60\,$dB, $P_t = 30\,$dBm, $\lambda_b = 50/km^2$, and information parameter ($\mu_b = 1$).

perfect alignment information.

To further examine this relationship, Figure 3.8 presents the coverage probability P_c at an SINR threshold of 5 dB as a function of the alignment information parameter μ_b, over the entire range $\mu_b \in [0, 1]$. The analysis considers three different serving BS beamwidths: $\eta_b = 90°$, $\eta_b = 30°$, and $\eta_b = 5°$.

For the wide beam (90°), when the serving BS has low-level alignment information ($0 \leq \mu_b \leq 0.3$), the coverage probability initially increases gradually with μ_b, indicating that improvements in alignment knowledge within this range enhance performance. Between $\mu_b = 0.3$ and $\mu_b = 0.4$, the coverage probability rises slightly from approximately 0.257 to 0.278. Then stabilizes around 0.280 for $\mu_b \approx 0.42$, showing no noticeable improvement beyond this point. Therefore, $\mu_b \approx 0.42$ represents a critical transition point and can be considered a practical design threshold for wide beams, since additional alignment information beyond this value does not provide a meaningful performance gain.

The 30° beamwidth (medium beamwidth) begins to outperform both the 90° and 5° beamwidths once the availability of alignment information μ_b exceeds 0.3, suggesting that medium beamwidths benefit more from increased alignment information, especially at intermediate levels of μ_b. This advantage becomes particularly apparent when the alignment information level is high, but not yet perfect. Therefore, the medium beamwidth provides a more balanced solution, benefits from improved alignment knowledge without requiring the extreme precision needed by narrow beams, and at the same time, it offers better performance than the wider and narrower beamwidths

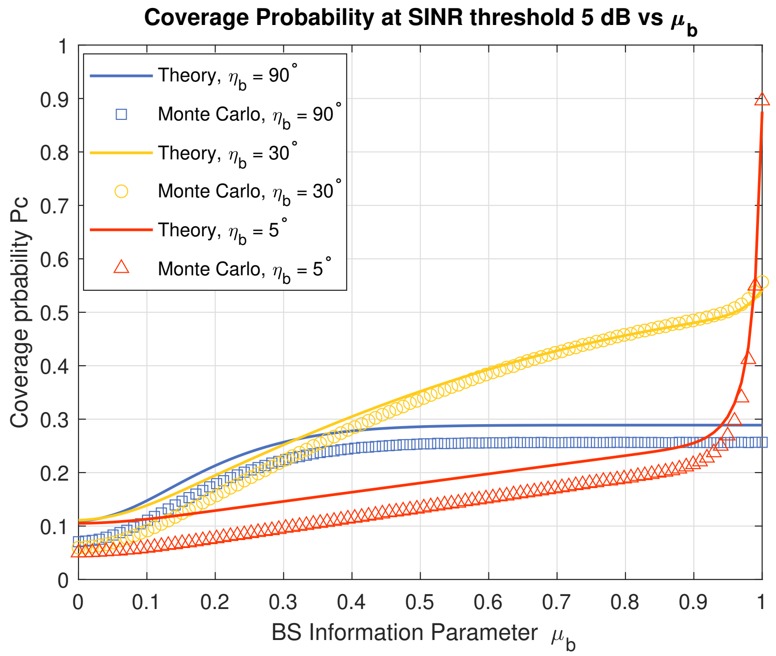

Figure 3.8: Coverage probability P_c (theoretical and Monte Carlo simulation) as a function of the serving BS alignment information parameter μ_b for $\alpha_L = 2$. This analysis examines three distinct serving BS beamwidths: $\eta_b = 90°$, $\eta_b = 30°$, and $\eta_b = 5°$, with a SINR threshold set at 5 dB. The system parameters include: $C_L = -60$ dB, $P_t = 30\,$dBm, $\lambda_b = 50\,$BS/km^2.

in these intermediate availability of alignment information scenarios.

The 5° beamwidth (narrow beam) outperforms both wider beamwidths at very high alignment information levels ($\mu_b > 0.98$), where the availability of alignment information reaches near perfection.

In summary, our results reveal that while wider beamwidths benefit from increased alignment information, their performance plateaus after a certain threshold ($\mu_b \approx 0.42$). In contrast, medium beamwidths ($\eta_b = 30^\circ$) consistently outperform both wider and narrower beams in intermediate knowledge scenarios ($0.3 < \mu_b < 0.98$), while narrow beamwidths ($\eta_b = 5^\circ$) excel when alignment information is nearly perfect ($\mu_b > 0.98$). This highlights the critical role of beamwidth selection in relation to the level of alignment information availability in the mmWave communication systems.

We now turn to the second scenario in our analysis, where the path loss exponent is $\alpha_N = 4$. Figure 3.9 presents the Monte Carlo simulation results alongside our analytical model, comparing the downlink coverage probability, P_C, for different levels of alignment information at the serving BS: perfect information ($\mu_b = 1$), partial information ($\mu_b = 0.5$), and no information ($\mu_b = 0$). Here, μ_b represents the beam alignment information availability and corresponds to the parameter μ defined in Section 3.2.4.

It is evident that when the serving BS possesses complete alignment information ($\mu_b = 1$), the coverage probability is significantly higher compared to scenarios with partial or no alignment information. The simulation parameters for this figure include a transmit power of $P_t = 30\,\text{dBm}$.

In Figure 3.10, the simulation parameters remain the same as those in Figure 3.9, except for an increased transmit power of $P_t = 40\,\text{dBm}$. The re-

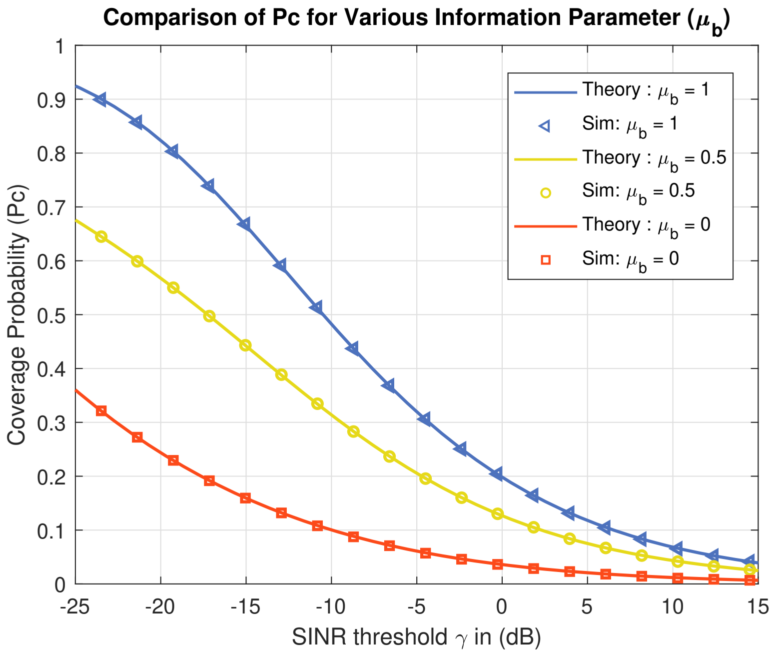

Figure 3.9: Coverage probability P_c theory and Monte Carlo simulation vs SINR for $\alpha_N = 4$. Results are shown for different beam alignment information availability at the serving BS: perfect information ($\mu_b = 1$), partial information ($\mu_b = 0.5$), and no information ($\mu_b = 0$), where μ_b corresponds to the alignment information parameter μ defined in Section 3.2.4. The system utilizes the following parameters: $C_N = -70\ dB$, $P_t = 30\,$dBm, $\eta_b = 30^o$, $\lambda_b = 50/km^2$.

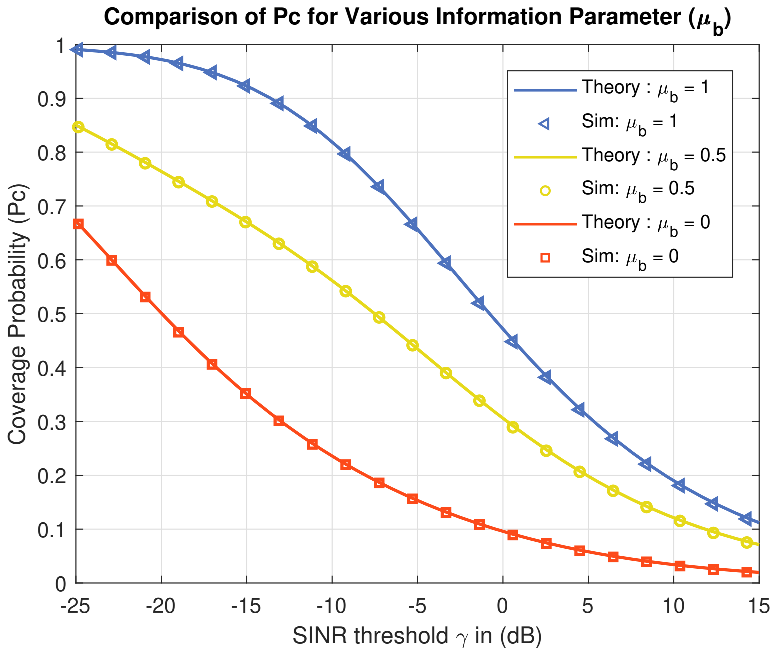

Figure 3.10: Coverage probability P_c theory and Monte Carlo simulation vs SINR for $\alpha_N = 4$. The system utilizes the following parameters: $C_N = -70\ dB$, $P_t = 40\,$dBm, $\eta_b = 30^o$, and $\lambda_b = 50/km^2$.

sults indicate an enhanced coverage probability across all levels of alignment information, demonstrating the positive effect of increased transmit power on the system's performance. This improvement in coverage is particularly notable when the path loss exponent is $\alpha_N = 4$. Such an improvement is not observed when the path loss exponent is $\alpha_L = 2$, underscoring the significance of transmit power in environments with higher path loss. To further interpret the results, consider a SINR threshold of -15 dB. At this operating point, the coverage probability is approximately 0.92 for perfect alignment information ($\mu_b = 1$), 0.67 for partial alignment information ($\mu_b = 0.5$), and 0.35 when no alignment information is available ($\mu_b = 0$). These results demonstrate that improved information at the serving BS substantially increases the coverage probability by reducing beam misalignment effects. Although relatively high coverage is achieved at low SINR thresholds, the coverage probability decreases rapidly as the SINR threshold becomes more stringent. For example, at a SINR threshold of 10 dB, the coverage probability falls to approximately 0.20, 0.11, and 0.03 for $\mu_b = 1$, $\mu_b = 0.5$, and $\mu_b = 0$, respectively. The perfect alignment information case achieves a high coverage probability at a low SINR threshold (e.g., $P_c \approx 0.92$ at -15 dB); however, the coverage probability becomes substantially lower when partial or no alignment information is available and when higher SINR thresholds are required. At higher SINR thresholds, most operating points in the considered configuration achieve coverage probabilities that are considerably lower than the high coverage levels generally required for practical network operation.

Figure 3.11 depicts the coverage probability P_C across various BS beamwidths (η_b) under perfect alignment conditions ($\mu_b = 1$). The considered beamwidths

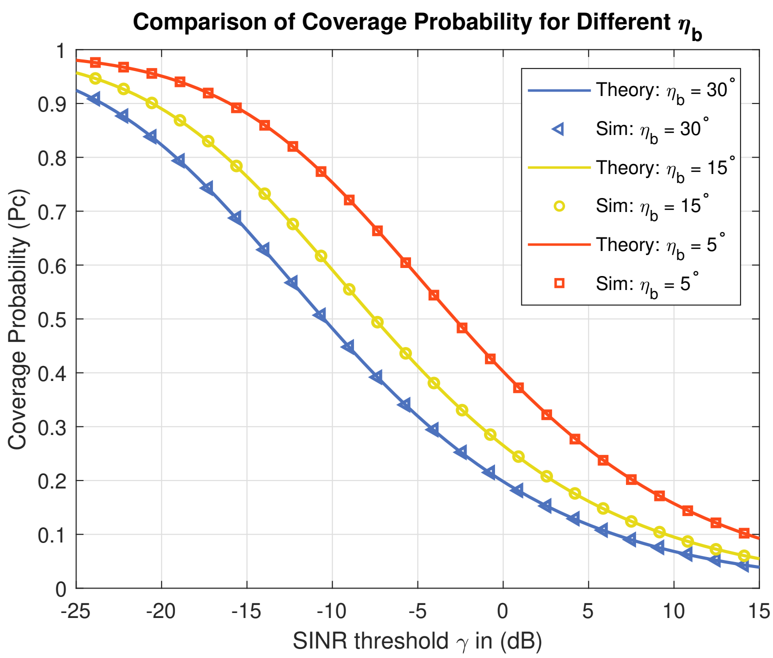

Figure 3.11: Coverage probability P_c theory and Monte Carlo simulation vs SINR for $\alpha_N = 4$. The system parameters are as follows: $P_t = 30$ dBm, $C_N = -70$ dB, $\lambda_b = 50$ BS/km^2, and information parameter ($\mu_b = 1$).

include $\eta_b = 30°$, $\eta_b = 15°$, and $\eta_b = 5°$. Notably, $\eta_b = 5°$ exhibits the highest P_C compared to wider beamwidths. This superiority arises from the enhanced focus and reduced interference achieved with narrower beams, particularly notable under conditions of perfect alignment. Consequently, $\eta_b = 5°$ stands out as the optimal choice for maximizing coverage probability in mmWave systems under perfect alignment conditions.

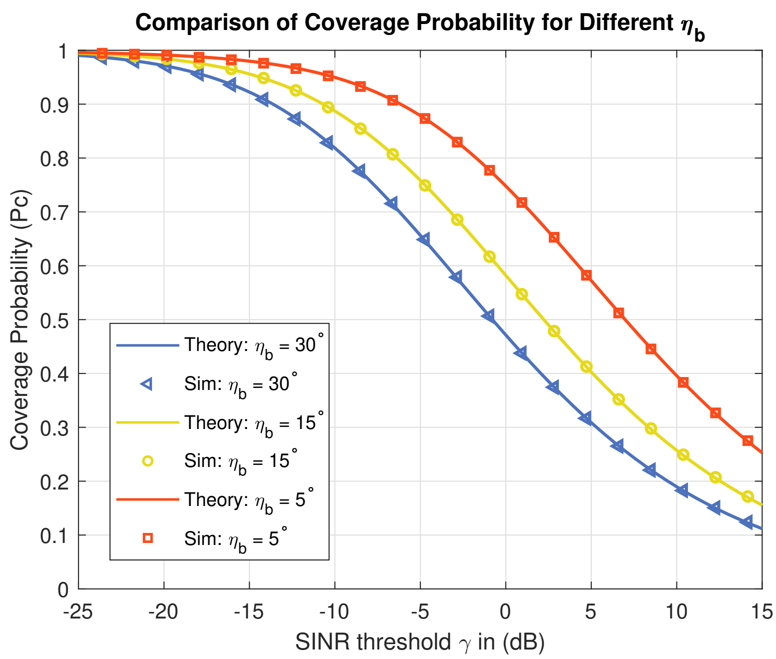

Figure 3.12: Coverage probability P_c theory and Monte Carlo simulation vs SINR for $\alpha_N = 4$. The system parameters are as follows: $P_t = 40$ dBm, $C_N = -70$ dB, $\lambda_b = 50$ BS/km^2, and information parameter ($\mu_b = 1$).

In Figure 3.12, the coverage probability P_C is depicted for different BS beamwidths (η_b), assuming perfect alignment information ($\mu_b = 1$). The primary distinction between Figure 3.12 and Figure 3.11 lies in the BS transmit power (P_t) configuration. Notably, Figure 3.12 explores the scenario where P_t is set to 40 dBm, showcasing improved coverage probability compared to

Figure 3.11, where P_t is 30 dBm. This difference highlights the crucial role of transmit power in improving coverage performance under $\alpha_N = 4$.

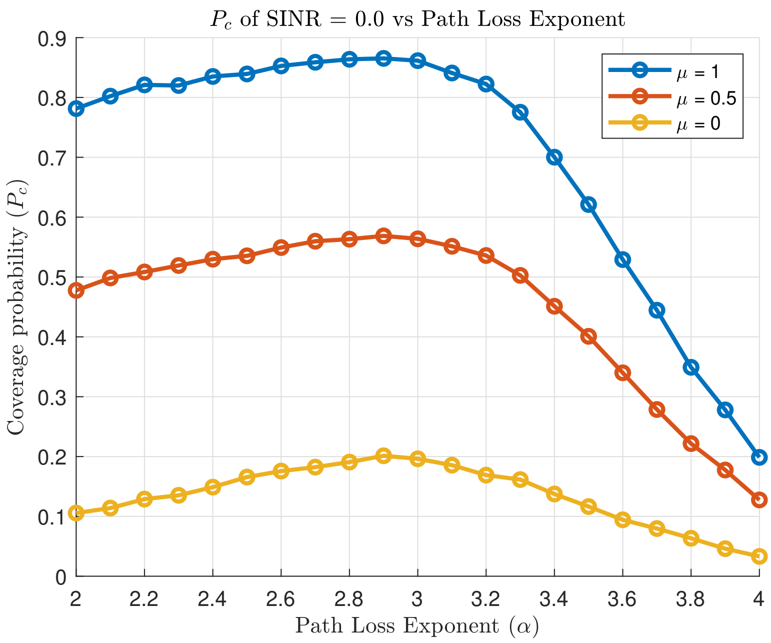

Figure 3.13: Coverage probability P_c by Monte Carlo simulation vs. path-loss exponent, with system parameters: $P_t = 40$ dBm, BS $\eta_b = 30°$, $\lambda_b = 50/\text{km}^2$.

Figure 3.13 illustrates the impact of the availability of beam alignment information at the serving BS, μ_b, under different path loss exponents α on the network coverage. The results highlight that under varying path loss exponents, higher levels of alignment information at the BS (μ_b) consistently result in superior performance compared to scenarios where the BS has partial or no alignment information. This emphasizes the critical role of alignment knowledge in achieving better coverage, especially in environments with significant path loss effects. In addition, the results demonstrate a non-monotonic relationship between the path loss exponent α and the coverage probability for all values of μ_b. Specifically, the coverage probability initially increases as α increases from 2.1 to approximately 2.8 – 2.9, after which it decreases significantly. This trend is due to the different impact of path loss on the desired and interfering signals. For moderate values of α, interference from interfering BSs is attenuated more rapidly than the desired signal, improving SINR and increasing coverage probability. However, as α increases further (beyond $\alpha \approx 2.9$), the desired signal from the serving BS also experiences stronger attenuation, which ultimately degrades the SINR and reduces coverage.

3.4.2 Simulation-Based Comparison of channel fading models

To validate the theoretical assumption of Rayleigh fading adopted in Section 3.2.3, this subsection presents a Monte Carlo simulation-based comparison of several commonly used fading models for mmWave channels. These include Rayleigh, Rician, Nakagami, and a no-fading scenario. The impact of these models on downlink coverage probability is evaluated under both LOS and NLOS conditions. For the Rician fading model, K-factor of 3 dB and 6 dB are selected for LOS scenarios, based on measurement studies in mmWave environments [192–194]. For NLOS conditions, a K-factor of -5 dB is used [192]. Different parameters for Nakagami fading are set to $M_L = 3$ for LOS and $M_N = 2$ for NLOS, respectively [11, 18].

Table 3.2 provides a measurement-based overview of the Rician K-factor in typical mmWave environments, supporting the selection of representative values used in simulations.

Figures 3.14 and 3.15 compare the downlink coverage probability P_c for

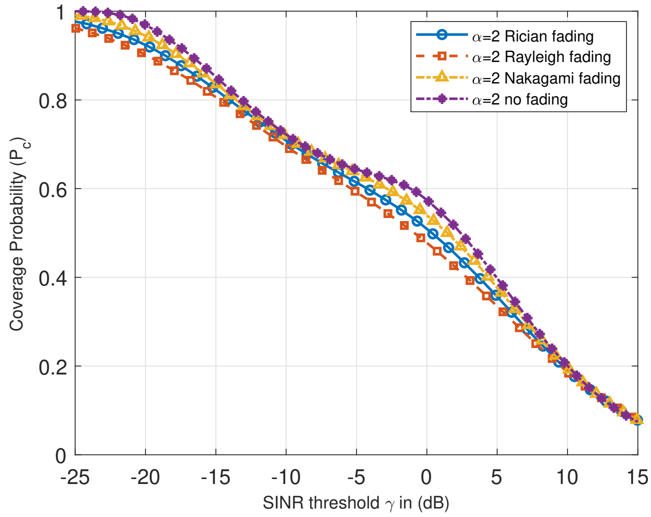

(a) Coverage probability for various fading models.

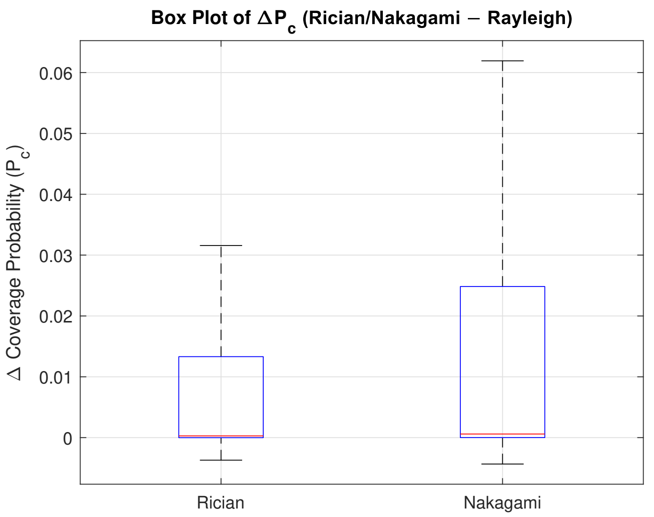

(b) Coverage probability difference relative to Rayleigh.

Figure 3.14: Monte Carlo simulation results comparing fading models under LOS conditions ($\alpha_L = 2$), with Rician fading ($K = 3$ dB), Nakagami fading ($M_L = 3$), and no fading scenario. Subfigure (a) shows downlink coverage probability across Rayleigh, Rician, Nakagami, and no fading models. Subfigure (b) presents a boxplot showing the distribution of coverage probability differences (ΔP_c) for Rician and Nakagami fading relative to the Rayleigh baseline; the red line indicates the median (ΔP_c).

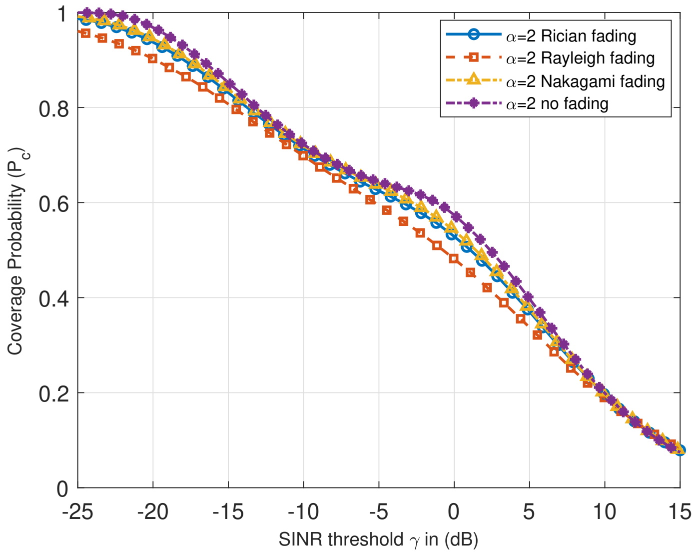

(a) Coverage probability for various fading models.

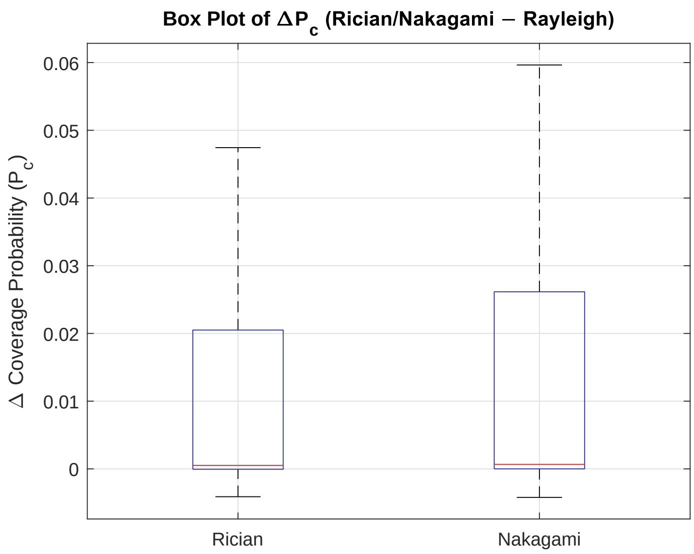

(b) Coverage probability difference relative to Rayleigh.

Figure 3.15: Monte Carlo simulation results under LOS conditions ($\alpha_L = 2$) with Rician fading ($K = 6$ dB), Nakagami fading ($M_L = 3$), and no fading scenario. Subfigure (a) shows downlink coverage probability across Rayleigh, Rician, Nakagami, and no fading models. Subfigure (b) presents a boxplot illustrating the distribution of coverage probability differences (ΔP_c) for Rician and Nakagami fading models relative to Rayleigh; the red line marks the median (ΔP_c).

Table 3.2: Overview of Reported Rician K-factor Values in mmWave Literature

Environment	Freq. (GHz)	Scenario	K-factor (dB)	Ref.
Indoor Office	26, 28, 33, 38	LOS	- 1.87 to 1.27	[194]
Indoor Office	26, 28, 33, 38	Obstructed LOS	- 3.79 to -2.31	[194]
Indoor Lab	25-40	LOS	0.48 to 3.43	[192]
Indoor Lab	25-40	NLOS	- 5.54 to - 0.56	[192]
Indoor Factory	4.9, 28	LOS	5.1 to 5.8	[195]
Open Office	28	LOS	up to 6.15	[193]

different fading models under LOS conditions with $\alpha_L = 2$. The system parameters are consistent with those used in Figure 3.6: $C_L = -60$ dB, $P_t = 30$ dBm, BS beamwidth $\eta_b = 30°$, $\lambda_b = 50$ BS/km^2, and BS information parameter $\mu_b = 0.5$. The corresponding boxplots in Figures 3.14-(b) and 3.15-(b) illustrate the distribution of the coverage probability differences (ΔP_c) between the Rician and Nakagami fading models and the Rayleigh baseline.

Under LOS conditions, Rayleigh fading tends to have a slightly lower coverage probability compared to the Rician and Nakagami models; however, the performance gap is minimal. This observation is supported by the boxplots in Figures 3.14-(b) and 3.15-(b) respectively, where the median difference ΔP_c for Rician fading is close to zero, indicating a negligible deviation from Rayleigh. Similarly, for Nakagami fading, the median ΔP_c is slightly higher than that for Rician fading but remains very close to zero, indicating only a minor improvement relative to Rayleigh.

For the NLOS scenario, Figure 3.16 illustrates the downlink coverage probability P_c with $\alpha_N = 4$. The simulation setup mirrors that of Figure 3.10, with considering BS information parameter of $\mu_b = 0.5$. For fading models, a Rician K-factor of -5 dB, and the Nakagami parameter is set to $M_N = 2$.

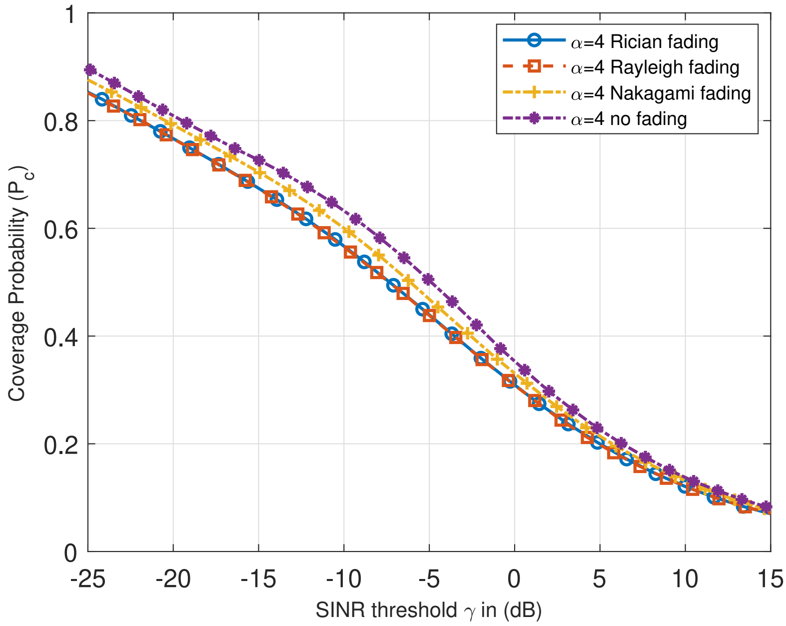

Figure 3.16: Comparison of downlink coverage probability under NLOS conditions ($\alpha_N = 4$) for different fading models: Rayleigh, Rician ($K = -5$ dB), Nakagami-m ($M_N = 2$), and no fading scenario, based on Monte Carlo simulation.

The results in Figure 3.16 demonstrate that the coverage probability for the Rician fading model closely matches that of the Rayleigh fading, indicating a minimal deviation. The Nakagami fading model yields a slightly higher coverage probability, with only minor differences compared to Rayleigh.

From the simulation results, Rayleigh fading slightly underestimates coverage probability compared to more general fading models such as Rician and Nakagami, providing a conservative lower bound while enabling tractable analysis of the LOS and NLOS scenarios considered in this work. Table 3.2 presents typical Rician K-factors in mmWave environments, and even under extreme K-factor conditions, deviations from the Rayleigh baseline remain small, confirming that the main performance trends are preserved for the scenarios analyzed.

3.5 Concluding Remarks

This chapter presents an analysis of downlink coverage probability in 6G mmWave networks using a stochastic geometry framework. The study evaluates the impact of beam alignment accuracy and beamwidth configurations under various propagation conditions, characterized by path loss exponents $\alpha = 4$ for dense urban environments and $\alpha = 2$ for less obstructed areas.

A key finding is that the coverage probability is highly sensitive to the availability of alignment information at the serving base station. In scenarios with complete alignment information, the coverage probability is significantly improved compared to situations with partial or no alignment knowledge, across both path loss conditions.

Additionally, our analysis reveals a clear relationship between coverage probability and the availability of alignment information for different antenna beamwidths. When alignment information is limited, wide beamwidths result in substantially lower coverage. As alignment knowledge increases, the coverage probability for wide beamwidths improves, but the enhancement tends to plateau after reaching a certain threshold of alignment information. In contrast, medium beamwidths consistently outperform both wider and narrower beams, especially when alignment information is partially available. Narrow beamwidths deliver optimal performance when alignment information is nearly perfect. These results emphasize the critical role of selecting the appropriate beamwidth according to the level of available alignment information.

In addition, Rayleigh fading provides a conservative lower bound and a mathematically tractable approach for LOS/NLOS mmWave analysis within the scenarios considered in this study.

Chapter 4

Coverage Analysis with Directional User

4.1 Introduction

This chapter extends the probabilistic beam alignment error framework introduced in Chapter 3 to scenarios in which the user is equipped with a directional antenna. The main objective is to analyze the downlink coverage probability under directional reception and to investigate how the availability of beam alignment information at the serving base station affects coverage performance. Stochastic geometry is used to derive analytical expressions for the downlink coverage probability, which are validated through Monte Carlo simulations. The analysis provides insights into the trade-offs between base station beamwidth, alignment information availability, and coverage, offering a foundation for performance analysis and system design decisions in environments where directional knowledge is limited or costly.

The remainder of this chapter is organized as follows. Section 4.2 describes the system model and methodology. Section 4.3 derives the analytical expressions for downlink coverage probability, Section 4.4 presents simulation results and discussion, and Section 4.5 summarizes key findings.

4.2 System Model and Methodology

In this chapter, the system model is the same as the framework described in Chapter 3. The only modification is that the user is assumed to have a directional antenna, while keeping the same antenna model as in Chapter 3. Figure 4.1 illustrates the system model.

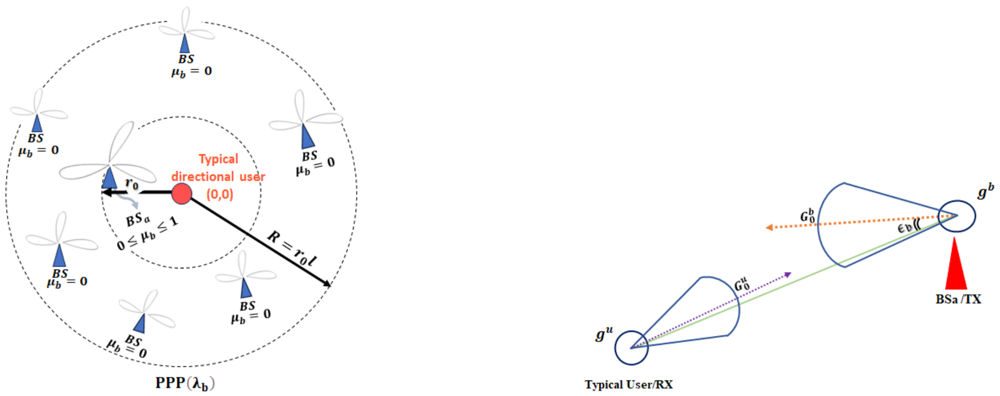

(a) System model (b) Directional Antenna

Figure 4.1: System model and downlink transmission scenario. (a) Overall network layout of a mmWave network with PPP distributed BSs and a typical user at the origin. The nearest BS, BS_a, is at distance r_o and has alignment information parameter $0 \le \mu_b \le 1$, while the interfering BSs with $\mu_b = 0$ occupy the ring between r_o and R; (b) A zoom on the directional downlink, showing beam misalignment with error ϵ_b. The main-lobe gains are G_o^b and G_o^u, and the side-lobe gains are g^b and g^u.

4.3 Coverage Probability

Coverage probability is a key performance metric in mmWave cellular networks. It is defined as the probability that the SINR received by a typical user exceeds a certain threshold [6], and is mathematically expressed as: $P_c(\gamma) = \mathbb{P}[SINR \geq \gamma]$ [16, 19]. In this section, we analyze the downlink SINR experienced by a typical user located at the origin, while accounting for the effects of beam alignment error. We first present a generalized framework that incorporates alignment information at both the BS, (denoted by μ_b) and the typical user (μ_u), capturing varying levels of alignment knowledge or uncertainty at each end of the communication link. Within the scope of this thesis, the alignment information parameter is treated as an abstract parameter within the model, as defined in Section 3.2.4. In practical systems, this parameter can be associated with physical measurements such as beam training, pilot-based estimation, or user location information. However, obtaining accurate directional information is inherently constrained by finite pilot resources, limited feedback resolution, channel variations, and user mobility, which degrade the reliability of the estimated alignment direction. In addition, achieving higher estimation accuracy requires multiple training beams, repeated pilot transmissions, and feedback exchange, which introduce additional signaling and computational burden. This, in turn, consumes network resources and reduces the resources available for data transmission, making precise directional information costly in practical systems. Subsequently, we narrow our focus to specific case studies that examine the availability of alignment information exclusively at the serving BS, and derive coverage probability expressions for different path loss exponents.

4.3.1 General Framework: Incorporating Alignment Information

This subsection introduces a framework that accounts for the beam alignment information available at the serving BS and the typical user. The parameters μ_b and μ_u represent the levels of alignment information at the BS and the user, respectively, with values ranging from 0 to 1. Specifically, $\mu_b = 1$ and $\mu_u = 1$ indicate that the perfect alignment information is available at both the BS and the user, while the values between 0 and 1 correspond to partial alignment information, and $\mu_b = 0$ and $\mu_u = 0$ represent the absence of alignment information at either end. A general expression for SINR is derived, incorporating the alignment parameters of both sides of the communication link. The resulting SINR at the typical receiver is expressed as follows:

$$\text{SINR} = \frac{P h_o G^{ab}_{\mu_b \neq 0}(\epsilon_b) G^{au}_{\mu_u \neq 0}(\epsilon_u)\ C r_o^{-\alpha}}{\sigma_n^2 + I_n} \tag{4.1}$$

In (4.1), h_o denotes the channel gain associated with the serving BS, and r_o represents a random variable that characterizes the distance between the typical user and the nearest BS, as detailed in Section 3.2.2. The parameters C and α correspond to the path loss intercept and the path loss exponent, respectively. Furthermore, ϵ_b and ϵ_u are random variables that capture alignment errors at the serving BS and the typical user, respectively. The terms σ_n^2 and I_n represent the noise power and the aggregate interference, respectively. It is assumed that all BSs transmit at the same power level, denoted by P. The aggregate interference encountered by a typical user is defined as follows. Interfering BSs are assumed to have no alignment information with respect to the typical user (i.e., $\mu_b = 0$ and $\mu_u = 0$ for interfering links), and no coordination is considered. These assumptions simplify interference modeling and allow for a focused analysis of the performance impact of alignment information at the serving BS. The current analysis considers a single-operator setting. Scenarios involving inter-operator coordination and the exchange of partial or varying levels of alignment information are left for future work.

$$I_n = \sum_{\substack{i\in\Phi \\ (r_o,R)}} P\ h_i\ G^{Ib}_{i(\mu_b=0)}(\epsilon_b)\ G^{Iu}_{(\mu_u=0)}(\epsilon_u)\ Cr_i^{-\alpha} \tag{4.2}$$

The gain expressions in (4.1) and (4.2) can be stated as follows: G^{ab} and G^{au} represent the gain of the serving BS at the typical user and the gain of the typical user at the serving BS user when $\mu_b \neq 0$. G^{Ib} and G^{Iu} represent the gain of the interfering BS at the typical user, and the gain of the typical user at the interfering BS when $\mu_b = 0$. Furthermore, the interfering BSs are located at distances r_i from the typical user. These BSs are characterized by the power fading random variables h_i, and all of them are positioned beyond the boundary defined by the circular region r_o; see Figure 4.1. The coverage probability P_c can be expressed as follows:

$$\begin{aligned} P_c =& \mathbb{P}\left[\text{SINR} > \gamma\right] = \mathbb{P}\left[\frac{h_o G^{ab}_{\mu_b\neq 0}(\epsilon_b) G^{au}_{\mu_u\neq 0}(\epsilon_u)\ Cr_o^{-\alpha}}{\sigma^2_{\bar{n}} + I_{\bar{n}}} > \gamma\right] \\ =& \mathbb{P}\left[h_o > \rho\left(\sigma^2_{\bar{n}} + I_{\bar{n}}\right)\right], \end{aligned} \tag{4.3}$$

here, $I_{\bar{n}} = \frac{I_n}{P}$, $\sigma^2_{\bar{n}} = \frac{\sigma^2_n}{P}$, represent the normalized aggregate interference and the normalized noise power, respectively. The parameter ρ is defined as: $\frac{\gamma\ r_o^{\alpha}}{G^{ab}G^{au}C}$. The coverage probability P_c is expressed as:

$$P_c = \mathbb{E}_{G^{ab},G^{au},r_o,I_{\bar{n}}}\left[e^{-\rho\sigma_{\bar{n}}^2} \cdot e^{-\rho I_{\bar{n}}}\right], \tag{4.4}$$

The formulation given in (4.4) arises from the small-scale Rayleigh fading, represented as h_o, which follows an exponential distribution, $h_o \sim \exp(1)$ [188]. The general form of our model, incorporating alignment information at both the serving BS μ_b and the typical user μ_u, is presented below.

$$\begin{aligned} P_c = &\int_{-b(\mu_u)}^{b(\mu_u)} \int_{-b(\mu_b)}^{b(\mu_b)} \int_0^{\infty} e^{-\rho\sigma_{\bar{n}}^2} \\ &\times \mathbb{E}_{\Phi,G^{Ib},G^{Iu},h}\left[e^{-\rho\sum_{i\in\Phi} h_i G^{Ib}_{(\mu_b=0)} G^{Iu}_{(\mu_u=0)} C r_i^{-\alpha}}\right] \\ &\times f_{R_o}(r_o) \cdot f_{\epsilon_b}(\epsilon_b) \cdot f_{\epsilon_u}(\epsilon_u)\, dr_o\ d\epsilon_b\ d\epsilon_u \end{aligned} \tag{4.5}$$

The expression in (4.5) is applicable to two distinct user-side antenna configurations: one where the typical user employs an omni- antenna and the other where a directional antenna is used. In the next step, we focus on solving the expectation term in (4.5). This can be rewritten as:

$$\mathbb{E}_{\Phi,G^{Ib},G^{Iu},h}\left[\prod_{i\in\Phi} e^{-\rho h_i G^{Ib}_{(\mu_b=0)} G^{Iu}_{(\mu_u=0)} C {r_i}^{-\alpha}}\right],$$

we apply the following steps to simplify this expectation term:

$$\overset{(a)}{=} \exp\left(\int_{(r_o,R)} \mathbb{E}_{G^{Ib},G^{Iu},h}[e^{-\rho h G^{Ib} G^{Iu} C r^{-\alpha}} - 1] d\Lambda(\bar{r})\right),$$

$$\overset{(b)}{=} \exp\left(\int_{(r_o,R)} \mathbb{E}_{G^{Ib},G^{Iu}}\left[\frac{-\rho G^{Ib} G^{Iu} C r^{-\alpha}}{1+\rho G^{Ib} G^{Iu} C r^{-\alpha}}\right] d\Lambda(\bar{r})\right). \tag{4.6}$$

Step (a) results from applying the Probability Generating Functional (PGFL) of the point process [183], while step (b) follows from the fact that small-scale fading h follows an exponential distribution $h \sim \exp(1)$. In the following subsections, we examine specific scenarios that allow significant simplifications, resulting in more tractable and intuitive expressions for the coverage probability.

4.3.2 Case Study: Impact of Base Station Information

For analytical tractability and without loss of generality, we assume that the serving BS, exclusively performs the beamforming process. In this context, we specifically consider the beam alignment information (μ_b) available at serving BS. The analysis adopts the perspective of a typical user equipped with a directional antenna. We assume that this typical user, with prior knowledge of the serving BS's location, aligns its directional antenna such that the main lobe is directed toward the serving BS, ensuring the associated gain of the typical user $G^{au} = G^u_o$. Given that G^{Ib} and G^{Iu} are evaluated at $\mu_b = 0$ and $\mu_u = 0$, the alignment error boundary and the PDF of the alignment error are given by:

$$b(\mu_b = 0) = \pi, \tag{4.7a}$$

$$\lim_{\mu_b \to 0} f_{\epsilon_b}(\epsilon_b) = \frac{1}{2\pi}, \tag{4.7b}$$

further as we are considering $G^{au} = G^u_o$, (4.6) can be reformulated as:

$$\exp\left(\int_{(r_o,R)} \mathbb{E}_{G^{Ib}_{\mu=0},G^{Iu}_{\mu=0}} \left[\frac{-\rho\, G^{Ib}G^{Iu}Cr^{-\alpha}}{1+\rho\, G^{Ib}G^{Iu}Cr^{-\alpha}}\right] d\Lambda(\bar{r})\right), \tag{4.8}$$

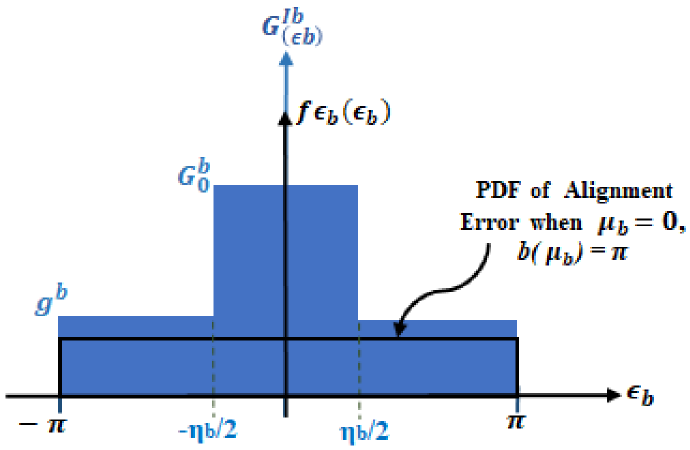

Figure 4.2: Illustration of the PDF of alignment error $f_{\epsilon_b}(\epsilon_b)$ for interfering BSs when the information parameter $\mu_b = 0$, where the error follows a uniform distribution with PDF value $f_{\epsilon_b}(\epsilon_b) = \frac{1}{2\pi}$. The figure also includes the flat-top antenna model, showing the main lobe gain $G^b_o = G^{Ib}_o$ and side lobe gain $g^b = g^{Ib}$ for the interfering BS gain G^{Ib}. This combined representation highlights both the uniform distribution of alignment error and the directional characteristics of the antenna model.

Based on (4.7a) and (4.7b) the PDF of alignment error for interference BSs follows a uniform distribution within the interval $[-\pi, \pi]$, as illustrated in Figure 4.2. The expression in (4.8) can be further simplified.

$$\exp\left(\frac{\eta_b\eta_u}{4\pi^2}\int_{r_o}^{R}\left(\frac{-\rho\; G^b_o G^u_o C r^{-\alpha}}{1+\rho\; G^b_o G^u_o C r^{-\alpha}}\right)2\pi\lambda r dr + \right.$$
$$\frac{\eta_b}{2\pi}\left(1-\frac{\eta_u}{2\pi}\right)\int_{r_o}^{R}\left(\frac{-\rho\; G^b_o g^u C r^{-\alpha}}{1+\rho\; G^b_o g^u C r^{-\alpha}}\right)2\pi\lambda r dr +$$
$$\left(1-\frac{\eta_b}{2\pi}\right)\frac{\eta_u}{2\pi}\int_{r_o}^{R}\left(\frac{-\rho g^b G^u_o C r^{-\alpha}}{1+\rho\; g^b G^u_o C r^{-\alpha}}\right)2\pi\lambda r dr +$$
$$\left.(1-\frac{\eta_b}{2\pi})(1-\frac{\eta_u}{2\pi})\int_{r_o}^{R}\left(\frac{-\rho\; g^b g^u C r^{-\alpha}}{1+\rho\; g^b g^u C r^{-\alpha}}\right)2\pi\lambda r dr\right).$$

In this context, $g^b = g^{Ib}$, and $g^u = g^{Iu}$ represent the side lobe gains of the interfering BSs and the typical user, respectively, while η_b and η_u correspond to the mainlobe beamwidths of a BS and the typical user, respectively. Let us now define the first term of the integral as B. Using hypergeometric functions, we can express the first term of the integral as:

$$B = \pi\lambda R^2 \ {}_2F_1\left(\frac{-G^{ab}}{G_o^b\gamma}\left(\frac{R}{r_o}\right)^\alpha\right) - \pi\lambda r_o^2 \ {}_2F_1\left(\frac{-G^{ab}}{G_o^b\gamma}\right) \tag{4.9}$$

for the second term of the integral, we define it as D:

$$D = \pi\lambda R^2 \ {}_2F_1\left(\frac{-G^{ab}}{g^b\gamma}\left(\frac{R}{r_o}\right)^\alpha\right) - \pi\lambda r_o^2 \ {}_2F_1\left(\frac{-G^{ab}}{g^b\gamma}\right) \tag{4.10}$$

similarly, we define the third term of the integral as H:

$$H = \pi\lambda R^2 \ {}_2F_1\left(\frac{-g^b}{G_o^u\gamma}\left(\frac{R}{r_o}\right)^\alpha\right) - \pi\lambda r_o^2 \ {}_2F_1\left(\frac{-g^b}{G_o^u\gamma}\right) \tag{4.11}$$

finally, we define the fourth term of the integral as L:

$$L = \pi\lambda R^2 \ {}_2F_1\left(\frac{-g^b}{g^u\gamma}\left(\frac{R}{r_o}\right)^\alpha\right) - \pi\lambda r_o^2 \ {}_2F_1\left(\frac{-g^b}{g^u\gamma}\right) \tag{4.12}$$

here, ${}_2F_1(\cdot)$ represents the hypergeometric function, and we utilize the form ${}_2F_1(\cdot) = {}_2F_1\left(1, \frac{2}{\alpha}; \frac{2}{\alpha} + 1; (\cdot)\right)$. Using the expressions for B, D, H, and L, and substituting them into (4.5), we derive the following expression:

$$P_c = \int_0^{\infty} \int_{-b(\mu_b)}^{b(\mu_b)} \exp -\left(\rho\, \sigma_{\bar{n}}^2 + \frac{\eta_u \eta_b}{4\pi^2} B + \frac{\eta_u}{2\pi}\left(1 - \frac{\eta_b}{2\pi}\right) D \right.$$
$$\left. + \frac{\eta_b}{2\pi}\left(1 - \frac{\eta_u}{2\pi}\right) H + \left(1 - \frac{\eta_b}{2\pi}\right)\left(1 - \frac{\eta_u}{2\pi}\right) L + \pi\lambda r_o^2\right)$$
$$2\pi\lambda r_o \frac{\mu_b\, e^{\frac{-\mu_b^2 \epsilon_b^2}{2\zeta_b^2}}}{\sqrt{2\pi}\, \zeta_b \,\mathrm{erf}\left(\frac{\mu_b b(\mu_b)}{\sqrt{2}\zeta_b}\right)} d\epsilon_b dr_o \,. \tag{4.13}$$

The expression in (4.13) defines the probability of downlink coverage P_c, considering the alignment information, μ_b, at the serving BS. It applies to scenarios where the typical user employs a directional antenna and is valid for the path loss exponent values of $\alpha = 4$ and $\alpha = 2$. In the following, explicit solutions are derived for these specific path-loss exponents.

4.3.2.1 Path Loss Exponent 4

In this first specific case, we consider a path loss exponent set to $\alpha = 4$. To facilitate a tractable mathematical analysis without loss of generality, we assume that the radius R of the system model is given by $R = lr_o$, where $l > 1$. By solving (4.9), (4.10), (4.11), and (4.12) for $\alpha = 4$, we can express these terms as follows:

$$B^{(\alpha=4)} = \sqrt{\frac{\gamma G_o^b}{G^{ab}}}\left(\tan^{-1}\left(\sqrt{\frac{G^{ab}}{G_o^b \gamma}} l^2\right) - \tan^{-1}\left(\sqrt{\frac{G^{ab}}{G_o^b \gamma}}\right)\right) \tag{4.14}$$

$$D^{(\alpha=4)} = \sqrt{\frac{\gamma g^b}{G^{ab}}}\left(\tan^{-1}\left(\sqrt{\frac{G^{ab}}{g^b\gamma}}l^2\right) - \tan^{-1}\left(\sqrt{\frac{G^{ab}}{g^b\gamma}}\right)\right) \tag{4.15}$$

$$H^{(\alpha=4)} = \sqrt{\frac{g^u G_o^b\gamma}{G^{ab}G_o^u}}\left(\tan^{-1}\left(\sqrt{\frac{G^{ab}G_o^u}{g^u G_o^b\gamma}}l^2\right) - \tan^{-1}\left(\sqrt{\frac{G^{ab}G_o^u}{g^u G_o^b\gamma}}\right)\right) \tag{4.16}$$

$$L^{(\alpha=4)} = \sqrt{\frac{g^u g^b\gamma}{G^{ab}G_o^u}}\left(\tan^{-1}\left(\sqrt{\frac{G^{ab}G_o^u}{g^u g^b\gamma}}l^2\right) - \tan^{-1}\left(\sqrt{\frac{G^{ab}G_o^u}{g^u g^b\gamma}}\right)\right) \tag{4.17}$$

substituting (4.14), (4.15), (4.16), and (4.17) into (4.13), and solving for $\alpha = 4$ yields:-

$$\begin{aligned}
P_c = {} & \frac{\pi^{3/2}\lambda\sqrt{G_o^b G_o^u CP}}{2\sigma_n\sqrt{\gamma}} \cdot e^{\frac{\pi^2\lambda^2 G_o^b G_o^u CP}{4\gamma\sigma_n^2} K_o^2} \\
& \text{erfc}\left[\frac{\pi\lambda\sqrt{G_o^b G_o^u CP}}{2\sigma_n\sqrt{\gamma}} K_o\right] \Delta^b \\
& + \frac{\pi^{3/2}\lambda\sqrt{g^b G_o^u CP}}{2\sigma_n\sqrt{\gamma}} \, e^{\frac{\pi^2\lambda^2 g^b G_o^u CP}{4\gamma\sigma_n^2} K_g^2} \\
& \text{erfc}\left[\frac{\pi\lambda\sqrt{g^b G_o^u CP}}{2\sigma_n\sqrt{\gamma}} K_g\right] \quad (1-\Delta^b),
\end{aligned} \tag{4.18}$$

where:

$$\begin{aligned}
K_o = {} & 1 + \frac{\eta_u\eta_b}{4\pi^2}\cdot B_o + \frac{\eta_u}{2\pi}\left(1-\frac{\eta_b}{2\pi}\right) D_o \\
& + \frac{\eta_b}{2\pi}\left(1-\frac{\eta_u}{2\pi}\right) H_o + \left(1-\frac{\eta_b}{2\pi}\right)\left(1-\frac{\eta_u}{2\pi}\right) L_o
\end{aligned}$$

$$K_g = 1 + \frac{\eta_u \eta_b}{4\pi^2} \cdot B_g + \frac{\eta_u}{2\pi}\left(1 - \frac{\eta_b}{2\pi}\right) D_g + \frac{\eta_b}{2\pi}\left(1 - \frac{\eta_u}{2\pi}\right) H_g + \left(1 - \frac{\eta_b}{2\pi}\right)\left(1 - \frac{\eta_u}{2\pi}\right) L_g$$

$$B_o = \sqrt{\gamma}\left(\tan^{-1}\left(\frac{l^2}{\sqrt{\gamma}}\right) - \tan^{-1}\left(\frac{1}{\sqrt{\gamma}}\right)\right)$$

$$B_g = \sqrt{\frac{\gamma G_o^b}{g^b}}\left(\tan^{-1}\left(\sqrt{\frac{g^b}{G_o^b \gamma}} l^2\right) - \tan^{-1}\left(\sqrt{\frac{g^b}{G_o^b \gamma}}\right)\right)$$

$$D_o = \sqrt{\frac{\gamma g^b}{G_o^b}}\left(\tan^{-1}\left(\sqrt{\frac{G_o^b}{g^b \gamma}} l^2\right) - \tan^{-1}\left(\sqrt{\frac{G_o^b}{g^b \gamma}}\right)\right)$$

$$D_g = \sqrt{\gamma}\left(\tan^{-1}\left(\frac{l^2}{\sqrt{\gamma}}\right) - \tan^{-1}\left(\frac{1}{\sqrt{\gamma}}\right)\right)$$

$$H_o = \sqrt{\frac{\gamma g^u}{G_o^u}}\left(\tan^{-1}\left(\sqrt{\frac{G_o^u}{g^u \gamma}} l^2\right) - \tan^{-1}\left(\sqrt{\frac{G_o^u}{g^u \gamma}}\right)\right)$$

$$H_g = \sqrt{\frac{\gamma G_o^b g^u}{G_o^u g^b}}\left(\tan^{-1}\left(\sqrt{\frac{G_o^u g^b}{G_o^b g^u \gamma}} l^2\right) - \tan^{-1}\left(\sqrt{\frac{G_o^u g^b}{G_o^b g^u \gamma}}\right)\right)$$

$$L_o = \sqrt{\frac{\gamma g^b g^u}{G_o^b G_o^u}}\left(\tan^{-1}\left(\sqrt{\frac{G_o^b G_o^u}{g^b g^u \gamma}} l^2\right) - \tan^{-1}\left(\sqrt{\frac{G_o^b G_o^u}{g^b g^u \gamma}}\right)\right)$$

$$L_g = \sqrt{\frac{\gamma g^u}{G_o^u}}\left(\tan^{-1}\left(\sqrt{\frac{G_o^u}{g^u \gamma}} l^2\right) - \tan^{-1}\left(\sqrt{\frac{G_o^u}{g^u \gamma}}\right)\right)$$

$$\Delta^b = \begin{cases} \frac{\mathrm{erf}\left(\frac{\mu_b \eta_b}{2\sqrt{2}\zeta_b}\right)}{\mathrm{erf}\left(\frac{\mu_b b(\mu_b)}{\sqrt{2}\zeta_b}\right)} & \text{if } b(\mu_b) \geq \frac{\eta_b}{2} \\ 1 & \text{if } b(\mu_b) < \frac{\eta_b}{2} \end{cases} \tag{4.19}$$

As discussed in Section 3.2.3, we defined $\delta_b = \eta_b/2$, then $b(\mu_b) \geq \eta_b/2$.

$$\Rightarrow \Delta^b = \frac{\mathrm{erf}\left(\frac{\mu_b \eta_b}{2\sqrt{2}\zeta_b}\right)}{\mathrm{erf}\left(\frac{\mu_b b(\mu_b)}{\sqrt{2}\zeta_b}\right)}$$

The expression for Δ^b represents the effect of alignment error on the coverage probability P_c, illustrating how the system performance is sensitive to variations in alignment information μ_b. Furthermore, this term captures the combined influence of the alignment information level μ_b, the truncation boundary $b(\mu_b)$, the beamwidth η_b, and the inefficiency factor ζ_b on the system's performance. The expression in (4.18) defines the downlink coverage probability P_c for $\alpha = 4$. Extending this analysis to $\alpha = 2$ allows evaluation of how different propagation conditions affect the coverage probability.

4.3.2.2 Path Loss Exponent 2

In the second case, we examine the scenario in which the path loss exponent is set to $\alpha = 2$. To maintain a tractable mathematical analysis without loss of generality, we again assume that the radius R of the system model is given by $R = lr_o$, where $l > 1$ (as illustrated in Figure 4.1). By solving equations (4.9), (4.10), (4.11), and (4.12) under these conditions, we can express the terms as follows:

$$B^{(\alpha=2)} = \pi \lambda r_o^2 \left(\frac{\gamma \; G_o^b}{G^{ab}} \right) \ln \left(\frac{\frac{\gamma \; G_o^b}{G^{ab}} + l^2}{\frac{\gamma \; G_o^b}{G^{ab}} + 1} \right) \tag{4.20}$$

$$D^{(\alpha=2)} = \pi \lambda r_o^2 \left(\frac{\gamma \; g^b}{G^{ab}} \right) \ln \left(\frac{\frac{\gamma \; g^b}{G^{ab}} + l^2}{\frac{\gamma \; g^b}{G^{ab}} + 1} \right) \tag{4.21}$$

$$H^{(\alpha=2)} = \pi \lambda r_o \left(\frac{\gamma G_o^b g^u}{G^{ab} G_o^u} \right) \ln \left(\frac{\frac{\gamma G_o^b g^u}{G^{ab} G_o^u} + l^2}{\frac{\gamma G_o^b g^u}{G^{ab} G_o^u} + 1} \right) \tag{4.22}$$

$$L^{(\alpha=2)} = \pi \lambda r_o \left(\frac{\gamma g^b g^u}{G^{ab} G_o^u} \right) \ln \left(\frac{\frac{\gamma g^b g^u}{G^{ab} G_o^u} + l^2}{\frac{\gamma g^b g^u}{G^{ab} G_o^u} + 1} \right) \tag{4.23}$$

By substituting (4.20), (4.21), (4.22), and (4.23) into (4.13) and solving the integrals for $\alpha = 2$ (see Figure 4.3), we obtain the expression for P_c, given in (4.24).

$$\tilde{B}_o = \gamma \ln \left(\frac{\gamma + l^2}{\gamma + 1} \right), \qquad \tilde{B}_g = \frac{G_o^b \gamma}{g^b} \ln \left(\frac{\frac{G_o^b \gamma}{g^b} + l^2}{\frac{G_o^b \gamma}{g^b} + 1} \right),$$

$$\tilde{D}_o = \frac{g^b \gamma}{G_o^b} \ln \left(\frac{\frac{g^b \gamma}{G_o^b} + l^2}{\frac{g^b \gamma}{G_o^b} + 1} \right), \qquad \tilde{D}_g = \gamma \ln \left(\frac{\gamma + l^2}{\gamma + 1} \right),$$

$$\tilde{H}_o = \left(\frac{g^u \gamma}{G_o^u} \right) \ln \left(\frac{\frac{g^u \gamma}{G_o^u} + l^2}{\frac{g^u \gamma}{G_o^u} + 1} \right), \quad \tilde{H}_g = \left(\frac{g^u G_o^b \gamma}{g^b G_o^u} \right) \ln \left(\frac{\frac{g^u G_o^b \gamma}{g^b G_o^u} + l^2}{\frac{g^u G_o^b \gamma}{g^b G_o^u} + 1} \right),$$

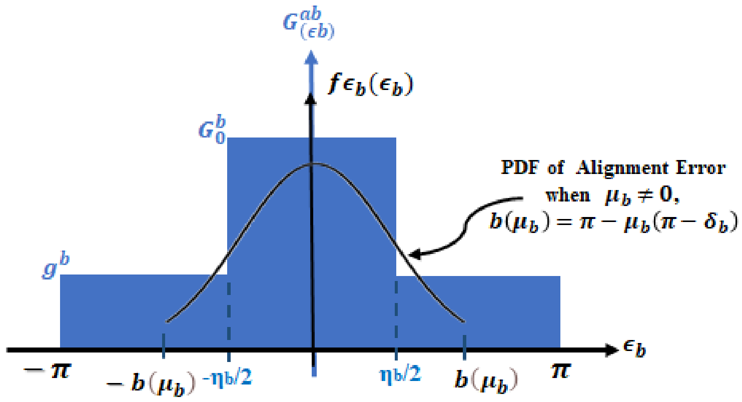

Figure 4.3: Illustration of the PDF of alignment error $f_{\epsilon_b}(\epsilon_b)$ for the serving BS with $\mu_b \neq 0$, where the error follows a truncated Gaussian distribution. The plot highlights the main lobe gain ($G_o^b = G_o^{ab}$) and side lobe gain ($g^b = g^{ab}$) under a flat-top antenna model.

$$P_c = \frac{\Delta^b}{1 + \frac{\gamma\sigma_n^2}{\pi\lambda P C G_o^b G_o^u} + \frac{\eta_b\eta_u}{4\pi^2}\tilde{B}_o + \left(\frac{\eta_u}{2\pi}\right)\left(1-\frac{\eta_b}{2\pi}\right)\tilde{D}_o + \left(\frac{\eta_b}{2\pi}\right)\left(1-\frac{\eta_u}{2\pi}\right)\tilde{H}_o + \left(1-\frac{\eta_b}{2\pi}\right)\left(1-\frac{\eta_u}{2\pi}\right)\tilde{L}_o} + \frac{(1-\Delta^b)}{1 + \frac{\gamma\sigma_n^2}{\pi\lambda P C g^b G_o^u} + \frac{\eta_b\eta_u}{4\pi^2}\tilde{B}_g + \left(\frac{\eta_u}{2\pi}\right)\left(1-\frac{\eta_b}{2\pi}\right)\tilde{D}_g + \left(\frac{\eta_b}{2\pi}\right)\left(1-\frac{\eta_u}{2\pi}\right)\tilde{H}_g + \left(1-\frac{\eta_b}{2\pi}\right)\left(1-\frac{\eta_u}{2\pi}\right)\tilde{L}_g}, \tag{4.24}$$

$$\tilde{L_o} = \left(\frac{g^b g^u \gamma}{G_o^b G_o^u}\right) \ln\left(\frac{\frac{g^b g^u \gamma}{G_o^b G_o^u} + l^2}{\frac{g^b g^u \gamma}{G_o^b G_o^u} + 1}\right), \quad \tilde{L_g} = \left(\frac{g^u \gamma}{G_o^u}\right) \ln\left(\frac{\frac{g^u \gamma}{G_o^u} + l^2}{\frac{g^u \gamma}{G_o^u} + 1}\right).$$

The expression derived in (4.24) for the coverage probability P_c under the path loss exponent $\alpha = 2$.

4.4 Simulation and Discussion Results

This section analyzes the performance of a mmWave network in the presence of beam alignment errors and verifies the precision of our analytical

Table 4.1: Simulation Parameters

Notation	Description	Value	Reference
λ_b	BS density	50/km^2	[18]
g_b	BS antenna gain-sidelobe	-10 (dBi)	–
g_u	User antenna gain-sidelobe	-20 dBi	–
α_L, α_N	LOS and NLOS path loss exponents, respectively	2, 4	[188]
C_L, C_N	LOS and NLOS path loss intercepts, respectively	-60 dB, -70 dB	[188]
f_c	Carrier frequency	28 GHz	[13]
W	Bandwidth	100 MHz	[13]
ζ_b	Antenna system inefficiency factor	0.158	–
l	Positive integer scaling factor ($l > 1$, $R = r_o\, l$)	18	–
σ_n^2	Noise power	- 174 dBm/Hz + 10 $\log_{10}(W)$ + 10 dB	[18]

framework through Monte Carlo simulations. The coverage probability expressions P_c derived in Section 4.3 for NLOS and LOS conditions, given in (4.18) and (4.24), respectively are evaluated under different network configurations. The results examine the impact of the alignment information available at the serving BS, represented by μ_b, the serving BS beamwidth η_b, and the BS density λ_b. Table 4.1 presents the key simulation parameters.

4.4.1 Coverage Analysis

We begin by analyzing network performance in a dense environment under NLOS conditions with $\alpha_N = 4$. Figure 4.4 shows the impact of BS beamwidth η_b on the downlink coverage probability P_c under varying levels of alignment information μ_b (i.e., over the full range $\mu_b \in [0, 1]$), evaluated at a 15 dB SINR threshold, for three different serving BS beamwidths: $\eta_b = 90°$, $30°$,

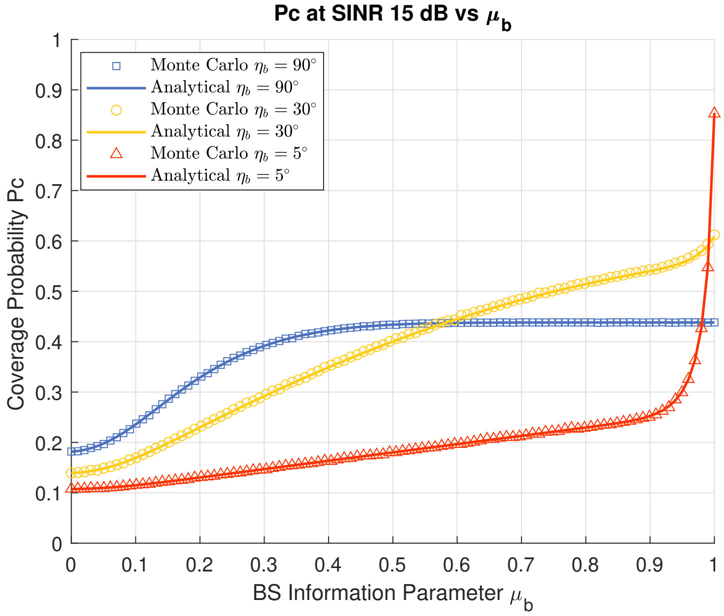

Figure 4.4: Coverage probability P_c (theoretical and Monte Carlo) versus the serving BS alignment information parameter μ_b, for $\alpha_N = 4$ and a SINR threshold of 15 dB. Three BS beamwidths are considered: $\eta_b = 90°$, $30°$, and $5°$. The system parameters: $C_N = -\ 70\,\text{dB}$, $P_t = 40\,\text{dBm}$, user beamwidth $\eta_u = 5°$, BS density $\lambda_b = 50\,\text{BS/km}^2$, and $l = 18$.

and $5°$.

For wide beams $90°$, the coverage probability P_c is relatively low when alignment information is very limited $0 \leq \mu_b \leq 0.1$, increasing substantially as μ_b increases from 0.1 to 0.4. Beyond $\mu_b > 0.4$, the improvement in P_c begins to diminish, stabilizing at approximately 0.44 as μ_b approaches 1. This indicates that for wide beams, alignment information beyond this threshold yields negligible gains, making $\mu_b \approx 0.4$ a practical benchmark for regulatory or deployment decisions regarding wide-beam operation. Medium beams $\eta_b = 30°$ outperform both wide and narrow beams once alignment information exceeds 0.6, with the advantage most pronounced for $(0.6 < \mu_b < 0.98)$. Narrow beams $5°$ surpass others only when alignment information is near perfect ($\mu_b > 0.98$).

The coverage probability for the wide beam configurations ($\eta_b = 90°$ and $30°$) remains below 0.6 over the entire range of $\mu_b \in [0, 1]$. This is mainly attributed to the NLOS propagation environment, characterized by a path loss exponent of $\alpha_N = 4$, which causes significant attenuation of the received signal power. Furthermore, the coverage probability is evaluated at an SINR threshold of 15 dB, which requires a sufficiently strong received signal for successful reception. Although increasing μ_b improves beam alignment and increases the antenna directional gain, the resulting improvement is insufficient to compensate for the severe NLOS attenuation and satisfy the 15 dB SINR requirement. In contrast, the narrow beam configuration ($\eta_b = 5°$) achieves a significantly higher coverage probability (≈ 0.85) under perfect alignment ($\mu_b = 1$) due to its higher antenna gain.

The results in Figure 4.4 show that although wider beamwidths benefit from increased alignment information, their performance gains plateau beyond a certain threshold. In contrast, medium beamwidths benefit more from increased information compared to wider beamwidths. Therefore, medium beamwidths offer a tradeoff: they leverage improved alignment knowledge without requiring the precision needed by narrow beamwidths, while providing better performance than both wider and narrower beamwidths under intermediate levels of alignment information. Narrow beamwidths excel when alignment information is nearly perfect. These observations highlight the critical role of beamwidth selection in relation to the level of alignment information availability in the mmWave systems. From a regulatory perspective, these findings support defining minimum alignment information thresholds

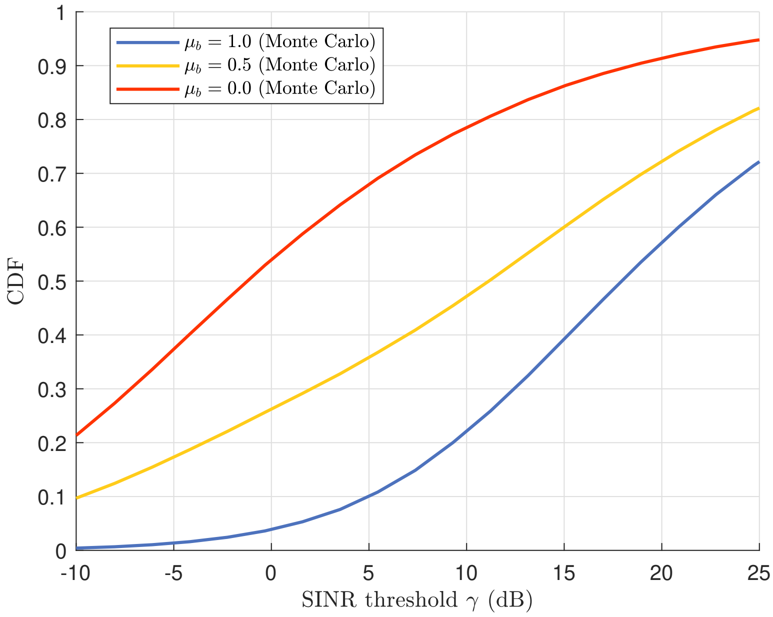

Figure 4.5: Empirical CDF (Monte Carlo) versus SINR threshold γ for $\alpha_N = 4$. The system parameters are: $C_L = -70\,\text{dB}$, $P_t = 40\,\text{dBm}$, $\eta_b = 30°$, $\eta_u = 5°$, $\lambda_b = 50\,\text{BS/km}^2$, and $l = 18$.

for authorizing narrow beam deployments, recommending medium beams under partial alignment information, and permitting wide beams in scenarios with low alignment information, where stable coverage can be maintained despite lower peak performance. Incorporating such alignment-aware guidelines enables regulators to define enforceable deployment rules that maintain adequate coverage and improve spectrum utilization efficiency in mmWave networks.

To further analyze system performance, Figure 4.5 illustrates the empirical Cumulative Distribution Function (CDF) of the SINR for a typical user located at the origin in a stochastic geometry-based under different values of the BS information parameter μ_b. The results are obtained using Monte Carlo simulations, where base stations are distributed according to a homogeneous PPP, as discussed in the system model Section 4.2 and shown in Figure. 4.1.

It can be observed that increasing μ_b shifts the CDF towards lower values, indicating an improvement in the SINR distribution. To further interpret the results, consider a SINR threshold of 10 dB. The CDF values at this threshold are 0.79 for $\mu_b = 0$, 0.49 for $\mu_b = 0.5$, and 0.24 for $\mu_b = 1$. This indicates that under no alignment information ($\mu_b = 0$), there is approximately 80% probability that the SINR of the typical user falls below this threshold, while the intermediate case ($\mu_b = 0.5$) shows a moderate reduction to about 50%. In contrast, when perfect alignment information is available ($\mu_b = 1$), this probability decreases to approximately 25%, demonstrating a significant improvement in the SINR distribution. The results confirm that increasing μ_b consistently enhances system performance by reducing the probability of low-SINR events.

Figure 4.6 extends the analysis of Figure 4.4 by presenting the probability of coverage P_c as a function of the SINR threshold for three BS beamwidths ($\eta_b = 90°$, $30°$, and $\eta_b = 5°$ under three levels of alignment information: no information, partial, and perfect information. For $\eta_b = 90°$ (Figure 4.6-(a)), the performance with partial information ($\mu_b = 0.5$) closely matches that with perfect information ($\mu_b = 1$), both significantly outperforming the no-information case ($\mu_b = 0$). Reducing the beamwidth to $30°$ (Figure 4.6-(b)) leads to higher overall coverage compared to $90°$, although the performance gap between the perfect and partial alignment information becomes more pronounced. With the narrowest beamwidth, $\eta_b = 5°$ (Figure 4.6-(c)), P_c reaches its maximum only with perfect alignment information, while even

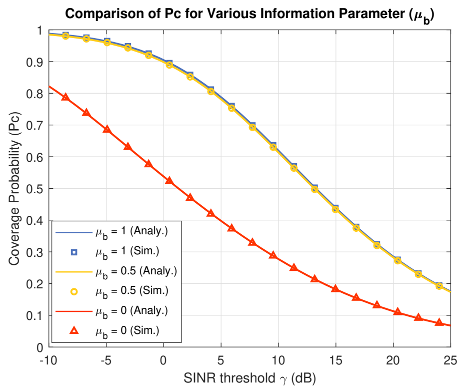

(a) BS beamwidth, $\eta_b = 90°$

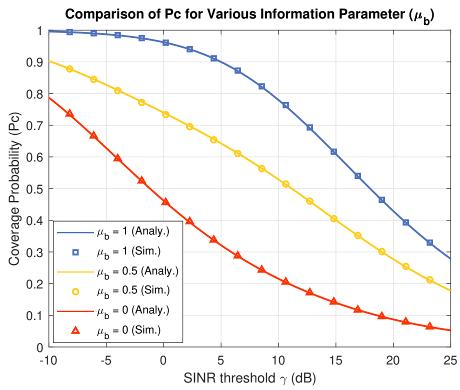

(b) BS beamwidth, $\eta_b = 30°$

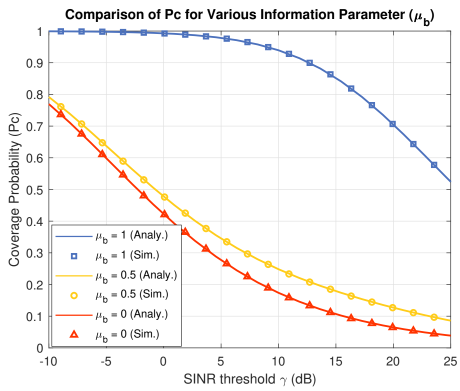

(c)BS beamwidth, $\eta_b = 5°$

Figure 4.6: Comparison of coverage probability P_c (theory and Monte Carlo) vs. SINR for different BS beamwidths, η_b, with parameters: $\alpha_N = 4$, $C_N = -70\,\text{dB}$, $P_t = 40\,\text{dBm}$, $\eta_u = 5°$, $\lambda_b = 50\,\text{km}^{-2}$, and $l = 18$.

partial alignment information leads to a significant performance drop. These results suggest different regulatory considerations based on the availability of alignment information and beamwidth configurations. Regulatory frameworks incorporating alignment information thresholds can enable adaptive spectrum management that balances coverage and interference in mmWave networks.

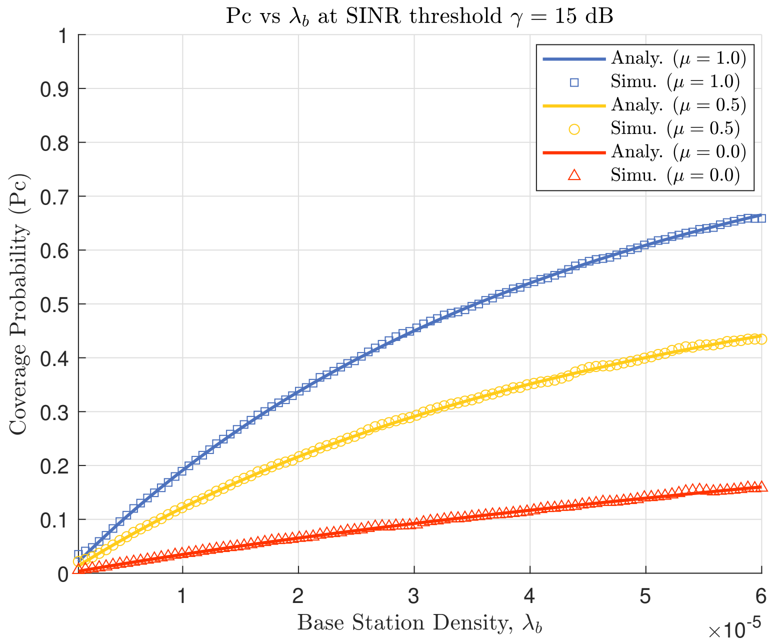

Figure 4.7: Coverage probability P_c at SINR threshold of 15 dB vs. BS density λ_b for BS information parameters $\mu = \{1, 0.5, 0\}$. Theoretical and Monte Carlo results are shown with parameters: $\alpha_N = 4$, $C_N = -70\,$dB, $P_t = 40\,$dBm, $\eta_b = 30°$, $\eta_u = 5°$, and $l = 18$.

Figure 4.7 illustrates the relationship between P_c and BS density λ_b at SINR threshold of 15 dB. The analysis considers three scenarios: complete alignment ($\mu = 1$), partial alignment ($\mu = 0.5$), and no alignment information ($\mu = 0$). A clear trend is observed, indicating that increased BS density significantly enhances coverage probability across all configurations. This

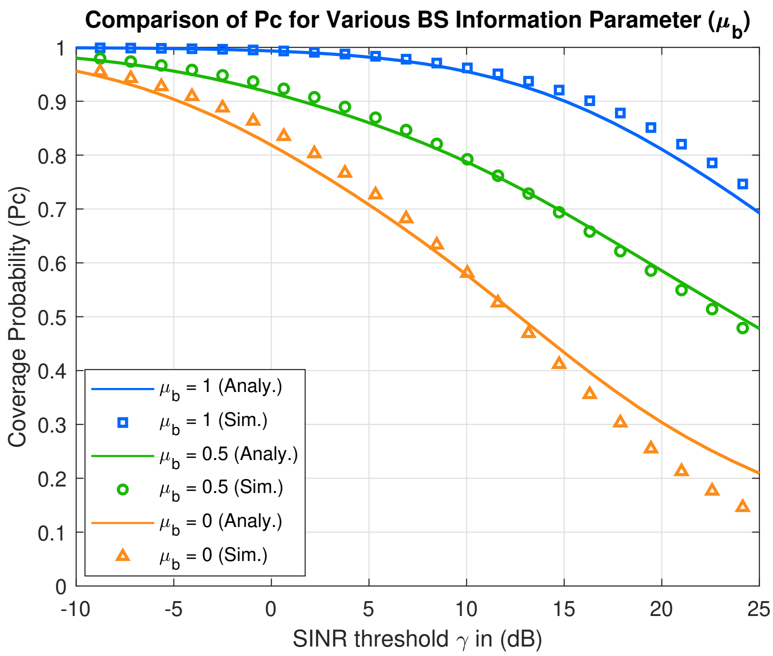

Figure 4.8: Coverage probability P_c (theoretical and Monte Carlo) as a function of SINR thresholds with $\alpha_L = 2$. The system parameters: $C_L = -60\,\text{dB}$, $P_t = 40\,\text{dBm}$, $\eta_b = 30°$, $\eta_u = 5°$, $\lambda_b = 50\,\text{BS/km}^2$, and $l = 18$.

improvement is linked to the reduced expected distance r_o between the typical user, located at the center of a disk-shaped area with radius R, and the nearest BS. As BS density rises, r_o decreases, thereby enhancing the likelihood of the typical user receiving a stronger signal from the closest BS. This effect is particularly pronounced in the complete alignment scenario ($\mu = 1$), where the probability of establishing reliable connections reaches its peak. In contrast, both partial and no alignment information scenarios exhibit lower coverage probabilities, reaffirming the critical role that alignment information plays in optimizing network performance. To provide a comprehensive assessment of the system, we now extend the analysis to a scenario with a path loss exponent of $\alpha = 2$, representative of environments with lower attenuation rates, such as open areas or LOS dominant conditions. This transition allows us to evaluate the impact of reduced path loss on coverage probability P_c and network performance across varying levels of beam alignment information at the serving BS. By comparing results between $\alpha = 4$ and $\alpha = 2$, we gain insight into how different propagation conditions affect signal quality and reliability with dense BS deployments.

Figure 4.8 illustrates the coverage probability P_c as a function of SINR thresholds for different levels of alignment information: perfect ($\mu_b = 1$), partial ($\mu_b = 0.5$), and none ($\mu_b = 0$). When the BS has perfect alignment information ($\mu_b = 1$), P_c is the highest across the range of SINR thresholds. With partial alignment information ($\mu_b = 0.5$), P_c decreases compared to the perfect case but remains higher than when no alignment information is available. In the absence of alignment information ($\mu_b = 0$), P_c reaches its lowest level, illustrating the impact of missing alignment. Therefore, coverage probability improves as the quality of alignment information increases, with partial information still offering a significant advantage over lack of alignment information.

It is important to note that the analytical predictions tend to deviate from Monte Carlo simulation results at high SINR thresholds due to inherent limitations of stochastic geometry when $\alpha = 2$. As discussed in Example 5 of [180], the mean interference in a PPP network is finite only if $\alpha > 2$. For $\alpha = 2$, the interference from distant BSs does not decay sufficiently, which can cause cumulative interference to diverge as the number of BSs increases. Furthermore, [180] highlights the role of an exclusion zone around the typical user, representing an interference-free area proposed to mitigate near-field effects. However, in case of $\alpha = 2$, the interference from just beyond this exclusion zone remains significant, which complicates the accurate interference modeling. Similar trends will be observed in Figures 4.9 and 4.10.

Figure 4.9 illustrates P_c as a function of SINR thresholds for $l = 38$, while Figure 4.8 illustrates the corresponding results for $l = 18$. Both figures assume a constant BS density of $\lambda_b = 50\,\text{BS/km}^2$. The primary difference between the two scenarios lies in the effective coverage area, which is influenced by the value of l, specifically through the effective radius R of the study area, defined as $R = r_o\, l$. For $l = 18$, the effective radius R is approximately 1.27 km, resulting in a total coverage area of about $5\,\text{km}^2$ with around 250 BSs. In contrast, for $l = 38$, the effective radius increases to approximately 2.7 km, leading to a total coverage area of approximately $22\,\text{km}^2$ and around 1100 BSs. Although the increase in the number of BSs due to the larger area may seem advantageous, it also leads to increased interference. This

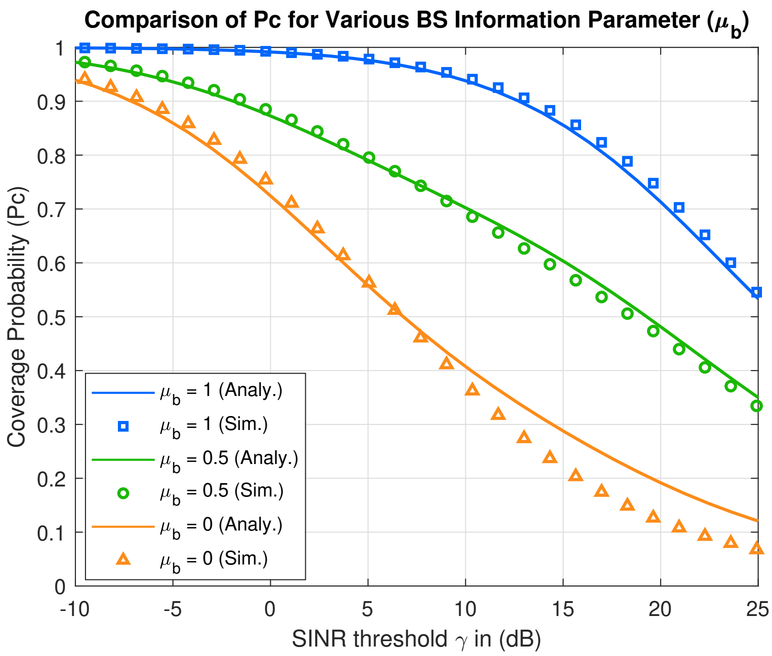

Figure 4.9: Coverage probability P_c (theory and Monte Carlo) vs. SINR thresholds with $\alpha_L = 2$. System parameters: $C_L = -\,60\,\text{dB}$, $P_t = 40\,\text{dBm}$, $\eta_b = 30°$, $\eta_u = 5°$, $\lambda_b = 50/\text{km}^2$, and $l = 38$.

interference can negatively impact the coverage probability P_c, resulting in the lower performance observed in Figure 4.9 compared to Figure 4.8.

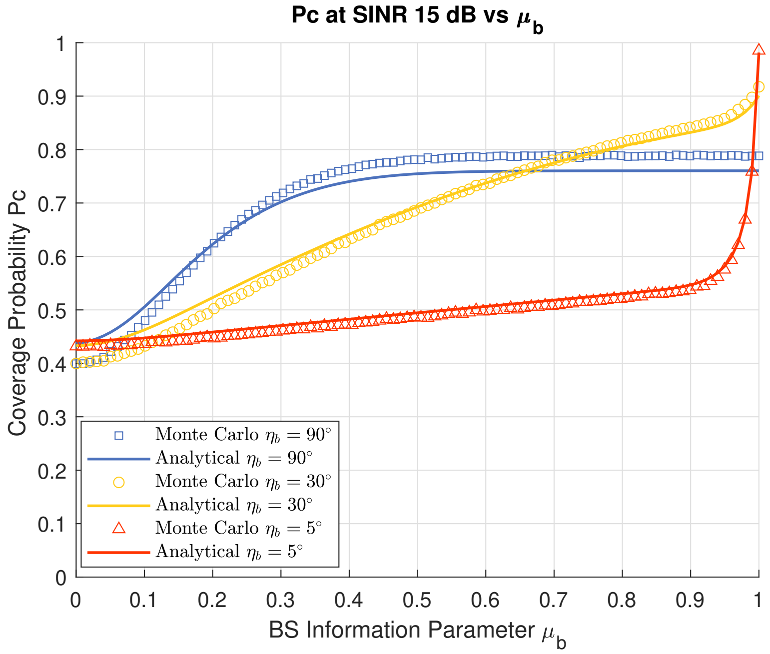

Figure 4.10: Coverage probability P_c (theoretical and Monte Carlo) as a function of BS alignment information parameter μ_b, for $\alpha_L = 2$. This analysis examines three distinct serving BS beamwidths: $\eta_b = 90°$, $\eta_b = 30°$, and $\eta_b = 5°$, with a SINR threshold set at 15 dB. The system parameters: $C_L = -60\,\text{dB}$, $P_t = 40\,\text{dBm}$, $\eta_u = 5°$, $\lambda_b = 50\,\text{BS/km}^2$, and $l = 18$.

Figure 4.10 depicts P_c as a function of the serving BS alignment information parameter, μ_b, which ranges from 0 to 1. The analysis considers three BS beamwidths ($\eta_b = 90°$, $30°$, $\eta_b = 5°$). The SINR threshold is set to 15 dB. Wider beams ($\eta_b = 90°$) offer stable coverage even with limited alignment information. Beyond an alignment information threshold of approximately $\mu_b \approx 0.4$, additional alignment information provides diminishing returns in coverage improvement, making wider beams a practical choice in environments where acquiring complete alignment information is challenging or costly. Medium beams ($\eta_b = 30°$) exhibit improved coverage performance when alignment information exceeds $\mu_b = 0.65$, making them a viable option for scenarios where moderate alignment information is available and can be reliably obtained. In contrast, narrow beams ($\eta_b = 5°$) achieve the highest coverage when alignment information is nearly perfect ($\mu_b \geq 0.98$). However, they are highly sensitive to alignment errors and require a high level of alignment information availability to maintain reliable coverage. As in Figure 4.4 ($\alpha = 4$), regulators can leverage these alignment thresholds to tailor deployment rules authorizing wide beams for low alignment information scenarios, recommending medium beams for partial alignment information, and restricting narrow beams to near-perfect alignment information environments.

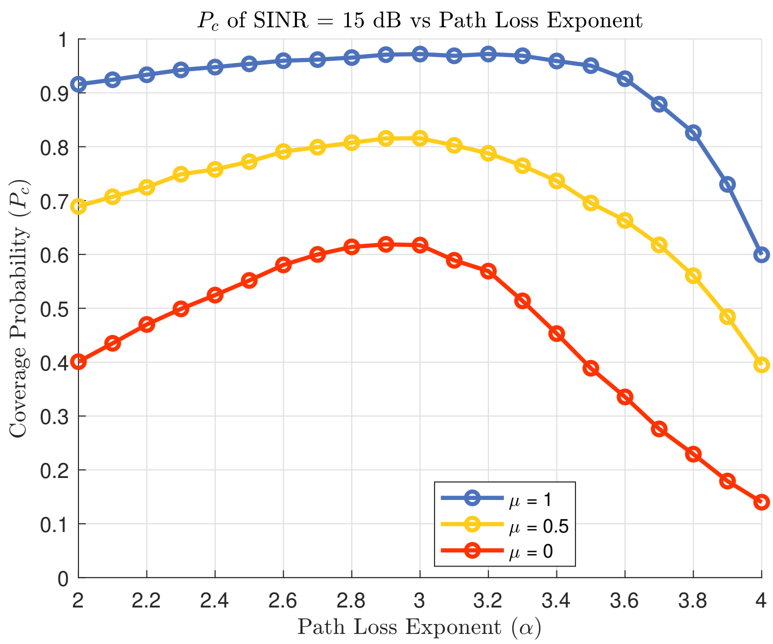

Figure 4.11: Coverage probability P_c via Monte Carlo simulation vs. path loss exponent, with system parameters: $P_t = 40\,\text{dBm}$, $\eta_b = 30°$, $\eta_u = 5°$, $\lambda_b = 50/\text{km}^2$, and $l = 18$.

Figure 4.11 illustrates the influence of the path loss exponents (α) and beam alignment information at the serving BS (μ_b) on network coverage probability, based on Monte Carlo simulation results. The results show that higher alignment information (μ_b) leads to a higher coverage probability, while an increased path loss exponent (α), which signifies a more challenging environment, results in a lower coverage probability across all alignment scenarios. These findings underscore the critical role of the availability of beam alignment information in improving network coverage. In environments with high path loss, the availability of alignment information becomes even more crucial, as its absence significantly degrades coverage performance. In addition, the results show a non-monotonic trend with respect to the path loss exponent α for all values of μ_b. The coverage probability initially increases with α, then exhibits a mild saturation around intermediate values, and finally decreases as α becomes large. This is due to the competing effect of path loss on the desired and interfering signals. At moderate values of α, interference is reduced more rapidly than the desired signal, improving SINR and increasing coverage probability. However, at higher values of α, the desired signal experiences stronger attenuation, which leads to a reduction in SINR and coverage probability.

4.4.2 Performance Comparison Under Different Fading Models

To validate the Rayleigh fading assumption, this subsection presents a Monte Carlo simulation-based comparison of commonly mmWave fading models, including Rayleigh, Rician, Nakagami, and a no-fading scenario. The effect

Table 4.2: Overview of Reported Rician K-factor in mmWave Literature

Environment	Freq. (GHz)	Scenario	K-factor (dB)	Ref.
Indoor Office	25 - 40	LOS	- 1.87 to 1.27	[194]
Indoor Office	25 - 40	OLOS	- 3.79 to -2.31	[194]
Indoor Lab	25 - 40	LOS	0.48 to 3.43	[192]
Indoor Lab	25 - 40	NLOS	- 5.54 to - 0.56	[192]
Indoor Factory	4.9, 28	LOS	5.1 to 5.8	[195]
Open Office	28	LOS	up to 6.15	[193]

of the selected fading models on downlink coverage probability is analyzed under both LOS and NLOS conditions. For the Rician fading model, the K-factor is set to 3 dB for LOS and -5 dB for the NLOS. Table 4.2 provides a measurement-based Rician K-factor observed in typical mmWave environments, which supports the selection of our representative values. For the Nakagami fading model, the shape parameters are set to $M_L = 3$ for LOS and $M_N = 2$ for NLOS, as reported in [11, 18].

Figure 4.12-(a) compares the downlink coverage probability P_c for different fading models under NLOS with $\alpha_N = 4$. The system parameters are: $C_N = -70$ dB, $P_t = 40$ dBm, $\eta_b = 30°$, $\eta_u = 5°$, $\lambda_b = 50$ BS/km^2, and BS information parameter $\mu_b = 0.5$. The corresponding boxplots in Figures 4.12-(b) illustrates the distribution of the coverage probability differences (ΔP_c) between the Rician and Nakagami fading models and the Rayleigh baseline. As observed in Figure 4.12-(a), P_c of Rayleigh closely matches that of the Rician model and is slightly lower than that of the Nakagami model; however, the performance gap remains minimal. This is further supported by the boxplot in Figure 4.12-(b), where the median difference ΔP_c for Rician fading is close to zero, indicating a negligible deviation from Rayleigh. Similarly, for the Nakagami fading, the median ΔP_c is slightly higher than that of the

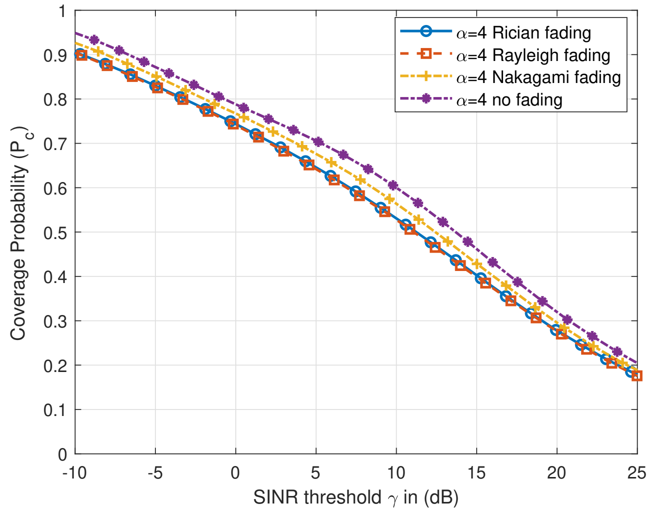

(a) Coverage probability vs. SINR for different fading models

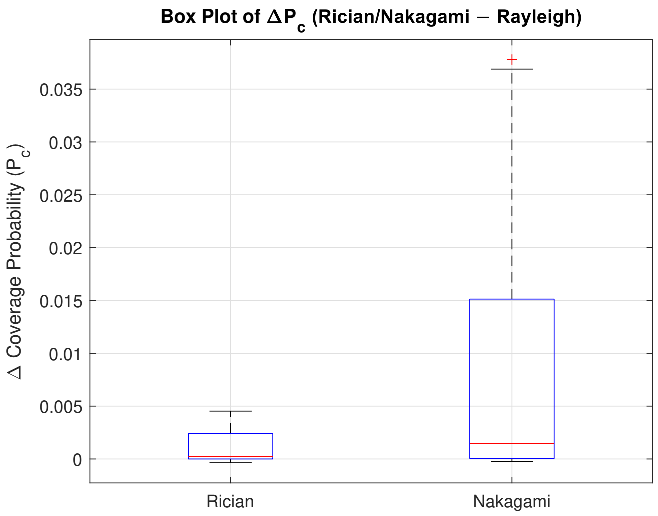

(b) ΔP_c relative to Rayleigh

Figure 4.12: Monte Carlo simulation results comparing fading models under NLOS conditions ($\alpha_N = 4$), with Rician ($K = -5$ dB), Nakagami ($M_N = 2$). Subfigure (a) shows downlink coverage probability vs. SINR for Rayleigh, Rician, Nakagami, and no fading models. Subfigure (b) presents a boxplot showing the distribution of coverage probability differences (ΔP_c) for Rician and Nakagami fading relative to the Rayleigh baseline.

Rician fading but remains near zero, indicating only a minor improvement relative to Rayleigh. Figure 4.13 compares the downlink coverage probabil-

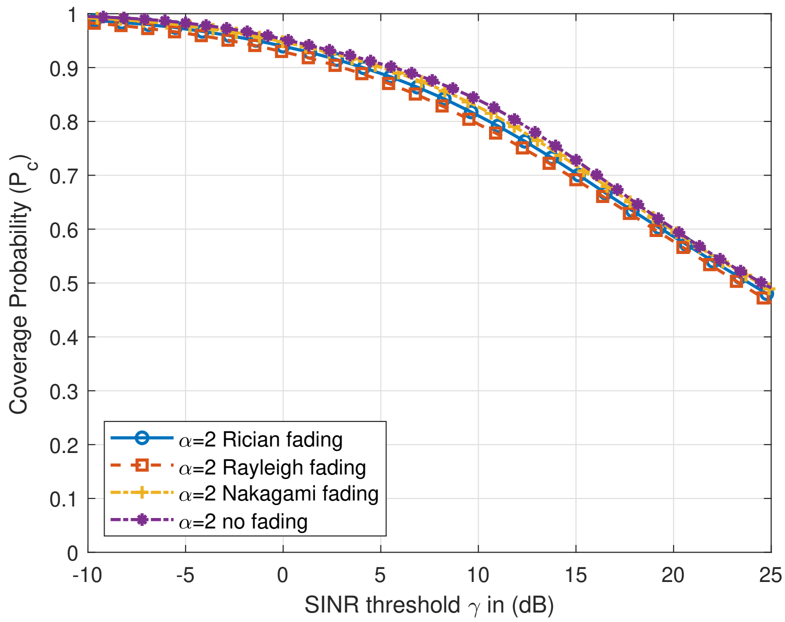

Figure 4.13: Downlink coverage probability versus SINR threshold for different fading models under LOS conditions ($\alpha_L = 2$). The compared models are Rayleigh, Rician ($K = 3$ dB), Nakagami ($M_L = 3$), and a no-fading scenario. Results are obtained from Monte Carlo simulation.

ity P_c as a function of the SINR thresholds for different fading models with $\alpha_L = 2$. The simulation setup follows that of Figure 4.8, with $\mu_b = 0.5$, a Rician K-factor of 3 dB, and Nakagami parameter $M_L = 3$. Rayleigh fading shows slightly lower coverage probability than the Rician and Nakagami models, and the median difference ΔP_c is close to zero for both, indicating only minor deviations from the Rayleigh baseline. These findings support the use of Rayleigh fading as an analytically tractable lower bound for mmWave performance evaluation under both LOS and NLOS conditions.

4.5 Concluding Remarks

This chapter analyzes the coverage probability in cellular mmWave networks using stochastic geometry, focusing on the impact of the availability of alignment information at the serving BS. The analysis considers the effects of beamwidth configurations, BS density, fading models, and path loss exponents under varying level of alignment information. Our key findings (e.g., Figures (4.4) and (4.10)) emphasize the trade-offs between beamwidth and alignment information availability. Wider beams provide relatively stable coverage with limited alignment information, but have a lower ceiling for maximum coverage. Medium beams strike a balance, benefiting from increased alignment information while maintaining competitive performance across a broad range. Narrow beams offer the highest coverage when alignment information is highly available. These findings can assist regulators in defining recommendations for beamwidth selection, particularly in scenarios where acquiring accurate beam alignment information is challenging or resource intensive.

Moreover, the simulation results show that Rayleigh fading consistently yields slightly lower coverage probabilities than Rician and Nakagami fading, while preserving overall performance trends. Therefore, it can be used as a practical and analytically tractable model to evaluate mmWave systems under both LOS and NLOS conditions.

Compared with the omni-user antenna configuration investigated in Chapter 3, the directional user antenna improves the overall coverage probability. However, the fundamental relationship between beamwidth selection and alignment information availability remains unchanged. Wide beams remain robust under limited alignment information, medium beams provide the best trade-off under partial alignment information, and narrow beams require near-perfect alignment information to achieve their maximum performance.

Future research could investigate the impact of user-side alignment information, particularly in scenarios where users actively contribute to the beam alignment process. The model may also be extended to multi-operator scenarios with spectrum sharing, considering both uncoordinated access and coordinated strategies, where directional information exchange can affect interference management, beam alignment, and overall system performance.

Chapter 5

Discrete Gain Approximation Approach

5.1 Introduction

The antenna radiation pattern plays a key role in evaluating the performance of directional antenna arrays in large-scale mmWave networks. Incorporating practical antenna patterns in system-level mathematical analysis is often challenging, as it can lead to significant analytical complexity and loss of tractability. Previous studies [190, 196–198] have therefore focused on tractable approximations of realistic antenna patterns. For instance, the multi-lobe model [196, 197], the multi-cosine pattern [190], and the multi-level flat-top (MLFT) model, have all been proposed to balance analytical simplicity with modeling accuracy. The authors in [196, 197] proposed a multi-lobe approximation to model arbitrary antenna radiation patterns in a tractable manner for system-level analysis, the antenna gain is represented as a piecewise constant across different angular lobes, with the approximation parameters optimized by minimizing the error in the logarithmic gain domain. However, subsequent studies [190, 198] noted that the model in [197] does not fully capture the true directivity gain in the main lobe and may mismatch side-lobe levels, which can introduce deviations in system-level performance evaluation. Moreover, the work in [197] primarily focuses on general cellular networks and does not fully capture the distinct characteristics of mmWave systems with highly directional antennas.

However, these approaches mainly approximate the actual antenna pattern itself and do not account for beam alignment errors. In contrast, this chapter develops a novel analytical framework that incorporates beam alignment errors probabilistically and discretizes main and side lobes, thereby avoiding full numerical integration while retaining realistic directional effects in the coverage probability analysis.

The main contributions of this chapter are summarized as follows:

- **Discrete Gain Method**: The tractable gain method approximates a continuous antenna gain pattern by discretizing the main and side lobes into finite intervals. This approach replaces intractable integrals in coverage probability analysis with finite summations while capturing the effects of beam alignment errors and the realistic antenna model. This method is flexible and can be applied to different antenna models such as cosine and 3GPP standardization patterns; in this thesis, the focus is on the cosine antenna model.
- **Coverage Probability Analysis:** The discrete gain method is integrated into a stochastic geometry framework to analyze downlink coverage in mmWave networks under beam alignment errors. Closed-form expressions are derived for special cases, including no-blockage and full-blockage networks, with the path loss exponent $\alpha = 2$ and $\alpha = 4$, respectively.

5.2 System Model and Methodology

The system model considered in this chapter follows the same general framework presented in Chapter 3, with one key difference: the adoption of a cosine antenna model in place of the sectored (flat-top) antenna model. While the flat-top model provides analytical convenience, it oversimplifies the antenna radiation pattern and often overestimates performance, especially under beam misalignment. In contrast, the cosine-based model provides a more realistic representation of the main lobe and more accurately captures the gradual degradation of the beamforming gain with angular deviation. This feature is particularly important when analyzing beam alignment errors. In the alignment error model presented in Chapter 3, the information parameter controls the variance of the alignment error distribution. Using a cosine antenna model enables a more precise evaluation of how the availability of alignment information affects the beam alignment behavior and consequently how this interaction, combined with practical antenna characteristics, impacts coverage performance.

However, incorporating a realistic antenna pattern such as the cosine model introduces significant analytical complexity, especially when coupled with the stochastic misalignment model. The resulting expressions are generally intractable and typically require numerical integration. To balance analytical tractability with modeling accuracy, a discrete gain approximation method is adopted. The details of this approach are presented in the following subsections.

5.2.1 Antenna Model and Discrete Gain Approximation

The antenna radiation pattern is modeled using the cosine function, which provides a more accurate representation of the main lobe of a practial antenna compared to the flat-top model. The continuous antenna gain as a function of the beam alignment error ϵ is:

$$G(\epsilon) = \begin{cases} G_o \cos^2\left(\frac{\pi}{\eta}\,\epsilon\right), & |\epsilon| \leq \frac{\eta}{2} \\ 0, & \text{otherwise} \end{cases} \tag{5.1}$$

where G_o is the maximum antenna gain and η is the main lobe beamwidth.

Analyzing system performance with the cosine model under beam alignment error is mathematically complex. To preserve analytical tractability while retaining the essential characteristics of the antenna, a discrete gain approximation method is applied, as detailed below.

5.2.1.1 Discrete Gain Approximation Method

The discrete gain approximation method provides a trade-off between analytical tractability and accurately capturing the effects of alignment error on directional beamforming. The approach illustrated in Figure 5.1.

In this method, the main lobe of width η is divided into K intervals, each of width:

$$\Delta\epsilon = \frac{\eta}{2K}.$$

The gain in the $i-th$ interval is approximated as

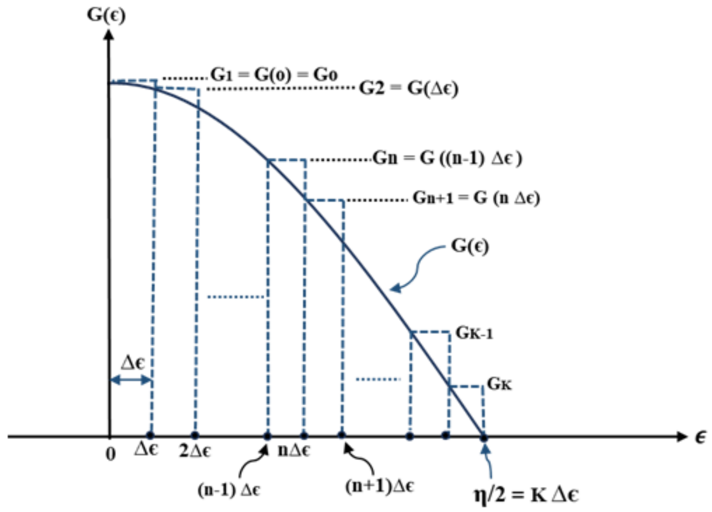

Figure 5.1: Discrete gain approximation of cosine antenna pattern. The continuous gain function $G(\epsilon)$ with main-lobe beamwidth η is divided into K equal angular intervals, each of width $\Delta\epsilon = \eta/2K$. Within each interval, the gain is represented by a constant value $G_1, G_2, \ldots, G_K$, forming a stepwise approximation of the continuous cosine pattern.

$$G_i = G\left(\epsilon = (i-1)\,\Delta\epsilon\right), \quad i = 1, 2, \ldots, K,$$

with the gain in the first interval ($i = 1$) corresponding to the peak of the main lobe:

$$G_1 = G(0) = G_o,$$

and the side lobe gain represented as:

$$G_{K+1} = g,$$

where $g = 0$ for the cosine model, as it does not include side lobes.

This discrete approximation allows the continuous antenna gain to be expressed as a piecewise-constant function, simplifying the analysis while retaining the variations of the continuous cosine pattern. Using this approach, the expected gain under beam alignment error can be derived analytically, as detailed below.

5.2.1.2 Expected Gain with Discrete Approximation

The expected gain under beam alignment error can be made analytically tractable using the discrete gain approximation. Let ϵ be the alignment error, modeled as a random variable with PDF, $f_\epsilon(\epsilon)$, as defined in (3.2). Figure 5.2 illustrates the discrete gain approximation of the cosine antenna gain $G(\epsilon)$ as a function of the alignment error (ϵ), together with the alignment error PDF $f_\epsilon(\epsilon)$, truncated at $b(\mu)$.

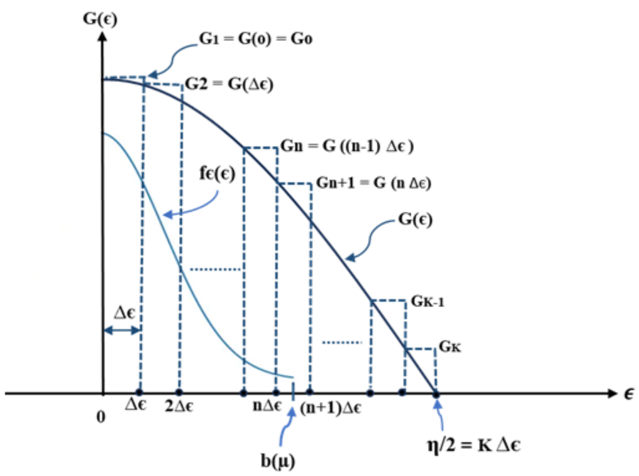

Figure 5.2: Illustration of the discrete gain approximation of the cosine antenna gain $G(\epsilon)$ as a function of the alignment error (ϵ), together with the alignment error PDF $f_\epsilon(\epsilon)$, truncated at $b(\mu)$ (blue curve). Both gain pattern and the PDF of error are plotted on the same graph for visual comparison, with only their positive halves displayed, since both are symmetric around zero.

The expected value of a function $\psi(G(\epsilon))$, where $\psi(\cdot)$ maps the antenna gain $G(\epsilon)$ to performance metric (e.g., received power or SINR), is given by:

$$\mathbb{E}\left[\psi(G(\epsilon))\right] = \int_{-\infty}^{\infty} \psi(G(\epsilon))\, f_\epsilon(\epsilon) d\epsilon.$$

Since the error distribution $f_\epsilon(\epsilon)$ is symmetric around zero and truncated to the interval $[-b(\mu), b(\mu)]$, where $f_\epsilon(\epsilon) = 0$ for $|\epsilon| > b(\mu)$, the above expectation can be expressed as:

$$\mathbb{E}\left[\psi(G(\epsilon))\right] = 2\int_{0}^{b(\mu)} \psi(G(\epsilon))\, f_\epsilon(\epsilon) d\epsilon.$$

In the discrete gain approximation, the main lobe of width η is divided into K intervals of width $\Delta\epsilon = \eta/2K$. Let n denote the number of intervals fully contained within the effective error range $b(\mu)$. Approximating the gain as constant G_s over each interval given by:

$$\begin{aligned}
\mathbb{E}\left[\psi(G(\epsilon))\right] &= 2\int_{0}^{b(\mu)} \psi(G(\epsilon))\, f_\epsilon(\epsilon) d\epsilon \\
&= 2\int_{0}^{\Delta\epsilon} \psi(G_1) f_\epsilon(\epsilon) d\epsilon + 2\int_{\Delta\epsilon}^{2\Delta\epsilon} \psi(G_2) f_\epsilon(\epsilon) d\epsilon + \ldots + 2\int_{(n-1)\Delta\epsilon}^{n\Delta\epsilon} \psi(G_n) f_\epsilon(\epsilon) d\epsilon \\
&\quad + 2\int_{n\Delta\epsilon}^{b(\mu)} \psi(G_{n+1}) f_\epsilon(\epsilon)\, d\epsilon \\
&= \psi(G_1)(\Delta_1 - \Delta_0) + \psi(G_2)(\Delta_2 - \Delta_1) + \ldots + \psi(G_n)(\Delta_n - \Delta_{n-1}) \\
&\quad + 2\int_{0}^{b(\mu)} \psi(G_{n+1}) f_\epsilon(\epsilon) d\epsilon - 2\int_{0}^{n\Delta\epsilon} \psi(G_{n+1}) f_\epsilon(\epsilon) d\epsilon,
\end{aligned}$$

the expected value is obtained as

$$\mathbb{E}\left[\psi(G_{(\epsilon)})\right] = \sum_{s=1}^{n} \psi(G_s)(\Delta_s - \Delta_{s-1}) + \psi(G_{n+1})(1 - \Delta_n), \qquad (5.2)$$

defining

$$\Delta_s = \frac{\operatorname{erf}\left(\frac{\mu\,\eta}{2\sqrt{2}\,\zeta}\frac{s}{K}\right)}{\operatorname{erf}\left(\frac{\mu\,b(\mu)}{\sqrt{2}\,\zeta}\right)}, \quad s = 1, 2, \ldots, n, \quad \Delta_0 = 0,$$

$$\Delta_n = \frac{\operatorname{erf}\left(\frac{\mu\,\eta}{2\sqrt{2}\,\zeta}\frac{n}{K}\right)}{\operatorname{erf}\left(\frac{\mu\,b(\mu)}{\sqrt{2}\,\zeta}\right)},$$

here, μ and $b(\mu)$ are defined in Chapter 3, representing the information parameter and the truncated boundary of $f_\epsilon(\epsilon)$, respectively. The number of discrete intervals n within the effective error range is:

$$n = \begin{cases} K, & b(\mu) \geq \frac{\eta}{2}, \\ \left\lfloor \frac{2K}{\eta} b(\mu) \right\rfloor, & b(\mu) < \frac{\eta}{2}, \end{cases} \tag{5.3}$$

where, $\lfloor \cdot \rfloor$ denotes the floor function to ensure that n is an integer.

The expression in (5.2) replaces a continuous integral with a discrete summation, where each gain value is multiplied by the probability that the misalignment occurs within its corresponding interval. This approach preserves the fundamental characteristics of the continuous antenna pattern while ensuring analytical tractability. Using this approach, the downlink coverage probability under beam misalignment is evaluated in the following section.

5.3 Coverage Probability Analysis

This section extends the downlink coverage probability analysis previously presented in Chapter 3 for the system model shown in Figure 3.1. The main difference lies in the antenna model: while the earlier analysis assumed a flat-top antenna model, the coverage analysis in this chapter adopts the cosine model, combined with the discrete gain approximation introduced in Section 5.2. A generalized framework is first established to capture all possible beam alignment scenarios at both ends of the communication link. This formulation demonstrates that the model accommodates different user antenna configurations: a directional antenna user capable of beam alignment ($\mu_u \neq 0$), or an omni-antenna user that does not perform beamforming ($\mu_u = 0$). The analysis builds on the general expressions for SINR in (3.9) -(3.13) from Chapter 3, with the continuous antenna gain replaced by the discrete approximation. The following subsections present closed-form expressions for the downlink coverage probability under LOS ($\alpha = 2$) and NLOS ($\alpha = 4$) conditions.

The analysis begins with the interference term. As assumed in the system model, the interfering BSs do not perform beamforming toward the typical user (i.e. $\mu_b = 0$), and therefore their beam alignment error is uniformly distributed over $[-\pi, \pi]$, and the user is also assumed to have no alignment information ($\mu_u = 0$) towards interfering links. Applying the discrete gain approximation method to the interference term in (3.14) gives:

$$\begin{aligned}
&= \exp\Bigg(\int_{r_o}^{R} \sum_{i=1}^{K} \sum_{J=1}^{T} \frac{-\rho G_i^{Ib} G_J^{Iu} C r^{-\alpha}}{1 + \rho G_i^{Ib} G_J^{Iu} C r^{-\alpha}} \left(\frac{\eta_b \eta_u}{4\pi^2 KT}\right) (2\pi\lambda r dr) \\
&+ \int_{r_o}^{R} \sum_{J=1}^{T} \frac{-\rho g^{Ib} G_J^{Iu} C r^{-\alpha}}{1 + \rho g^{Ib} G_J^{Iu} C r^{-\alpha}} \left(1 - \frac{\eta_b}{2\pi}\right) \left(\frac{\eta_u}{2\pi T}\right) (2\pi\lambda r dr) \\
&+ \int_{r_o}^{R} \sum_{i=1}^{K} \frac{-\rho g^{Iu} G_i^{Ib} C r^{-\alpha}}{1 + \rho g^{Iu} G_i^{Ib} C r^{-\alpha}} \left(1 - \frac{\eta_u}{2\pi}\right) \left(\frac{\eta_b}{2\pi K}\right) (2\pi\lambda r dr) \\
&+ \int_{r_o}^{R} \frac{-\rho g^{Iu} g^{Ib} C r^{-\alpha}}{1 + \rho g^{Iu} g^{Ib} C r^{-\alpha}} \left(1 - \frac{\eta_u}{2\pi}\right) \left(1 - \frac{\eta_b}{2\pi}\right) (2\pi\lambda r dr)\Bigg).
\end{aligned} \tag{5.4}$$

Here, G_i^{Ib} and G_J^{Iu} represent the discrete main-lobe gains of interfering BSs and the typical user, respectively, while g^{Ib} and g^{Iu} denote their corresponding side-lobe gains. K and T represent the the number of discrete intervals related to the antenna gain of the BS and the typical user, respectively. The expression in (5.4) can be rewritten in a compact form as:

$$= \exp - \left(\sum_{i=1}^{K} \sum_{J=1}^{T} C_{iJ} + \sum_{J=1}^{T} D_J + \sum_{i=1}^{K} H_i + L \right), \tag{5.5}$$

and substituting (5.5) into (3.13) yields:

$$P_c = \int_{-b(\mu_b)}^{b(\mu_b)} \int_{-b(\mu_u)}^{b(\mu_u)} \int_0^{\infty} e^{-\left(\rho\sigma_{\bar{n}}^2 + \sum_{i=1}^{K} \sum_{J=1}^{T} C_{iJ} + \sum_{J=1}^{T} D_J + \sum_{i=1}^{K} H_i + L\right)} f_{r_o}(r_o) dr_o f_{\epsilon_b}(\epsilon_b) f_{\epsilon_u}(\epsilon_u) d\epsilon_b d\epsilon_u, \tag{5.6}$$

Let $\psi_{(\alpha)}\left(G^{ab}_{\mu_b \neq 0}(\epsilon_b), G^{au}_{\mu_u \neq 0}(\epsilon_u)\right) = \int_0^{\infty} e^{-\left(\rho\,\sigma_{\bar{n}}^2 + \sum_{i=1}^{K} \sum_{J=1}^{T} C_{iJ} + \sum_{J=1}^{T} D_J + \sum_{i=1}^{K} H_i + L\right)} f_{r_o}(r_o)\, dr_o$ (5.7)

For the serving link, the BS participates in beam alignment (i.e., $\mu_b \neq 0$). In this case, the beam alignment error ϵ_b follows the PDF $f_{\epsilon_b}(\epsilon_b)$ given in (3.2), truncated to the interval $[-b(\mu_b), b(\mu_b)]$. The discrete-gain approximation method is applied to compute (G_s^{ab} and G_q^{au}) for ($\mu_b \neq 0$, $\mu_u \neq 0$), yielding:

$$P_c = \sum_{q=1}^{m}\sum_{s=1}^{n}\psi_{(\alpha)}(G_s^{ab}, G_q^{au})(\Delta_s^b - \Delta_{s-1}^b)(\Delta_q^u - \Delta_{q-1}^u)$$
$$+ \sum_{s=1}^{n}\psi_{(\alpha)}(G_s^{ab}, G_{m+1}^{au})(\Delta_s^b - \Delta_{s-1}^b)(1 - \Delta_m^u)$$
$$+ \sum_{q=1}^{m}\psi_{(\alpha)}(G_{n+1}^{ab}, G_q^{au})(1 - \Delta_n^b)(\Delta_q^u - \Delta_{q-1}^u)$$
$$+ \psi_{(\alpha)}(G_{n+1}^{ab}, G_{m+1}^{au})(1 - \Delta_n^b)(1 - \Delta_m^u) \quad (5.8)$$

where

$$\psi_{(\alpha)}\left(G_s^{ab}, G_q^{au}\right) = \int_0^\infty e^{-\left(\frac{\gamma\sigma_n^2 r_o^\alpha}{G_s^{ab}G_q^{au}C} + \sum_{i=1}^{K}\sum_{J=1}^{T} C_{iJsq}^{(\alpha)} + \sum_{J=1}^{T} D_{Jsq}^{(\alpha)} + \sum_{i=1}^{K} H_{isq}^{(\alpha)} + L_{sq}^{(\alpha)}\right)} f_{r_o}(r_o)\, dr_o, \quad (5.9)$$

here, G_s^{ab} represents the discrete main lobe gain of the serving BS and G_q^{au} denotes the discrete main-lobe gain of the typical user. Using the definition of the hypergeometric function ${}_2F_1(a,b;c;z)$, where ${}_2F_1(\cdot) = {}_2F_1\left(1, \frac{2}{\alpha}; \frac{2}{\alpha}+1; (\cdot)\right)$.

$$C_{iJsq}^{\alpha} = \left(\frac{\eta_b\eta_u}{4\pi^4 KT}\right)\left[\pi\lambda R^2\, {}_2F_1\left(\frac{-G_s^{ab}G_q^{au}}{G_i^{Ib}G_J^{Iu}\gamma}\right)\left(\frac{R}{r_o}\right)^\alpha - \pi\lambda r_o^2\, {}_2F_1\left(\frac{-G_s^{ab}G_q^{au}}{G_i^{Ib}G_J^{Iu}\gamma}\right)\right]$$
$$D_{Jsq}^{\alpha} = \left(\frac{\eta_u}{2\pi T}\left(1-\frac{\eta_b}{2\pi}\right)\right)\left[\pi\lambda R^2\, {}_2F_1\left(\frac{-G_s^{ab}G_q^{au}}{g^{Ib}G_J^{Iu}\gamma}\right)\left(\frac{R}{r_o}\right)^\alpha - \pi\lambda r_o^2\, {}_2F_1\left(\frac{-G_s^{ab}G_q^{au}}{g^{Ib}G_J^{Iu}\gamma}\right)\right]$$
$$H_{isq}^{\alpha} = \left(\frac{\eta_b}{2\pi K}\left(1-\frac{\eta_u}{2\pi}\right)\right)\left[\pi\lambda R^2\, {}_2F_1\left(\frac{-G_s^{ab}G_q^{au}}{G_i^{Ib}g^{Iu}\gamma}\right)\left(\frac{R}{r_o}\right)^\alpha - \pi\lambda r_o^2\, {}_2F_1\left(\frac{-G_s^{ab}G_q^{au}}{G_i^{Ib}g^{Iu}\gamma}\right)\right]$$
$$L_{sq}^{\alpha} = \left(1-\frac{\eta_b}{2\pi}\right)\left(1-\frac{\eta_u}{2\pi}\right)\left[\pi\lambda R^2\, {}_2F_1\left(\frac{-G_s^{ab}G_q^{au}}{g^{Ib}g^{Iu}\gamma}\right)\left(\frac{R}{r_o}\right)^\alpha - \pi\lambda r_o^2\, {}_2F_1\left(\frac{-G_s^{ab}G_q^{au}}{g^{Ib}g^{Iu}\gamma}\right)\right] \quad \text{(a)}$$

The number of discrete intervals n and m within the effective error range for the BS and the user is defined as:

$$n = \begin{cases} K, & b(\mu_b) \geq \frac{\eta_b}{2}, \\ \left\lfloor \frac{2K}{\eta_b} b(\mu_b) \right\rfloor, & b(\mu_b) < \frac{\eta_b}{2}, \end{cases}$$

$$m = \begin{cases} T, & b(\mu_u) \geq \frac{\eta_u}{2} \\ \left\lfloor \frac{2T}{\eta_u} b(\mu_u) \right\rfloor, & b(\mu_u) < \frac{\eta_u}{2}. \end{cases}$$

The truncated boundary of the PDF of the beam alignment error for both BS and the user is given by:

$$\begin{aligned} b(\mu_b) &= \pi - \mu_b \left(\pi - \frac{\eta_b}{2K} \right), \\ b(\mu_u) &= \pi - \mu_u \left(\pi - \frac{\eta_u}{2T} \right), \end{aligned} \tag{b}$$

$$\Delta_s^b = \frac{\operatorname{erf}\left(\frac{\eta_b \mu_b}{2\sqrt{2}\zeta_b} \frac{s}{K} \right)}{\operatorname{erf}\left(\frac{\mu_b b(\mu_b)}{\sqrt{2}\zeta_b} \right)}, \qquad \Delta_q^u = \frac{\operatorname{erf}\left(\frac{\eta_u \mu_u}{2\sqrt{2}\zeta_u} \frac{q}{T} \right)}{\operatorname{erf}\left(\frac{\mu_u b(\mu_u)}{\sqrt{2}\zeta_u} \right)} \tag{c}$$

$$\begin{aligned} & G_i^{Ib} = G^b \left(\epsilon = \frac{\eta_b (i-1)}{2K} \right), \quad G_s^{ab} = G^b \left(\epsilon = \frac{\eta_b (s-1)}{2K} \right), \quad G_{K+1}^{ab} = g^{Ib} \\ & G_J^{Iu} = G^u \left(\epsilon = \frac{\eta_u (J-1)}{2T} \right), \quad G_J^{au} = G^u \left(\epsilon = \frac{\eta_u (q-1)}{2T} \right), \quad G_{T+1}^{au} = g^{Iu} \\ & i, J = 1, 2, \ldots, K,\ T \\ & s, q = 1, 2, \ldots, n,\ m \end{aligned} \tag{d}$$

5.3.1 Path Loss Exponent 2

Following the same assumptions as in Chapter 3, where the path loss exponent is set to $\alpha = 2$ and the outer radius of the disk region is defined as $R = lr_o$, these assumptions are substituted into (5.9), and (a) is subsequently applied. The resulting expression is given in (5.10).

$$\psi_{(2)}(G_s^{ab}, G_q^{au}) = \frac{1}{1 + \frac{\gamma\sigma_{\bar{n}}^2}{G_s^{ab}G_q^{au}\pi\lambda C} + \sum_{i=1}^{K}\sum_{J=1}^{T}\tilde{C}_{iJsq} + \sum_{J=1}^{T}\tilde{D}_{Jsq} + \sum_{i=1}^{K}\tilde{H}_{isq} + \tilde{L}_{sq}} \tag{5.10}$$

where $\tilde{C}_{iJsq}$, $\tilde{D}_{Jsq}$, $\tilde{H}_{isq}$, and $\tilde{L}_{sq}$ are:

$$\tilde{C}_{iJsq}^{\alpha=2} = \left(\frac{G_i^{Ib}G_J^{Iu}}{G_s^{ab}G_q^{au}}\gamma\right)\ln\left[\frac{\frac{G_i^{Ib}G_J^{Iu}}{G_s^{ab}G_q^{au}}\gamma + l^2}{\frac{G_i^{Ib}G_J^{Iu}}{G_s^{ab}G_q^{au}}\gamma + 1}\right]\left(\frac{\eta_u\eta_b}{4\pi^2KT}\right)$$

$$\tilde{D}_{Jsq}^{\alpha=2} = \left(\frac{g^bG_J^{Iu}}{G_s^{ab}G_q^{au}}\gamma\right)\ln\left[\frac{\frac{g^bG_J^{Iu}}{G_s^{ab}G_q^{au}}\gamma + l^2}{\frac{g^bG_J^{Iu}}{G_s^{ab}G_q^{au}}\gamma + 1}\right]\left(\frac{\eta_u}{2\pi T}\right)\left(1 - \frac{\eta_b}{2\pi}\right)$$

$$\tilde{H}_{isq}^{\alpha=2} = \left(\frac{G_i^{Ib}g^u}{G_s^{ab}G_q^{au}}\gamma\right)\ln\left[\frac{\frac{G_i^{Ib}g^u}{Gs^{ab}G_q^{au}}\gamma + l^2}{\frac{G_i^{Ib}g^u}{Gs^{ab}G_q^{au}}\gamma + 1}\right]\left(\frac{\eta_b}{2\pi K}\right)\left(1 - \frac{\eta_u}{2\pi}\right)$$

$$\tilde{L}_{sq}^{\alpha=2} = \left(\frac{g^bg^u}{G_s^{ab}G_q^{au}}\gamma\right)\ln\left[\frac{\frac{g^bg^u}{G_s^{ab}G_q^{au}}\gamma + l^2}{\frac{g^bg^u}{G_s^{ab}G_q^{au}}\gamma + 1}\right]\left(1 - \frac{\eta_u}{2\pi}\right)\left(1 - \frac{\eta_b}{2\pi}\right) \tag{e}$$

5.3.2 Path loss exponent 4

Following the same assumptions as in Chapter 3, where the path loss exponent is set to $\alpha = 4$ and the outer radius of the disk region is defined as $R = lr_o$, these assumptions are substituted into (5.9), and (a) is applied. The resulting expression is given in (5.11).

$$\begin{aligned}\psi_{(4)}(G_s^{ab}, G_q^{au}) = &\left(\frac{\pi^{3/2}\lambda\sqrt{G_s^{ab}G_q^{au}C}}{2\sigma_{\bar{n}}\sqrt{\gamma}}\right)\\ &\times\exp\left(\left(\frac{\pi^2\lambda^2 G_s^{ab}G_q^{au}C}{4\gamma\sigma_{\bar{n}^2}}\right)\left(1+\sum_{i=1}^{K}\sum_{J=1}^{T}\tilde{\tilde{C}}_{iJsq}+\sum_{J=1}^{T}\tilde{\tilde{D}}_{Jsq}+\sum_{i=1}^{K}\tilde{\tilde{H}}_{isq}+\tilde{\tilde{L}}_{sq}\right)^2\right)\\ &\times\operatorname{erfc}\left[\frac{\pi\lambda\sqrt{G_s^{ab}G_q^{au}C}}{2\sigma_{\bar{n}}\sqrt{\gamma}}\left(1+\sum_{i=1}^{K}\sum_{J=1}^{T}\tilde{\tilde{C}}_{iJsq}+\sum_{J=1}^{T}\tilde{\tilde{D}}_{Jsq}+\sum_{i=1}^{K}\tilde{\tilde{H}}_{isq}+\tilde{\tilde{L}}_{sq}\right)\right],\end{aligned} \tag{5.11}$$

$$\tilde{\tilde{C}}_{iJsq}^{\alpha=4} = \left(\frac{G_i^{Ib}G_J^{Iu}\gamma}{G_s^{ab}G_q^{au}}\right)^{1/2}\left[\tan^{-1}\left(\frac{G_i^{Ib}G_J^{Iu}l^4}{G_s^{ab}G_q^{au}\gamma}\right)^{1/2} - \tan^{-1}\left(\frac{G_i^{Ib}G_J^{Iu}}{G_s^{ab}G_q^{au}\gamma}\right)^{1/2}\right]\frac{\eta_u\eta_b}{4\pi KT}$$

$$\tilde{\tilde{D}}_{Jsq}^{\alpha=4} = \left(\frac{g^b G_J^{Iu}\gamma}{G_s^{ab}G_q^{au}}\right)^{1/2}\left[\tan^{-1}\left(\frac{G_s^{ab}G_q^{au}l^4}{g^b G_J^{Iu}\gamma}\right)^{1/2} - \tan^{-1}\left(\frac{G_s^{ab}G_q^{au}}{g^b G_J^{Iu}\gamma}\right)^{1/2}\right]\frac{\eta_u}{2\pi T}\left(1-\frac{\eta_b}{2\pi}\right)$$

$$\tilde{\tilde{H}}_{isq}^{\alpha=4} = \left(\frac{G_i^{Ib}g^u\gamma}{G_s^{ab}G_q^{au}}\right)^{1/2}\left[\tan^{-1}\left(\frac{G_s^{ab}G_q^{au}l^4}{g^u G_i^{Ib}\gamma}\right)^{1/2} - \tan^{-1}\left(\frac{G_s^{ab}G_q^{au}}{g^u G_i^{Ib}\gamma}\right)^{1/2}\right]\frac{\eta_b}{2\pi K}\left(1-\frac{\eta_u}{2\pi}\right)$$

$$\tilde{\tilde{L}}_{sq}^{\alpha=4} = \left(\frac{g^b g^u \gamma}{G_s^{ab} G_q^{au}}\right)^{1/2} \left[\tan^{-1}\left(\frac{G_s^{ab} G_q^{au} l^4}{g^u g^b \gamma}\right)^{1/2} - \tan^{-1}\left(\frac{G_s^{ab} G_q^{au}}{g^u g^b \gamma}\right)^{1/2}\right] \left(1 - \frac{\eta_b}{2\pi}\right)\left(1 - \frac{\eta_u}{2\pi}\right) \tag{f}$$

5.3.3 Special Case: Cosine-Antenna BS and Omni-Antenna User

The downlink coverage probability for the typical user assumes an omni-antenna, while the BS utilizes a directional antenna with a cosine antenna model. Under these assumptions, the expression in (5.8) can be significantly simplified. For an omni-user antenna:

$$\begin{aligned}
\eta_u = 2\pi, \quad T = 1, \quad \Rightarrow \quad & J = T = 1, \quad m = T = 1 = q, \\
& \Delta_q^u = \Delta_1^u = 1, \quad \Delta_{q-1}^u = \Delta_0^u = 0 \\
& \Rightarrow \Delta_q^u - \Delta_{q-1}^u = 1, \quad (1 - \Delta_m^u) = (1 - \Delta_1^u) = 0 \\
& \Rightarrow \text{2nd and 4th terms in (5.8) vanish, and from} (e): \\
& \tilde{H}_{isq}^{\alpha=2} \text{ and } \tilde{L}_{sq}^{\alpha=2} = 0,
\end{aligned}$$

further:

$$\begin{aligned}
& G_q^{au} = G_1^{au} = G_o^u = 1, \\
& G_J^{Iu} = G_1^{Iu} = G_o^u = 1,
\end{aligned} \tag{5.12}$$

using (5.12), (5.8) will be:

$$P_c = \sum_{s=1}^{n} \psi_{(\alpha)}(G_s^{ab}, 1)(\Delta_s^b - \Delta_{s-1}^b) + \psi_{(\alpha)}(g^{Ib}, 1)(1 - \Delta_n^b) \quad (5.13)$$

where $G_{n+1}^{ab} = G_{K+1}^{ab} = g^{Ib}$

For the BS with cosine antenna model, and as discussed in Section (5.2), the cosine with approximation given by:

$$G_i(\epsilon) = G_o^b \cos^2\left(\frac{\pi}{\eta}(i-1)\Delta\epsilon\right), \quad \Delta\epsilon = \frac{\eta}{2K}$$

$$G_i = G_o^b \cos^2\left(\beta\frac{(i-1)}{K}\right), \quad \beta = \frac{\pi}{2}$$

$$G_s^{ab} = G_o^b \cos^2\left(\beta\frac{s-1}{K}\right),$$

$$G_i^{Ib} = G_o^b \cos^2\left(\beta\frac{i-1}{K}\right),$$

For $\alpha = 2$, using (5.10) and (e), the coverage probability P_c in (5.13) becomes:

$$P_c = \left(\sum_{s=1}^{n} \frac{\left(\Delta_s^b - \Delta_{s-1}^b\right)}{1 + \frac{\gamma\,\sigma_{\bar{n}}^2}{G_s^{ab}\,C\,\pi\lambda} + \sum_{i=1}^{K} C_{is} + D_s}\right) + \left(\frac{(1-\Delta_n^b)}{1 + \frac{\gamma\,\sigma_{\bar{n}}^2}{g^{Ib}\,C\,\pi\lambda} + \sum_{i=1}^{K} C_i + D}\right), \quad (5.14)$$

$$C_{is} = \left(\frac{G_i^{Ib}}{G_s^{ab}}\,\gamma\right) \ln\left(\frac{\frac{G_i^{Ib}}{G_s^{ab}}\,\gamma + l^2}{\frac{G_i^{Ib}}{G_s^{ab}}\,\gamma + 1}\right) \frac{\eta_b}{2\pi K}$$

$$D_s = \left(\frac{g^{Ib}}{G_s^{ab}}\,\gamma\right) \ln\left(\frac{\frac{g^{Ib}}{G_s^{ab}}\,\gamma + l^2}{\frac{g^{b}}{G_s^{ab}}\,\gamma + 1}\right)\left(1 - \frac{\eta_b}{2\pi}\right)$$

$$C_i = \left(\frac{G_i^{Ib}}{g^{Ib}}\,\gamma\right) \ln\left(\frac{\frac{G_i^{Ib}}{g^{Ib}}\,\gamma + l^2}{\frac{G_i^{Ib}}{g^{Ib}}\,\gamma + 1}\right)\frac{\eta_b}{2\pi K}$$

$$D = \gamma \ln\left(\frac{\gamma + l^2}{\gamma + 1}\right)\left(1 - \frac{\eta_b}{2\pi}\right)$$

$$\Delta_s^b = \frac{\mathrm{erf}\left(\frac{\mu_b\,\eta_b\,s}{2\sqrt{2}\,\zeta_b\,K}\right)}{\mathrm{erf}\left(\frac{\mu_b\,b(\mu_b)}{\sqrt{2}\,\zeta_b}\right)},$$

$$\Delta_n^b = \frac{\mathrm{erf}\left(\frac{\mu_b\,\eta_b\,n}{2\sqrt{2}\,\zeta_b\,K}\right)}{\mathrm{erf}\left(\frac{\mu_b\,b(\mu_b)}{\sqrt{2}\,\zeta_b}\right)}.$$

For the cosine antenna model, the side lobe $g^{Ib} = 0$. Therefore, the coverage probability P_c in (5.14) can be simplified and rewritten as:

$$P_c = \sum_{s=1}^{n} \frac{\left(\Delta_s^b - \Delta_{s-1}^b\right)}{1 + \frac{\gamma\,\sigma_n^2}{G_s^{ab}\,C\,\pi\lambda} + \sum_{i=1}^{K} C_{is}}. \tag{5.15}$$

For $\alpha = 4$, using (5.11) and (f), the P_c expression in (5.13) will be:

$$P_c = \sum_{s=1}^{n} \frac{\pi^{3/2}\lambda\sqrt{G_s^{ab}C}}{2\sigma_{\bar{n}}\sqrt{\gamma}} \exp\left(\frac{\pi^2\lambda^2 G_s^{ab}C}{4\gamma\sigma_{\bar{n}}^2}\left(1+\sum_{i=1}^{K} C_{is} + D_s\right)^2\right)$$
$$\times \operatorname{erfc}\left(\frac{\pi\lambda\sqrt{G_s^{ab}C}}{2\sigma_{\bar{n}}\sqrt{\gamma}}\left(1+\sum_{i=1}^{K} C_{is} + D_s\right)\right)\left(\Delta_s^b - \Delta_{s-1}^b\right)$$
$$+ \frac{\pi^{3/2}\lambda\sqrt{g^{Ib}C}}{2\sigma_{\bar{n}}\sqrt{\gamma}} \exp\left(\frac{\pi^2\lambda^2 g^{Ib}C}{4\gamma\sigma_{\bar{n}}^2}\left(1+\sum_{i=1}^{K} C_i + D\right)^2\right)$$
$$\times \operatorname{erfc}\left(\frac{\pi\lambda\sqrt{g^{Ib}C}}{2\sigma_{\bar{n}}\sqrt{\gamma}}\left(1+\sum_{i=1}^{K} C_i + D\right)\right)(1-\Delta_n)) \quad (5.16)$$

$$C_{is}^{\alpha=4} = \sqrt{\frac{G_i^{Ib}}{G_s^{ab}}\gamma}\left[\tan^{-1}\left(\sqrt{\frac{G_s^{ab}}{G_i^{Ib}\gamma}}l^2\right) - \tan^{-1}\left(\sqrt{\frac{G_s^{ab}}{G_i^{Ib}\gamma}}\right)\right]\frac{\eta_b}{2\pi K}$$

$$C_{i}^{\alpha=4} = \sqrt{\frac{G_i^{Ib}}{g^{Ib}}\gamma}\left[\tan^{-1}\left(\sqrt{\frac{g^{Ib}}{G_i^{Ib}\gamma}}l^2\right) - \tan^{-1}\left(\sqrt{\frac{g^{Ib}}{G_i^{Ib}\gamma}}\right)\right]\frac{\eta_b}{2\pi K}$$

$$D_{s}^{\alpha=4} = \sqrt{\frac{g^{Ib}}{G_s^{ab}}\gamma}\left[\tan^{-1}\left(\sqrt{\frac{G_s^{ab}}{g^{Ib}\gamma}}l^2\right) - \tan^{-1}\left(\sqrt{\frac{G_s^{ab}}{g^{Ib}\gamma}}\right)\right]\left(1-\frac{\eta_b}{2\pi}\right)$$

$$D^{\alpha=4} = \sqrt{\gamma}\left[\tan^{-1}\left(\frac{l^2}{\sqrt{\gamma}}\right) - \tan^{-1}\left(\frac{1}{\sqrt{\gamma}}\right)\right]\left(1-\frac{\eta_b}{2\pi}\right)$$

With $g^{Ib} = 0$, D_s in the first term of (5.16) becomes zero, and the entire second term vanishes.

5.4 Simulation and Discussion Results

This section analyzes the coverage in the presence of beam alignment errors and verifies the precision of the developed analytical framework through Monte Carlo simulations. Table 5.1 presents the key simulation parameters.

Table 5.1: Simulation Parameters

Notation	Description	Value
λ_b	BS density	$50/\text{km}^2$
α_L, α_N	LOS and NLOS path loss exponents, respectively	2, 4
C_L, C_N	LOS and NLOS path loss intercepts, respectively	- 60 dB, - 70 dB
f_c	Carrier frequency	28 GHz
W	Bandwidth	100 MHz
ζ_b	Antenna system inefficiency factor	0.158
l	Positive integer scaling factor ($l > 1$, $R = r_o\, l$)	8
σ_n^2	Noise power	- 174 dBm/Hz + 10 $\log_{10}$ (W) + 10 dB

5.4.1 Discrete Cosine Approximation Validation

To validate the discrete cosine approximation approach, the coverage probability obtained from the continuous cosine antenna pattern is compared with its discrete approximation using Monte Carlo simulations under the same system model and framework. As shown in Figure (5.3), the comparison demonstrates that the precision of the discrete approximation depends on the number of discrete intervals K. For a small number of intervals (e.g., $K = 2$ or 4) the approximation is coarse, while increasing K (e.g., $K = 8$ or 16) captures the main lobe more accurately and closely matches the continuous pattern. For subsequent system-level simulations, $K = 8$ is selected, as it captures the main-lobe sufficiently well, while $K = 16$ provides only a marginally finer resolution.

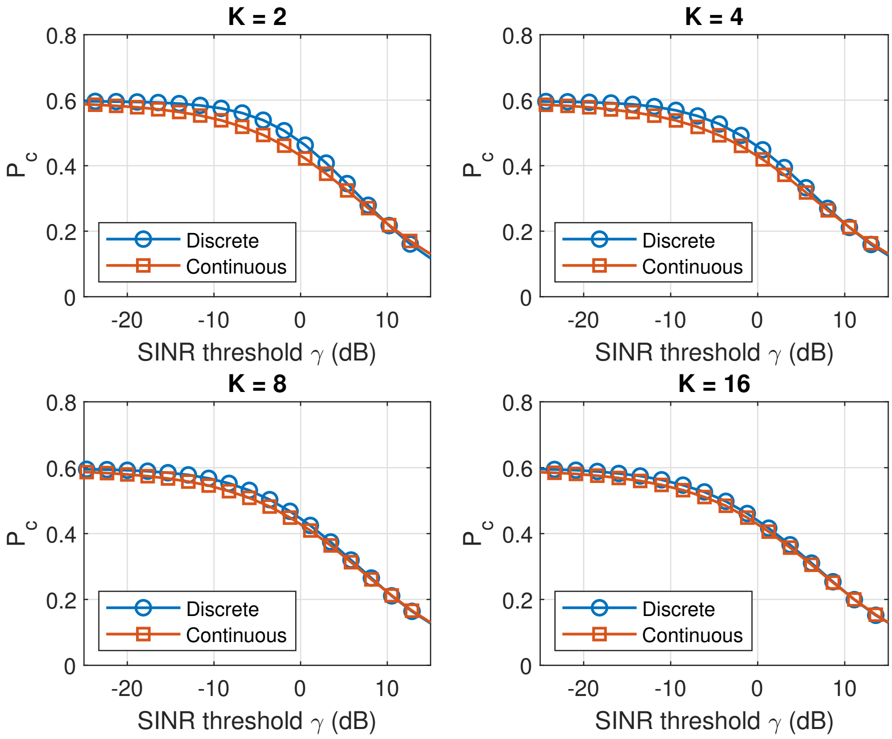

Figure 5.3: Monte Carlo simulation for coverage probability P_c for the continuous cosine antenna pattern and its discrete approximations with different numbers of intervals $K = 2, 4, 8, 16$ under the same system model with beam alignment error ϵ. Simulation parameters: path loss exponent $\alpha = 2$, information parameter $\mu_b = 0.5$, BS transmit power $P_t = 30\,\text{dBm}$, BS beamwidth $\eta_b = 30°$.

5.4.2 Cosine vs Flat-top Coverage Comparison

The coverage probability obtained using the cosine antenna model with the approximation approach is compared with that of the flat-top model presented in Chapter (3) (Figure (3.6) for $\alpha = 2$ and Figure(3.10) for $\alpha = 4$). Under identical system parameters, the comparisons shown in Figure (5.4) and Figure (5.5) reveal noticeable differences in coverage performance across various SINR thresholds and levels of beam alignment information.

When only partial alignment information ($\mu_b = 0.5$) or no information ($\mu_b = 0$) is available, the flat-top model demonstrates a higher coverage probability. This arises from differences in the representation of the antenna array radiation pattern in the two models. As discussed in Section (5.2), the flat-top model approximates the actual antenna array pattern by assuming a constant gain for all angles within the main lobe (G_o^b) and another constant side lobe gain ($g^b \neq 0$)(see (3.8)). This simplification neglects the gradual gain roll-off that occurs in practical antenna patterns, leading to an inaccurate characterization of the received signal strength under beam misalignment. As a result, the flat-top model tends to overestimate coverage because it fails to accurately capture the reduction in directional beamforming gain due to angular deviations.

Under perfect alignment information ($\mu_b = 1$), the coverage probability obtained with the cosine antenna model is slightly higher than that of the flat-top model, particularly at higher thresholds SINR ($SINR \geq -5$ dB) for $\alpha = 2$, as shown in Figure (5.4). This improvement arises because the cosine antenna model incorporates the continuous gain decay within the main lobe, thereby providing a more accurate characterization of the reduction in directional beamforming gain for small angular deviations within the main lobe compared to flat-top antenna model.

It is also important to note the limitations associated with side lobe mod-

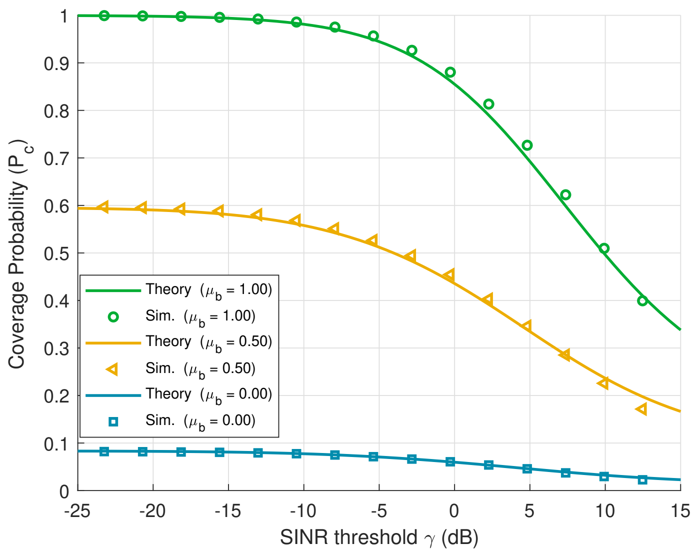

(a) P_c using cosine with discrete approximation, $K = 8$.

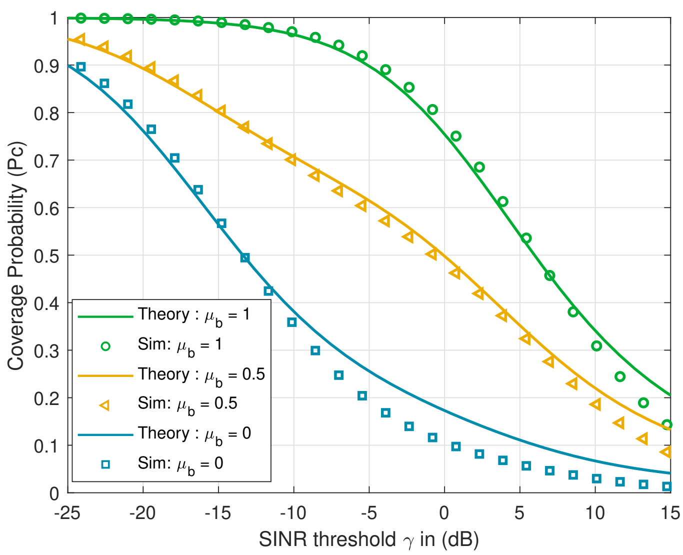

(b) P_c using the flat-top antenna model.

Figure 5.4: Comparison of coverage probability P_c vs SINR thresholds for (a) the cosine antenna model with discrete approximations and (b) using flat-top antenna model. Simulation parameters: path loss exponent $\alpha = 2$, BS transmit power $P_t = 30\,\text{dBm}$, BS beamwidth $\eta_b = 30°$.

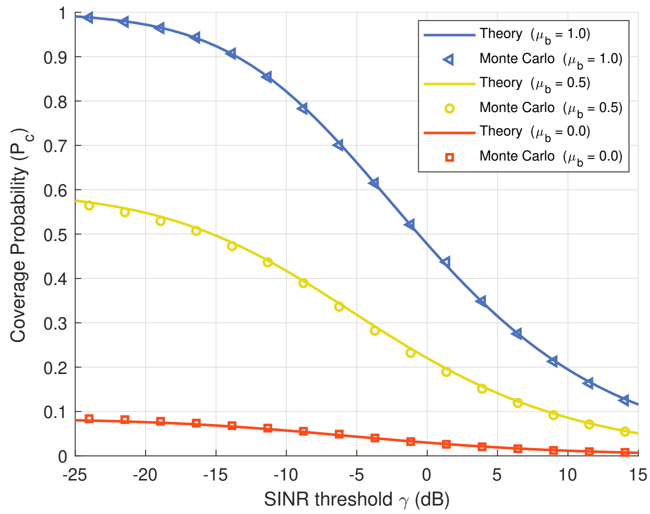

(a) P_c using cosine with discrete approximation, $K = 8$.

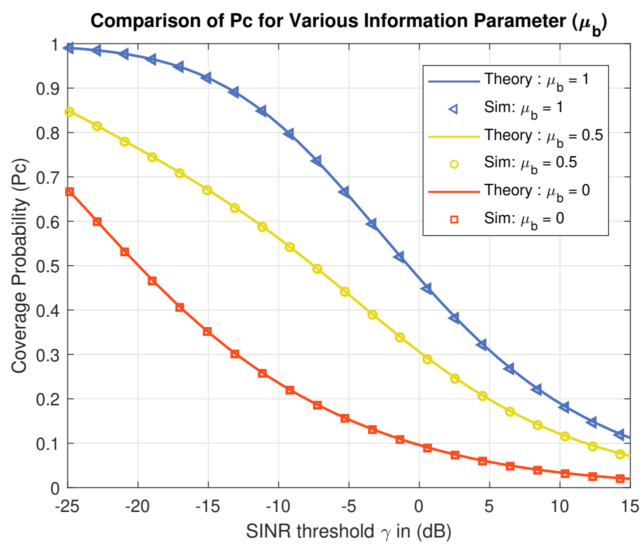

(b) P_c using the flat-top antenna model.

Figure 5.5: Comparison of coverage probability P_c vs SINR thresholds for (a) the cosine antenna model with discrete approximations and (b) using flat-top antenna model. Simulation parameters: path loss exponent $\alpha = 4$, BS transmit power $P_t = 40\,$dBm, BS beamwidth $\eta_b = 30°$.

elling in both antenna representations. The cosine antenna model neglects side lobes entirely (i.e., it assumes zero side lobe gain ($g^b = 0$)), whereas the flat-top model approximates side lobes using a constant low-gain level ($g^b \neq 0$). The absence of explicit side lobe modelling in the cosine model and the simplified side lobe representation in the flat-top model do not fully capture the angular variations of side lobes in practical antenna arrays. These simplifications may affect the accuracy of aggregate interference estimation, as practical side lobes can introduce additional interference components, potentially leading to deviations in the predicted coverage probability.

For the case of $\alpha = 4$, as shown in Figure (5.5), this improvement is less noticeable. The stronger path loss rapidly attenuates interference from distant transmitters, thereby reducing the impact of side-lobe contributions. As a result, the coverage difference between the cosine and flat-top models is smaller compared to the case of $\alpha = 2$.

The results obtained using the flat-top model provide an analytically tractable baseline for coverage analysis under different beamwidths, beam alignment information, and propagation environments ($\alpha = 2$ and $\alpha = 4$). The comparison with the cosine antenna model indicates that, although the observed differences are confined to the absolute coverage values due to the antenna gain modelling, the trends with respect to these parameters remain largely consistent across both formulations for both considered path loss exponents. This supports the use of the flat-top model for interpreting relative performance and the analytical conclusions developed in earlier chapters, while the cosine model serves as a validation framework for a more refined directional antenna gain representation.

5.5 Concluding Remarks

This chapter analyzed the coverage performance of mmWave networks using two antenna models: the cosine antenna model with a discrete gain approximation and the flat-top antenna model. The discrete cosine approximation was first validated through Monte Carlo simulations by comparing the resulting coverage probability with that obtained from the continuous cosine antenna pattern, showing that increasing the number of discrete intervals K improves the accuracy of the discrete gain relative to the continuous cosine gain, with minimal refinement beyond $K = 8$.

Coverage analysis under different beam alignment information ($\mu_b = 0, 0.5, 1$) and path loss exponents ($\alpha = 2, 4$) demonstrated that the cosine model with discrete approximation provides a more realistic representation of directional beamforming. The flat-top model tends to overestimate coverage when alignment information is partial or absent due to its assumption of a constant main-lobe gain within the beamwidth and its inability to capture the gradual antenna gain degradation caused by angular misalignment, whereas the cosine model accurately captures the gradual reduction in gain even for small angular deviations. The results also show that the cosine model yields slightly higher coverage than the flat-top model under perfect alignment information conditions, with the coverage difference being more noticeable for the path loss exponent $\alpha = 2$ than for $\alpha = 4$, as the stronger path loss rapidly attenuates interference and thus reduces the sensitivity of coverage to the antenna pattern.

These results show the impact of antenna gain modelling on the coverage probability, particularly when beam alignment errors and different propagation environments are considered. Nevertheless, comparison with the cosine antenna model indicates that the key trends obtained using the flat-top model are preserved, supporting its use as an analytically tractable framework for coverage analysis in mmWave networks.

Chapter 6

Conclusions and Future Work

6.1 Conclusions

This thesis provides an overview of the spectrum options for 6G technology in higher frequency bands, including mmWave, THz, and OWC. It examines regulatory frameworks, standardization efforts, technical features, limitations, and potential use cases of these bands. Beyond spectrum analysis, the coverage performance of mmWave networks under beam alignment errors was investigated by employing an information-aware beam alignment error model and considering two different antenna user configurations: omni-antenna and directional antenna. Furthermore, coverage performance was analyzed for two different antenna radiation pattern models (flat-top and cosine models), using a novel discrete-gain approximation approach for the cosine antenna model to facilitate analytical tractability under beam alignment errors. The key findings of the thesis can be summarized as follows.

Firstly, Chapter 2, provided a comprehensive survey and literature review of 6G spectrum options, with regulatory considerations and ongoing standardization activities. In relation to **Research Question 1**, the analysis of the review showed that the next generation of cellular networks 6G is expected to operate on a wide range of frequencies, from traditional sub-6 GHz bands to higher frequency ranges including mmWave, THz and OWC

(VLC, LiFi, OCC, FSO). Using a wide range of spectrum, especially higher-frequency bands, enables support for 6G applications demanding ultra-high data rates, massive connectivity, and low-latency services such as XR services, autonomous systems, and holographic telepresence. However, these higher-frequency bands introduce significant challenges such as severe path loss, high sensitivity to blockage, hardware complexity, and strict alignment requirements. The review's findings revealed that although THz bands offer wide bandwidth and potential to support Tbps data rates, practical barriers such as hardware constraints, antenna design challenges, and immature channel modeling currently hinder near-term large-scale adoption. By contrast, the mmWave and OWC technologies (e.g. VLC) are comparatively more mature and are expected to play a significant role in enabling early 6G deployments.

From a regulatory and standardization perspective, the review showed that although organizations such as ITU-R, 3GPP, IEEE, JEITA have initiated studies and pre-standardization for higher-frequency bands including work on frequency allocations and PHY/MAC layer requirements, but major gaps remain. For THz communications, ongoing efforts such as IEEE 802.15.3d and ITU-R studies provide an initial foundation, but complete THz channel modeling and transceiver specifications are still lacking. Similarly, OWC systems, especially FSO lack unified global standardization, with existing efforts remaining fragmented from different bodies, particularly regarding channel modeling. Furthermore, the analysis highlighted that the deployment of 6G will require a paradigm shift in spectrum management, where regulators need to re-evaluate traditional spectrum management policies and move toward developing more flexible access models, dynamic spectrum sharing mechanisms, and localized licensing tailored to emerging 6G deployment requirements.

In summary, Chapter 2 established that 6G will be enabled by a combination of mature and emerging high-frequency technologies, together with continued development in regulatory frameworks and standardization efforts to ensure efficient and practical deployment.

Chapters 3 and Chapter 4 developed an analytically tractable framework to investigate the downlink coverage probability in mmWave networks using stochastic geometry. This framework focuses on the crucial role of the beam alignment information available at the serving base station BS, by introducing an information-aware beam alignment error model, and considering two different antenna user configurations: omni-antenna and directional antenna. The analysis examined the effects of serving BS beamwidth configurations η_b, BS density λ_b, fading models, and different path loss exponents.

In relation to **Research Question 2:** The key results demonstrated clear trade-offs between beamwidth configurations and alignment information availability:

- **Wide beams ($\eta_b = 90°$):** Wide beams provide relatively stable coverage across all alignment scenarios (no information, partial information, and perfect information), their performance improves slightly as alignment information (μ_b) increases, but coverage plateaus once information exceeds a certain threshold (e.g. at $\mu_b \approx 0.4$), and increasing alignment information produces no further gain in coverage improvement beyond this threshold. The coverage plateau occurs because the wider beamwidth provides a lower main-lobe directivity gain compared with narrow beams, which limits the maximum achievable beamforming gain even under perfect alignment. Moreover, since wide beams are less sensitive to alignment errors, further improvements in alignment information provide only marginal gains once the serving link is within the main lobe. Wide beams also have the lowest ceiling for maximum achievable coverage compared to other beamwidth configurations (e.g., $\eta_b = 30°$, $\eta_b = 5°$), and only outperform under limited information. Thus, wide beams are only advantageous when alignment information is limited.

- **Medium beams ($\eta_b = 30°$):** Medium beams offer the best trade-off under partial information, as they benefit from increasing information (from partial to near-perfect), and outperform both wide and narrow beams, making them suitable for most practical deployments when perfect information is not guaranteed.
- **Narrow beams ($\eta_b = 9°, 5°$):** Narrow beams achieve the highest coverage compared to wide and medium beams, but only when near-perfect to perfect alignment information is available ($\mu_b \geq 0.98$).

These results emphasize that beamwidth selection must be aligned with the expected availability of alignment information, especially in scenarios where acquiring alignment information is challenging or resource-intensive.

Although simulation setups in Chapters 3 and Chapter 4 differ slightly, both show consistent qualitative alignment information thresholds, addressing **Research Question 3:**. Wide beams become insensitive to additional information beyond a specific threshold ($\mu_b \approx 0.4$) in both omni-user and directional user cases (see Figures (3.8) and (4.10)). Medium beams dominate for intermediate information, with thresholds ($0.3 < \mu_b \leq 0.98$) for an omni-user antenna and ($0.65 < \mu_b \leq 0.98$) for a directional user antenna. Narrow beams require ($\mu_b \geq 0.98$) in both cases.

Such thresholds can support the selection of wide, medium, and narrow beams in mmWave network design, based on the expected availability of alignment information in the deployment scenario, and can provide insight for regulatory considerations.

In relation to **Research Question 4:** The directional user antenna increases the overall coverage probability but does not alter the fundamental relationship between beamwidth and alignment information. In both antenna configurations, wide beams provide stable but lower performance, medium beams offer the best trade-off under partial alignment information, and narrow beams require near-perfect information. Thus, user antenna configurations affect the magnitude of the achieved coverage, but not the structural dependencies on alignment information.

In relation to **Research Question 5:** The cosine model yields a more realistic coverage, especially when alignment information is partial or absent, whereas the flat-top model overestimates coverage. The results also show that the cosine model yields slightly higher coverage than the flat-top model under perfect information, with the coverage difference being more noticeable for the path loss exponent $\alpha = 2$ than for $\alpha = 4$.

The results of this thesis demonstrated that mmWave coverage performance depends directly on the level of available beam alignment information, the chosen beamwidth and realistic antenna modeling. The quantitatively identified alignment information thresholds provide practical guidance for system designers and offer relevant insights for regulatory considerations in emerging 6G networks.

6.2 Future Research Directions

Future research directions in mmWave, THz, and OWC address key challenges and extend the proposed framework in several directions.

- **mmWave Communications:** Open research directions include mmWave-massive MIMO. Key challenges involve designing hybrid-analog digital beamforming architectures that approach digital beamforming performance, managing hardware cost and energy constraints, and addressing antenna numbers and channel estimation. Tackling these challenges is essential to make mmWave-massive MIMO a practical solution in 5G and future networks [199].

- **THz Communications:** Research can focus on designing compact and efficient antennas that can operate at THz frequencies, considering factors such as high path loss and atmospheric absorption [200]. Additionally, complete and flexible THz channel models are needed to capture the propagation characteristics of THz, including atmospheric absorption, scattering, and molecular absorption [201].

- **OWC:** Research can focus on developing theoretical channel models for VLC that account for the influential factors in both free-space and underwater transmission [202]. In addition, standardized FSO channel models should be established to support performance evaluation, interoperability, and optimization of FSO systems.

- **User-Side Alignment:** Extend the framework to incorporate user-side alignment information by considering directional antenna users and adopting more realistic antenna radiation patterns (e.g. 3GPP, sinc, or cosine), capturing additional sources of beam misalignment and further enhances the applicability of the framework to practical deployments.

- **Hybrid LOS/NLOS Networks:** Incorporate hybrid LOS/NLOS networks using probabilistic or spatially correlated blockage models (e.g., LOS ball or 3GPP) to analyze a wider range of propagation scenarios.

- **Emerging 6G Technologies:** Extend the framework to accommodate emerging 6G technologies, such as reconfigurable intelligent surfaces (RIS), user cooperation, and THz communications, to examine how alignment errors affect system performance in these technologies. For example, RIS-assisted links introduce reflected paths and phase alignment challenges, user cooperation requires modeling combined directional gains from multiple nodes, and THz communications involve extremely narrow beams that increase sensitivity to alignment errors.

- **Complex Deployment Scenarios:** Applying the framework to more complex deployment scenarios, including multi-tier networks and inter-operator environments. In multi-tier networks, base stations across different tiers (e.g., macro, micro, pico) differ in transmit power, density, and the level of directional information, suggesting that future work should investigate association strategies that account for both received power and beam alignment across tiers. In inter-operator scenarios, alignment errors may be correlated due to shared measurements or similar environmental conditions, and future work could examine their impact on network performance.

- **Regulatory Considerations:** Investigate how the information alignment-aware model quantifies the impact of physical-layer uncertainties (beam misalignment) on higher-layer regulatory considerations. Future work can extend the analysis by determining the information threshold required to maintain reliable beam alignment and meet QoS requirements under deployment scenarios not covered in this study, such as heterogeneous networks and inter-operator environments. This would enable the definition of minimum directional knowledge requirements for these extended deployment scenarios. Such insights can guide network design toward meeting QoS requirements and provide benchmark criteria that regulators can adopt for scalable and enforceable spectrum management strategies.

References

[1] W. K. Alsaedi, H. Ahmadi, Z. Khan, and D. Grace, "Spectrum options and allocations for 6G: A regulatory and standardization review," *IEEE Open Journal of the Communications Society*, 2023.

[2] Y. Heng, J. Mo, and J. G. Andrews, "Learning site-specific probing beams for fast mmwave beam alignment," *IEEE Transactions on Wireless Communications*, vol. 21, no. 8, pp. 5785–5800, 2022.

[3] J. Tan, T. H. Luan, W. Guan, Y. Wang, H. Peng, Y. Zhang, D. Zhao, and N. Lu, "Beam alignment in mmwave v2x communications: A survey," *IEEE Communications Surveys & Tutorials*, 2024.

[4] X. Wang, E. Turgut, and M. C. Gursoy, "Coverage in downlink heterogeneous mmwave cellular networks with user-centric small cell deployment," *IEEE Transactions on Vehicular Technology*, vol. 68, no. 4, pp. 3513–3533, 2019.

[5] M. Hussain and N. Michelusi, "Energy-efficient interactive beam alignment for millimeter-wave networks," *IEEE Transactions on Wireless Communications*, vol. 18, no. 2, pp. 838–851, 2018.

[6] Y. Xu and S. Zhou, "Coverage analyses on directional transmissions ultra-dense networks with imperfect beam alignment," *China Communications*, vol. 19, no. 5, pp. 318–328, 2022.

[7] W. Attaoui, K. Bouraqia, and E. Sabir, "Initial access & beam alignment for mmwave and terahertz communications," *IEEE Access*, vol. 10, pp. 35363–35397, 2022.

[8] L. Grannemann, A. Ichkov, P. Mähönen, and L. Simić, "Urban outdoor measurement study of phased antenna array impact on millimeter-wave link opportunities and beam misalignment," *IEEE Transactions on Wireless Communications*, vol. 20, no. 3, pp. 1727–1741, 2020.

[9] M. Xiao, S. Mumtaz, Y. Huang, L. Dai, Y. Li, M. Matthaiou, G. K. Karagiannidis, E. Björnson, K. Yang, I. Chih-Lin, *et al.*, "Millimeter wave communications for future mobile networks," *IEEE Journal on Selected Areas in Communications*, vol. 35, no. 9, pp. 1909–1935, 2017.

[10] T. Bai and R. W. Heath, "Coverage in dense millimeter wave cellular networks," in *2013 Asilomar Conference on Signals, Systems and Computers*, pp. 2062–2066, IEEE, 2013.

[11] T. Bai and R. W. Heath, "Coverage and rate analysis for millimeter-wave cellular networks," *IEEE Transactions on Wireless Communications*, vol. 14, no. 2, pp. 1100–1114, 2014.

[12] X. Yu, J. Zhang, M. Haenggi, and K. B. Letaief, "Coverage analysis for millimeter wave networks: The impact of directional antenna arrays," *IEEE Journal on Selected Areas in Communications*, vol. 35, no. 7, pp. 1498–1512, 2017.

[13] M. Cheng, J.-B. Wang, Y. Wu, X.-G. Xia, K.-K. Wong, and M. Lin, "Coverage analysis for millimeter wave cellular networks with imperfect beam alignment," *IEEE Transactions on Vehicular Technology*, vol. 67, no. 9, pp. 8302–8314, 2018.

[14] A. Thornburg and R. W. Heath, "Ergodic capacity in mmwave ad hoc network with imperfect beam alignment," in *MILCOM 2015-2015 IEEE Military Communications Conference*, pp. 1479–1484, IEEE, 2015.

[15] M. S. Zia, D. M. Blough, and M. A. Weitnauer, "Coverage in millimeter-wave networks with SNR-dependent beam alignment errors," in *2020 IEEE 91st Vehicular Technology Conference (VTC2020-Spring)*, pp. 1–5, IEEE, 2020.

[16] N. Bahadori, N. Namvar, B. Kelleyy, and A. Homaifar, "Device-to-device communications in millimeter wave band: Impact of beam alignment error," in *2019 Wireless Telecommunications Symposium (WTS)*, pp. 1–6, IEEE, 2019.

[17] J. Wildman, P. H. J. Nardelli, M. Latva-aho, and S. Weber, "On the joint impact of beamwidth and orientation error on throughput in directional wireless poisson networks," *IEEE Transactions on Wireless Communications*, vol. 13, no. 12, pp. 7072–7085, 2014.

[18] M. S. Zia, D. M. Blough, and M. A. Weitnauer, "Effects of SNR-dependent beam alignment errors on millimeter-wave cellular networks," *IEEE Transactions on Vehicular Technology*, vol. 71, no. 5, pp. 5216–5230, 2022.

[19] M. Rebato, J. Park, P. Popovski, E. De Carvalho, and M. Zorzi, "Stochastic geometric coverage analysis in mmwave cellular networks with realistic channel and antenna radiation models," *IEEE Transactions on Communications*, vol. 67, no. 5, pp. 3736–3752, 2019.

[20] I. F. Akyildiz, A. Kak, and S. Nie, "6G and beyond: The future of wireless communications systems," *IEEE Access*, vol. 8, pp. 133995–134030, 2020.

[21] W. Saad, M. Bennis, and M. Chen, "A vision of 6G wireless systems: Applications, trends, technologies, and open research problems," *IEEE network*, vol. 34, no. 3, pp. 134–142, 2019.

[22] C. De Alwis, A. Kalla, Q.-V. Pham, P. Kumar, K. Dev, W.-J. Hwang, and M. Liyanage, "Survey on 6G frontiers: Trends, applications, requirements, technologies and future research," *IEEE Open Journal of the Communications Society*, vol. 2, pp. 836–886, 2021.

[23] Y. Wu, S. Singh, T. Taleb, A. Roy, H. S. Dhillon, M. R. Kanagarathinam, and A. De, *6G mobile wireless networks*. Springer, 2021.

[24] H. Ahmadi, A. Nag, Z. Khar, K. Sayrafian, and S. Rahardja, "Networked twins and twins of networks: An overview on the relationship between digital twins and 6G," *IEEE Communications Standards Magazine*, vol. 5, no. 4, pp. 154–160, 2021.

[25] M. Z. Chowdhury, M. Shahjalal, S. Ahmed, and Y. M. Jang, "6G wireless communication systems: Applications, requirements, technologies, challenges, and research directions," *IEEE Open Journal of the Communications Society*, vol. 1, pp. 957–975, 2020.

[26] F. Tariq, M. R. Khandaker, K.-K. Wong, M. A. Imran, M. Bennis, and M. Debbah, "A speculative study on 6G," *IEEE Wireless Communications*, vol. 27, no. 4, pp. 118–125, 2020.

[27] W. Jiang, B. Han, M. A. Habibi, and H. D. Schotten, "The road towards 6G: A comprehensive survey," *IEEE Open Journal of the Communications Society*, vol. 2, pp. 334–366, 2021.

[28] B. Zong, C. Fan, X. Wang, X. Duan, B. Wang, and J. Wang, "6G technologies: Key drivers, core requirements, system architectures, and enabling technologies," *IEEE Vehicular Technology Magazine*, vol. 14, no. 3, pp. 18–27, 2019.

[29] K. B. Letaief, W. Chen, Y. Shi, J. Zhang, and Y.-J. A. Zhang, "The roadmap to 6G: AI empowered wireless networks," *IEEE communications magazine*, vol. 57, no. 8, pp. 84–90, 2019.

[30] K. B. Letaief, Y. Shi, J. Lu, and J. Lu, "Edge artificial intelligence for 6G: Vision, enabling technologies, and applications," *IEEE Journal on Selected Areas in Communications*, vol. 40, no. 1, pp. 5–36, 2021.

[31] S. Chen, Y.-C. Liang, S. Sun, S. Kang, W. Cheng, and M. Peng, "Vision, requirements, and technology trend of 6G: How to tackle the challenges of system coverage, capacity, user data-rate and movement speed," *IEEE Wireless Communications*, vol. 27, no. 2, pp. 218–228, 2020.

[32] G. K. Papageorgiou, K. Voulgaris, K. Ntougias, D. K. Ntaikos, M. M. Butt, C. Galiotto, N. Marchetti, V. Frascolla, H. Annouar, A. Gomes, *et al.*, "Advanced dynamic spectrum 5g mobile networks employing licensed shared access," *IEEE Communications Magazine*, vol. 58, no. 7, pp. 21–27, 2020.

[33] W. Lehr, F. Queder, and J. Haucap, "5G: A new future for mobile network operators, or not?," *Telecommunications Policy*, vol. 45, no. 3, p. 102086, 2021.

[34] S. G. . S. . ITU, "Spectrum management." `https://www.itu.int/en/ITU-R/study-groups/rsg1/Pages/default.aspx`. (accessed: February 26, 2023).

[35] F. Beltrán, "Accelerating the introduction of spectrum sharing using market-based mechanisms," *IEEE Communications Standards Magazine*, vol. 1, no. 3, pp. 66–72, 2017.

[36] M. Matinmikko-Blue, S. Yrjölä, and P. Ahokangas, "Spectrum management in the 6G era: The role of regulation and spectrum sharing," in *2020 2nd 6G Wireless Summit (6G SUMMIT)*, pp. 1–5, IEEE, 2020.

[37] M. Matinmikko-Blue, "Sustainability and spectrum management in the 6G era," in *2021 ITU Kaleidoscope: Connecting Physical and Virtual Worlds (ITU K)*, pp. 1–9, IEEE, 2021.

[38] A. Kuś and M. Massaro, "Analysing the C-band spectrum auctions for 5G in europe: Achieving efficiency and fair decisions in radio spectrum management," *Telecommunications Policy*, vol. 46, no. 4, p. 102286, 2022.

[39] M. Matinmikko-Blue, S. Yrjölä, V. Seppänen, P. Ahokangas, H. Hämmäinen, and M. Latva-Aho, "Analysis of spectrum valuation elements for local 5g networks: Case study of 3.5-GHz band," *IEEE Transactions on Cognitive Communications and Networking*, vol. 5, no. 3, pp. 741–753, 2019.

[40] A. Ponomarenko-Timofeev, A. Pyattaev, S. Andreev, Y. Koucheryavy, M. Mueck, and I. Karls, "Highly dynamic spectrum management within licensed shared access regulatory framework," *IEEE Communications Magazine*, vol. 54, no. 3, pp. 100–109, 2016.

[41] M. Massaro, "Next generation of radio spectrum management: Licensed shared access for 5G," *Telecommunications Policy*, vol. 41, no. 5-6, pp. 422–433, 2017.

[42] A. Chandra, "Spectrum management for future generation wireless based technology," in *2009 European Wireless Technology Conference*, pp. 201–205, IEEE, 2009.

[43] H. Ahmadi, I. Macaluso, I. Gomez, L. DaSilva, and L. Doyle, "Virtualization of spatial streams for enhanced spectrum sharing," in *2016 IEEE Global Communications Conference (GLOBECOM)*, pp. 1–6, 2016.

[44] J. Hwang and H. Yoon, "A mixed spectrum management framework for the future wireless service based on techno-economic analysis: The korean spectrum policy study," *Telecommunications Policy*, vol. 33, no. 8, pp. 407–421, 2009.

[45] H. Ahmadi, I. Macaluso, I. Gomez, L. Doyle, and L. A. DaSilva, "Substitutability of spectrum and cloud-based antennas in virtualized wireless networks," *IEEE Wireless Communications*, vol. 24, no. 2, pp. 114–120, 2017.

[46] R. Jain, "Spectrum auctions in india: lessons from experience," *Telecommunications Policy*, vol. 25, no. 10-11, pp. 671–688, 2001.

[47] M. Park, S.-W. Lee, and Y.-J. Choi, "Does spectrum auctioning harm consumers? lessons from 3G licensing," *Information Economics and Policy*, vol. 23, no. 1, pp. 118–126, 2011.

[48] H. Ahmadi, Y. H. Chew, N. Reyhani, C. C. Chai, and L. A. DaSilva, "Learning solutions for auction-based dynamic spectrum access in multicarrier systems," *Computer Networks*, vol. 67, pp. 60–73, 2014.

[49] H. Vuojala, M. Mustonen, X. Chen, K. Kujanpää, P. Ruuska, M. Höyhtyä, M. Matinmikko-Blue, J. Kalliovaara, P. Talmola, and A.-G. Nyström, "Spectrum access options for vertical network service providers in 5G," *Telecommunications Policy*, vol. 44, no. 4, p. 101903, 2020.

[50] A. Kliks, O. Holland, A. Basaure, and M. Matinmikko, "Spectrum and license flexibility for 5G networks," *IEEE Communications Magazine*, vol. 53, no. 7, pp. 42–49, 2015.

[51] J. Khun-Jush, P. Bender, B. Deschamps, and M. Gundlach, "Licensed shared access as complementary approach to meet spectrum demands: Benefits for next generation cellular systems," in *ETSI Workshop on reconfigurable radio systems*, 2012.

[52] J. Jeon, "NR wide bandwidth operations," *IEEE Communications Magazine*, vol. 56, no. 3, pp. 42–46, 2018.

[53] F. Beltran, S. K. Ray, and J. A. Gutiérrez, "Understanding the current operation and future roles of wireless networks: Co-existence, competition and co-operation in the unlicensed spectrum bands," *IEEE Journal on Selected Areas in Communications*, vol. 34, no. 11, pp. 2829–2837, 2016.

[54] R. Dilli, "Analysis of 5G wireless systems in FR1 and FR2 frequency bands," in *2020 2nd International Conference on Innovative Mechanisms for Industry Applications (ICIMIA)*, pp. 767–772, IEEE, 2020.

[55] S. Lagen, L. Giupponi, S. Goyal, N. Patriciello, B. Bojović, A. Demir, and M. Beluri, "New radio beam-based access to unlicensed spectrum: Design challenges and solutions," *IEEE Communications Surveys & Tutorials*, vol. 22, no. 1, pp. 8–37, 2019.

[56] A. M. Voicu, L. Simić, and M. Petrova, "Survey of spectrum sharing for inter-technology coexistence," *IEEE Communications Surveys & Tutorials*, vol. 21, no. 2, pp. 1112–1144, 2018.

[57] F. A. De Figueiredo, X. Jiao, W. Liu, R. Mennes, I. Jabandzić, and I. Moerman, "A spectrum sharing framework for intelligent next generation wireless networks," *IEEE Access*, vol. 6, pp. 60704–60735, 2018.

[58] P. Wang, B. Di, and L. Song, "Cellular communications over unlicensed mmwave bands with hybrid beamforming," *IEEE Transactions on Wireless Communications*, vol. 21, no. 8, pp. 6064–6078, 2022.

[59] L. Zhang, M. Xiao, G. Wu, M. Alam, Y.-C. Liang, and S. Li, "A survey of advanced techniques for spectrum sharing in 5G networks," *IEEE Wireless Communications*, vol. 24, no. 5, pp. 44–51, 2017.

[60] L. Zhang, Y.-C. Liang, and M. Xiao, "Spectrum sharing for internet of things: A survey," *IEEE Wireless Communications*, vol. 26, no. 3, pp. 132–139, 2018.

[61] M. Massaro and F. Beltrán, "Will 5G lead to more spectrum sharing? discussing recent developments of the LSA and the CBRS spectrum sharing frameworks," *Telecommunications Policy*, vol. 44, no. 7, p. 101973, 2020.

[62] A. Medeisis and V. V. Fomin, "Radio spectrum management as a system of innovation: LSA case study," in *2022 IEEE Open Conference of Electrical, Electronic and Information Sciences (eStream)*, pp. 1–6, IEEE, 2022.

[63] M. Matinmikko, H. Okkonen, M. Palola, S. Yrjola, P. Ahokangas, and M. Mustonen, "Spectrum sharing using licensed shared access: the concept and its workflow for lte-advanced networks," *IEEE Wireless Communications*, vol. 21, no. 2, pp. 72–79, 2014.

[64] C. Sexton, N. J. Kaminski, J. M. Marquez-Barja, N. Marchetti, and L. A. DaSilva, "5g: Adaptable networks enabled by versatile radio access technologies," *IEEE Communications Surveys & Tutorials*, vol. 19, no. 2, pp. 688–720, 2017.

[65] S. Bhattarai, J.-M. J. Park, B. Gao, K. Bian, and W. Lehr, "An overview of dynamic spectrum sharing: Ongoing initiatives, challenges, and a roadmap for future research," *IEEE Transactions on Cognitive Communications and Networking*, vol. 2, no. 2, pp. 110–128, 2016.

[66] M. Mustonen, M. Matinmikko, O. Holland, and D. Roberson, "Process model for recent spectrum sharing concepts in policy making," *Telecommunications Policy*, vol. 41, no. 5-6, pp. 391–404, 2017.

[67] V. Frascolla, A. J. Morgado, A. Gomes, M. M. Butt, N. Marchetti, K. Voulgaris, and C. B. Papadias, "Dynamic licensed shared access-a new architecture and spectrum allocation techniques," in *2016 IEEE 84th Vehicular Technology Conference (VTC-Fall)*, pp. 1–5, IEEE, 2016.

[68] S. K. Sharma, T. E. Bogale, L. B. Le, S. Chatzinotas, X. Wang, and B. Ottersten, "Dynamic spectrum sharing in 5g wireless networks with full-duplex technology: Recent advances and research challenges," *IEEE Communications Surveys & Tutorials*, vol. 20, no. 1, pp. 674–707, 2017.

[69] M. Mustonen, M. Matinmikko, M. Palola, S. Yrjölä, J. Paavola, A. Kivinen, and J. Engelberg, "Considerations on the licensed shared access (LSA) architecture from the incumbent perspective," in *2014 9th International Conference on Cognitive Radio Oriented Wireless Networks and Communications (CROWNCOM)*, pp. 150–155, IEEE, 2014.

[70] M. Parvini, A. H. Zarif, A. Nouruzi, N. Mokari, M. R. Javan, B. Abbasi, A. Ghasemi, and H. Yanikomeroglu, "A comprehensive survey of spectrum sharing schemes from a standardization and implementation perspective," *arXiv preprint arXiv:2203.11125*, 2022.

[71] M. Matinmikko, M. Latva-aho, P. Ahokangas, and V. Seppänen, "On regulations for 5G: Micro licensing for locally operated networks," *Telecommunications Policy*, vol. 42, no. 8, pp. 622–635, 2018.

[72] R. K. Saha, "Approaches to improve millimeter-wave spectrum utilization using indoor small cells in multi-operator environments toward 6G," *IEEE Access*, vol. 8, pp. 207643–207658, 2020.

[73] A. J. Morgado, F. B. Saghezchi, S. Mumtaz, V. Frascolla, J. Rodriguez, and I. Otung, "A novel machine learning-based scheme for spectrum sharing in virtualized 5G networks," *IEEE Transactions on Intelligent Transportation Systems*, vol. 23, no. 10, pp. 19691–19703, 2022.

[74] W. Chen, J. Montojo, J. Lee, M. Shafi, and Y. Kim, "The standardization of 5G-advanced in 3GPP," *IEEE Communications Magazine*, 2022.

[75] J. Pérez-Romero, O. Sallent, H. Ahmadi, and I. Macaluso, "On modeling channel selection in lte-u as a repeated game," in *2016 IEEE Wireless Communications and Networking Conference*, pp. 1–6, 2016.

[76] R. H. Tehrani, S. Vahid, D. Triantafyllopoulou, H. Lee, and K. Moessner, "Licensed spectrum sharing schemes for mobile operators: A survey and outlook," *IEEE Communications Surveys & Tutorials*, vol. 18, no. 4, pp. 2591–2623, 2016.

[77] W. Zhang, J. Yang, G. Zhang, L. Yang, and C. Kiat Yeo, "Tv white space and its applications in future wireless networks and communications: A survey," *IET Communications*, vol. 12, no. 20, pp. 2521–2532, 2018.

[78] Y. Ma, Y. Gao, C. Fu, W. Rong, Z. Xiong, and S. Cui, "Tv white space spectrum analysis based on machine learning," *Journal of Communications and Information Networks*, vol. 4, no. 2, pp. 68–80, 2019.

[79] A. Medeisis, V. Fomin, and W. Webb, "Untangling the paradox of licensed shared access: Need for regulatory refocus," *Telecommunications Policy*, p. 102380, 2022.

[80] Z. Zhang, Y. Xiao, Z. Ma, M. Xiao, Z. Ding, X. Lei, G. K. Karagiannidis, and P. Fan, "6G wireless networks: Vision, requirements, architecture, and key technologies," *IEEE Vehicular Technology Magazine*, vol. 14, no. 3, pp. 28–41, 2019.

[81] G. Gür, "Expansive networks: Exploiting spectrum sharing for capacity boost and 6G vision," *Journal of Communications and Networks*, vol. 22, no. 6, pp. 444–454, 2020.

[82] P. Yang, L. Kong, and G. Chen, "Spectrum sharing for 5g/6g urllc: Research frontiers and standards," *IEEE communications standards magazine*, vol. 5, no. 2, pp. 120–125, 2021.

[83] E. D. Pascale, H. Ahmadi, L. Doyle, and I. Macaluso, "Toward scalable user-deployed ultra-dense networks: Blockchain-enabled small cells as a service," *IEEE Communications Magazine*, vol. 58, no. 8, pp. 82–88, 2020.

[84] V. Haghighatdoost, S. Khorsandi, and H. Ahmadi, "Fair pricing in heterogeneous internet-of-things wireless access networks using crowdsourcing," *IEEE Internet of Things Journal*, vol. 8, no. 7, pp. 5710–5721, 2021.

[85] S. Sargunavathi, V. Vijayalakshmi, D. Shobana, *et al.*, "Enhancement of 5g ultra-reliable low-latency communication: Application of edge computing and ai-based approaches," in *2025 IEEE 2nd International Conference on Information Technology, Electronics and Intelligent Communication Systems (ICITEICS)*, pp. 1–6, IEEE, 2025.

[86] S. S. Sefati, A. U. Haq, R. Craciunescu, S. Halunga, A. Mihovska, O. Fratu, *et al.*, "A comprehensive survey on resource management

in 6g network based on internet of things," *IEEE access*, vol. 12, pp. 113741–113784, 2024.

[87] M. Adhikari and A. Hazra, "6g-enabled ultra-reliable low-latency communication in edge networks," *IEEE Communications Standards Magazine*, vol. 6, no. 1, pp. 67–74, 2022.

[88] H. Viswanathan and P. E. Mogensen, "Communications in the 6G era," *IEEE Access*, vol. 8, pp. 57063–57074, 2020.

[89] S. Iyer, A. Patil, S. Bhairanatti, S. Halagatti, and R. J. Pandya, "A survey on technological trends to enhance spectrum-efficiency in 6G communications," *Transactions of the Indian National Academy of Engineering*, pp. 1–28, 2022.

[90] P. Yang, Y. Xiao, M. Xiao, and S. Li, "6G wireless communications: Vision and potential techniques," *IEEE network*, vol. 33, no. 4, pp. 70–75, 2019.

[91] M. Giordani, M. Polese, M. Mezzavilla, S. Rangan, and M. Zorzi, "Toward 6G networks: Use cases and technologies," *IEEE Communications Magazine*, vol. 58, no. 3, pp. 55–61, 2020.

[92] A. Slalmi, H. Chaibi, A. Chehri, R. Saadane, and G. Jeon, "Toward 6G: Understanding network requirements and key performance indicators," *Transactions on Emerging Telecommunications Technologies*, vol. 32, no. 3, p. e4201, 2021.

[93] L. Zhu, Z. Xiao, X.-G. Xia, and D. O. Wu, "Millimeter-wave communications with non-orthogonal multiple access for b5g/6G," *IEEE Access*, vol. 7, pp. 116123–116132, 2019.

[94] M. Shafi, A. F. Molisch, P. J. Smith, T. Haustein, P. Zhu, P. De Silva, F. Tufvesson, A. Benjebbour, and G. Wunder, "5g: A tutorial overview of standards, trials, challenges, deployment, and practice," *IEEE journal on selected areas in communications*, vol. 35, no. 6, pp. 1201–1221, 2017.

[95] L. Wei, R. Q. Hu, Y. Qian, and G. Wu, "Key elements to enable millimeter wave communications for 5G wireless systems," *IEEE Wireless Communications*, vol. 21, no. 6, pp. 136–143, 2014.

[96] N. Al-Falahy and O. Y. Alani, "Millimetre wave frequency band as a candidate spectrum for 5G network architecture: A survey," *Physical Communication*, vol. 32, pp. 120–144, 2019.

[97] S. He, Y. Zhang, J. Wang, J. Zhang, J. Ren, Y. Zhang, W. Zhuang, and X. Shen, "A survey of millimeter-wave communication: Physical-layer technology specifications and enabling transmission technologies," *Proceedings of the IEEE*, vol. 109, no. 10, pp. 1666–1705, 2021.

[98] A. Morgado, K. M. S. Huq, S. Mumtaz, and J. Rodriguez, "A survey of 5G technologies: regulatory, standardization and industrial perspectives," *Digital Communications and Networks*, vol. 4, no. 2, pp. 87–97, 2018.

[99] J. Lee, E. Tejedor, K. Ranta-aho, H. Wang, K.-T. Lee, E. Semaan, E. Mohyeldin, J. Song, C. Bergljung, and S. Jung, "Spectrum for 5G: Global status, challenges, and enabling technologies," *IEEE Communications Magazine*, vol. 56, no. 3, pp. 12–18, 2018.

[100] A. N. Uwaechia and N. M. Mahyuddin, "A comprehensive survey on millimeter wave communications for fifth-generation wireless networks: Feasibility and challenges," *IEEE Access*, vol. 8, pp. 62367–62414, 2020.

[101] X. Wang, L. Kong, F. Kong, F. Qiu, M. Xia, S. Arnon, and G. Chen, "Millimeter wave communication: A comprehensive survey," *IEEE Communications Surveys & Tutorials*, vol. 20, no. 3, pp. 1616–1653, 2018.

[102] L. Bariah, L. Mohjazi, S. Muhaidat, P. C. Sofotasios, G. K. Kurt, H. Yanikomeroglu, and O. A. Dobre, "A prospective look: Key enabling technologies, applications and open research topics in 6G networks," *IEEE access*, vol. 8, pp. 174792–174820, 2020.

[103] W. Jiang and H. D. Schotten, "Initial beamforming for millimeter-wave and terahertz communications in 6G mobile systems," in *2022 IEEE Wireless Communications and Networking Conference (WCNC)*, pp. 2613–2618, IEEE, 2022.

[104] R. Hasan, M. M. Mowla, M. A. Rashid, M. K. Hosain, and I. Ahmad, "A statistical analysis of channel modeling for 5G mmwave communications," in *2019 International Conference on Electrical, Computer and Communication Engineering (ECCE)*, pp. 1–6, IEEE, 2019.

[105] M. Giordani, M. Polese, A. Roy, D. Castor, and M. Zorzi, "Standalone and non-standalone beam management for 3GPP NR at mmWaves," *IEEE Communications Magazine*, vol. 57, no. 4, pp. 123–129, 2019.

[106] Y. Niu, Y. Li, D. Jin, L. Su, and A. V. Vasilakos, "A survey of millimeter wave communications (mmWave) for 5G: opportunities and challenges," *Wireless networks*, vol. 21, no. 8, pp. 2657–2676, 2015.

[107] W. Hong, Z. H. Jiang, C. Yu, D. Hou, H. Wang, C. Guo, Y. Hu, L. Kuai, Y. Yu, Z. Jiang, *et al.*, "The role of millimeter-wave technologies in 5G/6G wireless communications," *IEEE Journal of Microwaves*, vol. 1, no. 1, pp. 101–122, 2021.

[108] Y.-N. R. Li, B. Gao, X. Zhang, and K. Huang, "Beam management in millimeter-wave communications for 5G and beyond," *IEEE Access*, vol. 8, pp. 13282–13293, 2020.

[109] N. Patriciello, S. Lagén, B. Bojović, and L. Giupponi, "NR-U and ieee 802.11 technologies coexistence in unlicensed mmwave spectrum: Models and evaluation," *IEEE access*, vol. 8, pp. 71254–71271, 2020.

[110] D. Moltchanov, E. Sopin, V. Begishev, A. Samuylov, Y. Koucheryavy, and K. Samouylov, "A tutorial on mathematical modeling of 5G/6G millimeter wave and terahertz cellular systems," *IEEE Communications Surveys & Tutorials*, 2022.

[111] Y. Kim, Y. Kim, J. Oh, H. Ji, J. Yeo, S. Choi, H. Ryu, H. Noh, T. Kim, F. Sun, *et al.*, "New radio (nr) and its evolution toward 5G-advanced," *IEEE Wireless Communications*, vol. 26, no. 3, pp. 2–7, 2019.

[112] H.-G. Song, K. Park, J.-Y. Park, T.-H. Kwon, J.-S. Seo, and S.-W. Jeon, "5G NR performance evaluation under phase noise distortion for 52.6 ghz to 71 ghz," in *2021 International Conference on Information and Communication Technology Convergence (ICTC)*, pp. 607–610, IEEE, 2021.

[113] X. Lin, "An overview of 5G advanced evolution in 3gpp release 18," *IEEE Communications Standards Magazine*, vol. 6, no. 3, pp. 77–83, 2022.

[114] M. Hirzallah, M. Krunz, B. Kecicioglu, and B. Hamzeh, "5G new radio unlicensed: Challenges and evaluation," *IEEE Transactions on Cognitive Communications and Networking*, vol. 7, no. 3, pp. 689–701, 2020.

[115] R. K. Saha, "Coexistence of cellular and IEEE 802.11 technologies in unlicensed spectrum bands-a survey," *IEEE Open Journal of the Communications Society*, vol. 2, pp. 1996–2028, 2021.

[116] S. Tripathi, N. V. Sabu, A. K. Gupta, and H. S. Dhillon, "Millimeter-wave and terahertz spectrum for 6G wireless," in *6G Mobile Wireless Networks*, pp. 83–121, Springer, 2021.

[117] C. Seker, M. T. Güneser, and T. Ozturk, "A review of millimeter wave communication for 5G," in *2018 2nd International Symposium on Multidisciplinary Studies and Innovative Technologies (ISMSIT)*, pp. 1–5, Ieee, 2018.

[118] T. Sharma, A. Chehri, and P. Fortier, "Review of optical and wireless backhaul networks and emerging trends of next generation 5G and 6G technologies," *Transactions on Emerging Telecommunications Technologies*, vol. 32, no. 3, p. e4155, 2021.

[119] T. S. Rappaport, Y. Xing, G. R. MacCartney, A. F. Molisch, E. Mellios, and J. Zhang, "Overview of millimeter wave communications for fifth-generation (5G) wireless networks—with a focus on propagation models," *IEEE Transactions on antennas and propagation*, vol. 65, no. 12, pp. 6213–6230, 2017.

[120] I. Rasheed, F. Hu, Y.-K. Hong, and B. Balasubramanian, "Intelligent vehicle network routing with adaptive 3D beam alignment for mmwave 5G-based V2X communications," *IEEE Transactions on Intelligent Transportation Systems*, vol. 22, no. 5, pp. 2706–2718, 2020.

[121] R. W. Heath, N. Gonzalez-Prelcic, S. Rangan, W. Roh, and A. M. Sayeed, "An overview of signal processing techniques for millimeter wave MIMO systems," *IEEE journal of selected topics in signal processing*, vol. 10, no. 3, pp. 436–453, 2016.

[122] M. Alsabah, M. A. Naser, B. M. Mahmmod, S. H. Abdulhussain, M. R. Eissa, A. Al-Baidhani, N. K. Noordin, S. M. Sait, K. A. Al-Utaibi, and F. Hashim, "6G wireless communications networks: A comprehensive survey," *IEEE Access*, vol. 9, pp. 148191–148243, 2021.

[123] A. Y. Pawar, D. D. Sonawane, K. B. Erande, and D. V. Derle, "Terahertz technology and its applications," *Drug invention today*, vol. 5, no. 2, pp. 157–163, 2013.

[124] Z. Qadir, K. N. Le, N. Saeed, and H. S. Munawar, "Towards 6G internet of things: Recent advances, use cases, and open challenges," *ICT Express*, 2022.

[125] I. F. Akyildiz, J. M. Jornet, and C. Han, "Teranets: Ultra-broadband communication networks in the terahertz band," *IEEE Wireless Communications*, vol. 21, no. 4, pp. 130–135, 2014.

[126] C. Chaccour, M. N. Soorki, W. Saad, M. Bennis, P. Popovski, and M. Debbah, "Seven defining features of terahertz (THz) wireless systems: A fellowship of communication and sensing," *IEEE Communications Surveys & Tutorials*, vol. 24, no. 2, pp. 967–993, 2022.

[127] I. F. Akyildiz, C. Han, Z. Hu, S. Nie, and J. M. Jornet, "Terahertz band communication: An old problem revisited and research directions for the next decade," *IEEE Transactions on Communications*, 2022.

[128] K. M. S. Huq, S. A. Busari, J. Rodriguez, V. Frascolla, W. Bazzi, and D. C. Sicker, "Terahertz-enabled wireless system for beyond-5G ultra-fast networks: A brief survey," *IEEE network*, vol. 33, no. 4, pp. 89–95, 2019.

[129] V. Petrov, T. Kurner, and I. Hosako, "IEEE 802.15. 3d: First standardization efforts for sub-terahertz band communications toward 6G," *IEEE Communications Magazine*, vol. 58, no. 11, pp. 28–33, 2020.

[130] L. Zhang, X. Pang, S. Jia, S. Wang, and X. Yu, "Beyond 100 Gb/s optoelectronic terahertz communications: Key technologies and directions," *IEEE Communications Magazine*, vol. 58, no. 11, pp. 34–40, 2020.

[131] T. Kürner and A. Hirata, "On the impact of the results of WRC 2019 on THz communications," in *2020 Third International Workshop on Mobile Terahertz Systems (IWMTS)*, pp. 1–3, IEEE, 2020.

[132] B. Ji, Y. Han, S. Liu, F. Tao, G. Zhang, Z. Fu, and C. Li, "Several key technologies for 6G: challenges and opportunities," *IEEE Communications Standards Magazine*, vol. 5, no. 2, pp. 44–51, 2021.

[133] Z. Chen, X. Ma, B. Zhang, Y. Zhang, Z. Niu, N. Kuang, W. Chen, L. Li, and S. Li, "A survey on terahertz communications," *China Communications*, vol. 16, no. 2, pp. 1–35, 2019.

[134] D. P. M. Osorio, I. Ahmad, J. D. V. Sánchez, A. Gurtov, J. Scholliers, M. Kutila, and P. Porambage, "Towards 6g-enabled internet of vehicles: Security and privacy," *IEEE Open Journal of the Communications Society*, vol. 3, pp. 82–105, 2022.

[135] M. M. Azari, S. Solanki, S. Chatzinotas, and M. Bennis, "THz-empowered UAVs in 6G: Opportunities, challenges, and trade-offs," *IEEE Communications Magazine*, vol. 60, no. 5, pp. 24–30, 2022.

[136] Y. Lu and X. Zheng, "6G: A survey on technologies, scenarios, challenges, and the related issues," *Journal of Industrial Information Integration*, vol. 19, p. 100158, 2020.

[137] D. Serghiou, M. Khalily, T. W. Brown, and R. Tafazolli, "Terahertz channel propagation phenomena, measurement techniques and modeling for 6G wireless communication applications: a survey, open challenges and future research directions," *IEEE Communications Surveys & Tutorials*, 2022.

[138] A. Shahraki, M. Abbasi, M. Piran, A. Taherkordi, *et al.*, "A comprehensive survey on 6G networks: Applications, core services, enabling technologies, and future challenges," *arXiv preprint arXiv:2101.12475*, 2021.

[139] S. Idris, U. Mohammed, J. Sanusi, and S. Thomas, "Visible light communication: A potential 5G and beyond communication technology," in *2019 15th International Conference on Electronics, Computer and Computation (ICECCO)*, pp. 1–6, IEEE, 2019.

[140] M. Xiong, Q. Liu, X. Wang, S. Zhou, B. Zhou, and Z. Bu, "Mobile optical communications using second harmonic of intra-cavity laser," *IEEE Transactions on Wireless Communications*, vol. 21, no. 5, pp. 3222–3231, 2021.

[141] A. E. Ibhaze, P. E. Orukpe, and F. O. Edeko, "High capacity data rate system: Review of visible light communications technology," *Journal of Electronic Science and Technology*, vol. 18, no. 3, p. 100055, 2020.

[142] M. Z. Chowdhury, M. T. Hossan, A. Islam, and Y. M. Jang, "A comparative survey of optical wireless technologies: Architectures and applications," *ieee Access*, vol. 6, pp. 9819–9840, 2018.

[143] A. Jahid, M. H. Alsharif, and T. J. Hall, "A contemporary survey on free space optical communication: Potentials, technical challenges, recent advances and research direction," *Journal of Network and Computer Applications*, p. 103311, 2022.

[144] M. Z. Chowdhury, M. K. Hasan, M. Shahjalal, M. T. Hossan, and Y. M. Jang, "Optical wireless hybrid networks: Trends, opportunities,

challenges, and research directions," *IEEE Communications Surveys & Tutorials*, vol. 22, no. 2, pp. 930–966, 2020.

[145] M. Ndiaye, A. M. Saley, K. Niane, and A. Raimy, "Future 6G communication networks: Typical IoT network topology and terahertz frequency challenges and research issues," in *2022 2nd International Conference on Innovative Research in Applied Science, Engineering and Technology (IRASET)*, pp. 1–5, IEEE, 2022.

[146] D. Karunatilaka, F. Zafar, V. Kalavally, and R. Parthiban, "Led based indoor visible light communications: State of the art," *IEEE communications surveys & tutorials*, vol. 17, no. 3, pp. 1649–1678, 2015.

[147] N. Saeed, S. Guo, K.-H. Park, T. Y. Al-Naffouri, and M.-S. Alouini, "Optical camera communications: Survey, use cases, challenges, and future trends," *Physical Communication*, vol. 37, p. 100900, 2019.

[148] O. Ergul, E. Dinc, and O. B. Akan, "Communicate to illuminate: State-of-the-art and research challenges for visible light communications," *Physical Communication*, vol. 17, pp. 72–85, 2015.

[149] O. Alsulami, A. T. Hussein, M. T. Alresheedi, and J. M. Elmirghani, "Optical wireless communication systems, a survey," *arXiv preprint arXiv:1812.11544*, 2018.

[150] S. Vappangi and V. Mani, "A survey on the integration of visible light communication with power line communication: Conception, applications and research challenges," *Optik*, p. 169582, 2022.

[151] L. U. Khan, "Visible light communication: Applications, architecture, standardization and research challenges," *Digital Communications and Networks*, vol. 3, no. 2, pp. 78–88, 2017.

[152] A.-M. Cailean and M. Dimian, "Impact of IEEE 802.15. 7 standard on visible light communications usage in automotive applications," *IEEE Communications Magazine*, vol. 55, no. 4, pp. 169–175, 2017.

[153] S. Rajagopal, R. D. Roberts, and S.-K. Lim, "IEEE 802.15. 7 visible light communication: modulation schemes and dimming support," *IEEE Communications Magazine*, vol. 50, no. 3, pp. 72–82, 2012.

[154] P. Namonta and P. Cherntanomwong, "Real time vital sign transmission using IEEE 802.15. 7 VLC PHY-I transceiver," in *2017 International Electrical Engineering Congress (iEECON)*, pp. 1–4, IEEE, 2017.

[155] H. Haas, "LiFi is a paradigm-shifting 5G technology," *Reviews in Physics*, vol. 3, pp. 26–31, 2018.

[156] M. Popadić and E. Kočan, "LiFi networks: Concept, standardization activities and perspectives," in *2021 25th International Conference on Information Technology (IT)*, pp. 1–4, IEEE, 2021.

[157] B. Béchadergue and B. Azoulay, "An industrial view on LiFi challenges and future," in *2020 12th International Symposium on Communication Systems, Networks and Digital Signal Processing (CSNDSP)*, pp. 1–6, IEEE, 2020.

[158] E. Khorov and I. Levitsky, "Current status and challenges of Li-Fi: IEEE 802.11 bb," *IEEE Communications Standards Magazine*, vol. 6, no. 2, pp. 35–41, 2022.

[159] A. A. Purwita and H. Haas, "Studies of flatness of LiFi channel for IEEE 802.11 bb," in *2020 IEEE Wireless Communications and Networking Conference (WCNC)*, pp. 1–6, IEEE, 2020.

[160] H. Haas and T. Cogalan, "LiFi opportunities and challenges," in *2019 16th International Symposium on Wireless Communication Systems (ISWCS)*, pp. 361–366, IEEE, 2019.

[161] S. A. H. Mohsan, A. Mazinani, H. B. Sadiq, and H. Amjad, "A survey of optical wireless technologies: Practical considerations, impairments, security issues and future research directions," *Optical and Quantum Electronics*, vol. 54, no. 3, p. 187, 2022.

[162] M. K. Hasan, M. O. Ali, M. H. Rahman, M. Z. Chowdhury, and Y. M. Jang, "Optical camera communication in vehicular applications: A review," *IEEE Transactions on Intelligent Transportation Systems*, 2021.

[163] S. A. Al-Gailani, M. F. M. Salleh, A. A. Salem, R. Q. Shaddad, U. U. Sheikh, N. A. Algeelani, and T. A. Almohamad, "A survey of free space optics (FSO) communication systems, links, and networks," *IEEE Access*, vol. 9, pp. 7353–7373, 2020.

[164] M. A. Khalighi and M. Uysal, "Survey on free space optical communication: A communication theory perspective," *IEEE communications surveys & tutorials*, vol. 16, no. 4, pp. 2231–2258, 2014.

[165] P. P. Ray, "A perspective on 6G: Requirement, technology, enablers, challenges and future road map," *Journal of Systems Architecture*, vol. 118, p. 102180, 2021.

[166] H. Kaushal and G. Kaddoum, "Optical communication in space: Challenges and mitigation techniques," *IEEE communications surveys & tutorials*, vol. 19, no. 1, pp. 57–96, 2016.

[167] K. Anbarasi, C. Hemanth, and R. Sangeetha, "A review on channel models in free space optical communication systems," *Optics & Laser Technology*, vol. 97, pp. 161–171, 2017.

[168] M. Alzenad, M. Z. Shakir, H. Yanikomeroglu, and M.-S. Alouini, "Fso-based vertical backhaul/fronthaul framework for 5g+ wireless networks," *IEEE Communications Magazine*, vol. 56, no. 1, pp. 218–224, 2018.

[169] P. Kulshreshtha and A. K. Garg, "Managing 5G networks-a review of FSO challenges and solutions," in *2020 11th International Conference on Computing, Communication and Networking Technologies (ICCCNT)*, pp. 1–4, IEEE, 2020.

[170] S. A. H. Mohsan, M. A. Khan, and H. Amjad, "Hybrid fso/rf networks: A review of practical constraints, applications and challenges," *Optical Switching and Networking*, p. 100697, 2022.

[171] R. Nebuloni and E. Verdugo, "FSO path loss model based on the visibility," *IEEE Photonics Journal*, vol. 14, no. 2, pp. 1–9, 2022.

[172] A. S. Hamza, J. S. Deogun, and D. R. Alexander, "Classification framework for free space optical communication links and systems," *IEEE Communications Surveys & Tutorials*, vol. 21, no. 2, pp. 1346–1382, 2018.

[173] A. S. Hamza, J. S. Deogun, and D. R. Alexander, "Evolution of data centers: A critical analysis of standards and challenges for fso links," in *2015 IEEE Conference on Standards for Communications and Networking (CSCN)*, pp. 100–105, IEEE, 2015.

[174] A. Boucouvalas, P. Chatzimisios, Z. Ghassemlooy, M. Uysal, and K. Yiannopoulos, "Standards for indoor optical wireless communications," *IEEE Communications Magazine*, vol. 53, no. 3, pp. 24–31, 2015.

[175] C. Jenila and R. Jeyachitra, "Green indoor optical wireless communication systems: Pathway towards pervasive deployment," *Digital Communications and Networks*, vol. 7, no. 3, pp. 410–444, 2021.

[176] P. P. Ray, "A review on 6g for space-air-ground integrated network: Key enablers, open challenges, and future direction," *Journal of King Saud University-Computer and Information Sciences*, vol. 34, no. 9, pp. 6949–6976, 2022.

[177] X. Song, S. Haghighatshoar, and G. Caire, "A scalable and statistically robust beam alignment technique for millimeter-wave systems," *IEEE Transactions on Wireless Communications*, vol. 17, no. 7, pp. 4792–4805, 2018.

[178] G. Yang, J. Du, and M. Xiao, "Analysis on 60 GHz wireless communications with beamwidth-dependent misalignment," *arXiv preprint arXiv:1611.07867*, 2016.

[179] C. Pradhan, A. Li, L. Zhuo, Y. Li, and B. Vucetic, "Beam misalignment aware hybrid transceiver design in mmwave MIMO systems," *IEEE Transactions on Vehicular Technology*, vol. 68, no. 10, pp. 10306–10310, 2019.

[180] J. G. Andrews, A. K. Gupta, and H. S. Dhillon, "A primer on cellular network analysis using stochastic geometry," *arXiv preprint arXiv:1604.03183*, 2016.

[181] A. Alkhateeb, Y.-H. Nam, M. S. Rahman, J. Zhang, and R. W. Heath, "Initial beam association in millimeter wave cellular systems: Analysis and design insights," *IEEE Transactions on Wireless Communications*, vol. 16, no. 5, pp. 2807–2821, 2017.

[182] A. Al-Hourani and M. Haenggi, "Performance of next-generation cellular networks guarded with frequency reuse distance," *IEEE Transactions on Communications*, vol. 67, no. 10, pp. 7277–7287, 2019.

[183] J. G. Andrews, F. Baccelli, and R. K. Ganti, "A tractable approach to coverage and rate in cellular networks," *IEEE Transactions on communications*, vol. 59, no. 11, pp. 3122–3134, 2011.

[184] J. G. Andrews, T. Bai, M. N. Kulkarni, A. Alkhateeb, A. K. Gupta, and R. W. Heath, "Modeling and analyzing millimeter wave cellular systems," *IEEE Transactions on Communications*, vol. 65, no. 1, pp. 403–430, 2016.

[185] M. Wang, C. Zhang, X. Chen, and S. Tang, "Performance analysis of millimeter wave wireless power transfer with imperfect beam alignment," *IEEE Transactions on Vehicular Technology*, vol. 70, no. 3, pp. 2605–2618, 2021.

[186] M. Di Renzo, "Stochastic geometry modeling and analysis of multi-tier millimeter wave cellular networks," *IEEE Transactions on Wireless Communications*, vol. 14, no. 9, pp. 5038–5057, 2015.

[187] A. K. Gupta, J. G. Andrews, and R. W. Heath, "On the feasibility of sharing spectrum licenses in mmwave cellular systems," *IEEE Transactions on Communications*, vol. 64, no. 9, pp. 3981–3995, 2016.

[188] J. Park, J. G. Andrews, and R. W. Heath, "Inter-operator base station coordination in spectrum-shared millimeter wave cellular networks," *IEEE Transactions on Cognitive Communications and Networking*, vol. 4, no. 3, pp. 513–528, 2018.

[189] A. K. Gupta, A. Alkhateeb, J. G. Andrews, and R. W. Heath, "Gains of restricted secondary licensing in millimeter wave cellular systems," *IEEE Journal on Selected Areas in Communications*, vol. 34, no. 11, pp. 2935–2950, 2016.

[190] N. Deng and M. Haenggi, "A novel approximate antenna pattern for directional antenna arrays," *IEEE Wireless Communications Letters*, vol. 7, no. 5, pp. 832–835, 2018.

[191] N. Olson, J. G. Andrews, and R. W. Heath, "Coverage in terahertz cellular networks with imperfect beam alignment," in *2021 IEEE Global Communications Conference (GLOBECOM)*, pp. 1–6, IEEE, 2021.

[192] B. Bernardo, H. Fernández, V. M. R. Peñarrocha, J. Reig, and L. Rubio, "Experimental rician k-factor characterization in a laboratory environment at the 25 to 40 GHz frequency band," in *2020 IEEE International Symposium on Antennas and Propagation and North American Radio Science Meeting*, pp. 1121–1122, IEEE, 2020.

[193] P. Tang, J. Zhang, M. Shafi, P. A. Dmochowski, and P. J. Smith, "Millimeter wave channel measurements and modelling in an indoor hotspot scenario at 28 GHz," in *2018 IEEE 88th Vehicular Technology Conference (VTC-Fall)*, pp. 1–5, IEEE, 2018.

[194] L. Rubio, V. M. R. Peñarrocha, J. Reig, H. Fernández, J. R. Pérez, R. P. Torres, and L. Valle, "Analysis of the Rician K-factor in a typical millimeter-wave office scenario," *IEEE Antennas and Wireless Propagation Letters*, vol. 23, no. 5, pp. 1553–1557, 2024.

[195] Y. Guan, J. Zhang, L. Tian, P. Tang, and T. Jiang, "A comparative study for indoor factory environments at 4.9 and 28 GHz," in *2020 14th*

European Conference on Antennas and Propagation (EuCAP), pp. 1–5, IEEE, 2020.

[196] W. Lu and M. Di Renzo, "Stochastic geometry modeling of cellular networks: Analysis, simulation and experimental validation," in *Proceedings of the 18th ACM International Conference on Modeling, Analysis and Simulation of Wireless and Mobile Systems*, pp. 179–188, 2015.

[197] M. Di Renzo, W. Lu, and P. Guan, "The intensity matching approach: A tractable stochastic geometry approximation to system-level analysis of cellular networks," *IEEE Transactions on Wireless Communications*, vol. 15, no. 9, pp. 5963–5983, 2016.

[198] H. Wei and N. Deng, "A simple yet effective approximation for directional antenna arrays," in *2018 24th Asia-Pacific Conference on Communications (APCC)*, pp. 476–481, IEEE, 2018.

[199] T. Kebede, Y. Wondie, J. Steinbrunn, H. B. Kassa, and K. T. Kornegay, "Precoding and beamforming techniques in mmwave-massive mimo: Performance assessment," *IEEE Access*, vol. 10, pp. 16365–16387, 2022.

[200] Z. R. Hajiyat, A. Ismail, A. Sali, and M. N. Hamidon, "Antenna in 6g wireless communication system: Specifications, challenges, and research directions," *Optik*, vol. 231, p. 166415, 2021.

[201] C. Han, Y. Wang, Y. Li, Y. Chen, N. A. Abbasi, T. Kürner, and A. F. Molisch, "Terahertz wireless channels: A holistic survey on measurement, modeling, and analysis," *IEEE Communications Surveys & Tutorials*, vol. 24, no. 3, pp. 1670–1707, 2022.

[202] N. Chi, Y. Zhou, Y. Wei, and F. Hu, "Visible light communication in 6g: Advances, challenges, and prospects," *IEEE Vehicular Technology Magazine*, vol. 15, no. 4, pp. 93–102, 2020.